Recruited atypical Ly6G^{+} macrophages license alveolar regeneration after lung injury

C. Ruscitti[1,2], J. Abinet[1,2], P. Maréchal[1,2], M. Meunier[1,2], C. de meeûs[2,3], D. Vanneste[1,2], P. Janssen[1,2], M. Dourcy[2,4], M. Thiry[5], F. Bureau[2,6], C. Schneider[7], B. Machiels[2,4], A. Hidalgo[8,9], F. Ginhoux[10,11,12,13], B.G. Dewals[2,4], J. Guiot[14,15], F. Schleich[14,15], M-M. Garigliany[2,3], A. Bellahcène[16], C. Radermecker[1,2,*], T. Marichal[1,2,17,*]

Affiliations:

[1] Laboratory of Immunophysiology, GIGA Institute, University of Liège; Liège, Belgium
[2] Faculty of Veterinary Medicine, University of Liège; Liège, Belgium
[3] Department of Pathology, FARAH Institute, University of Liège; Liège, Belgium
[4] Laboratory of Immunology-Vaccinology, FARAH Institute, University of Liège; Liège, Belgium
[5] Laboratory of Cellular and Tissular Biology, GIGA Institute, University of Liège; Liège, Belgium
[6] Laboratory of Cellular and Molecular Immunology, GIGA Institute, University of Liège; Liège, Belgium
[7] Institute of Physiology, University of Zurich; Zurich, Switzerland
[8] Area of Cell & Developmental Biology, Centro Nacional de Investigaciones Cardiovasculares Carlos III; Madrid, Spain
[9] Vascular Biology and Therapeutics Program and Department of Immunobiology, Yale University School of Medicine; New Haven, CT, USA.
[10] Shanghai Institute of Immunology, Shanghai JiaoTong University School of Medicine; Shanghai, China.
[11] Inserm U1015, Gustave Roussy, Bâtiment de Médecine Moléculaire ; Villejuif, France.
[12] Singapore Immunology Network (SIgN), Agency for Science, Technology and Research (A*STAR); Singapore, Singapore.
[13] Translational Immunology Institute, SingHealth Duke-NUS Academic Medical Centre; Singapore, Singapore.
[14] Laboratory of Pneumology, GIGA Institute, University of Liège; Liège, Belgium
[15] Department of Respiratory Medicine, CHU University Hospital; Liège, Belgium
[16] Metastasis Research Laboratory, GIGA Institute, University of Liège; Liège, Belgium
[17] Walloon Excellence in Life Sciences and Biotechnology (WELBIO) Department, WEL Research Institute; Wavre, Belgium
[*] These authors contributed equally to this work and are co-last authors

*Corresponding authors: c.radermecker@uliege.be; t.marichal@uliege.be

Abstract

The lung is constantly exposed to airborne pathogens and particles that can cause alveolar damage. Hence, appropriate repair responses are essential for gas exchanges and life. Here, we deciphered the spatiotemporal trajectory and function of an atypical population of macrophages after lung injury. Post-influenza A virus (IAV) infection, short-lived monocyte-derived Ly6G-expressing macrophages ($Ly6G^+$ Macs) were recruited to the alveoli of lung perilesional areas. $Ly6G^+$ Macs engulfed immune cells, exhibited a high metabolic potential and clustered with alveolar type 2 (AT2) epithelial cells in zones of active epithelial regeneration. $Ly6G^+$ Macs were partially dependent on GM-CSF and IL-4 receptor signaling and were essential for AT2-dependent alveolar regeneration. Similar macrophages were recruited in other models of injury and in the airspaces of lungs from patients suspected of pneumonia. This study identifies perilesional alveolar $Ly6G^+$ Macs as a spatially-restricted, short-lived macrophage subset promoting epithelial regeneration post-injury, thus representing an attractive therapeutic target for treating lung damage.

One-Sentence Summary

Short-lived perilesional $Ly6G^+$ macrophages license alveolar epithelial regeneration after viral-triggered lung injury.

Introduction

Severe respiratory viral infections represent a global health issue and a major threat for the healthcare systems as they often require hospitalization, such as seen during annual influenza A virus (IAV) outbreaks or the Covid-19 pandemic. Acute lung infectious episodes are typically associated with excessive lung inflammation, damage, and abnormal tissue repair that can lead to acute respiratory distress syndrome (ARDS), pneumonia and death (*1–5*). Deciphering the mechanisms eliciting appropriate lung regeneration and host recovery after viral-triggered lung injury is urgently needed to improve clinical management and broaden therapeutic opportunities.

Blood monocytes are heavily recruited to the lungs during the acute inflammatory phase post-infection, thereby contributing to host innate defense mechanisms. When not appropriately regulated, they are also thought to contribute to uncontrolled inflammation via the aberrant release of cytokines, which, in its extreme form, is known as the "cytokine storm", well described in severe Covid-19 patients (*3*, *6–9*). Recruited monocytes can also differentiate into monocyte-derived macrophages (Mo-Macs) that are either short-lived or can establish long-term residency in particular niches and can have functional consequences for lung immunity (*10–15*). The idea that recruited Mo-Macs are considered pathogenic after influenza infection (*15*, *16*) or Covid-19 (*6*, *17*), while lung-resident alveolar macrophages (AM) and interstitial macrophages (IM) exert beneficial roles (*13*, *18–24*) is likely oversimplistic. Indeed, recruited Mo-Macs are increasingly recognized as heterogenous and can adopt distinct functional identities that depend on their differentiation trajectory, the diseased tissue microenvironment, the extent and phase of inflammation, and their activation state (*9*, *13*, *14*, *18*, *25*). In this regard, the fate and functions of short-lived Mo-Macs after lung injury remain incompletely described.

Here, we used an *in vivo* model of IAV-triggered injury to investigate the spatiotemporal trajectory and function of an atypical population of Mo-Macs expressing Ly6G, a marker considered to be restricted to granulocytes. We found that Ly6G$^+$ Macs emerged transiently from Ccr2-dependent monocytes during the early recovery phase post-IAV, populated the alveolar lumen of lung perilesional areas and could promote progenitor AT2 differentiation and alveolar re-epithelization. Our study thus unravels the fate and function of a previously undescribed Ly6G$^+$ Mac population that engages in crosstalk with epithelial cells to promote epithelial repair after viral-triggered lung injury.

Results

Lung Ly6G$^+$ Macs emerge in the early recovery phase post-IAV infection

To investigate the dynamic of myeloid cell responses after lung injury, we performed time-course flow cytometry studies in a clinically relevant mouse model of lung infectious injury following IAV infection (*2*). Eight to twelve weeks-old C57BL/6 wild-type (WT) mice were infected intranasally (i.n.) with 5 plaque-forming units (PFU) of IAV H1N1 strain PR8/34, which triggered self-limiting disease with a peak in viral RNA at day 5 post-IAV and viral clearance at day 10 post-IAV (fig. S1, A and B). In this model, Ly6G$^+$CD11b$^+$CD64$^-$ neutrophils (Neu) increased at day 5 post-IAV and returned to baseline by day 15 (Fig. 1, A and B). A partial loss of Ly6G$^-$CD64$^+$SiglecF$^+$CD11c$^+$ AM was observed between day 5 and day 10 post-IAV, which was restored at day 15 post-IAV, as described (*15*) (Fig. 1, A and B). The numbers of CD64$^-$Ly6C$^-$ monocytes (Ly6C$^-$ Mo) remained stable over the course of infection, unlike those of classical CD64$^-$Ly6C$^+$ Mo (Ly6C$^+$ Mo) and inflammatory CD64$^+$Ly6C$^+$ monocytes (iMo) that peaked around day 5 post-IAV (Fig. 1, A and B). Macrophages (Macs) resembling IM (IM-like), defined as F4/80$^+$CD11b$^+$Ly6G$^-$SiglecF$^-$Ly6C$^-$CD64$^+$ cells and likely encompassing resident IM and recruited Mo-Macs, increased over time (Fig. 1, A and B). We also observed emergence, from day 5 onwards, of a distinct population of IAV-triggered Ly6G$^+$CD11b$^+$CD64$^+$ Macs that fell in the classical Ly6G$^+$CD11b$^+$ neutrophil gate but were clearly distinct from neutrophils based on their elevated CD64 expression (Fig. 1, C and D), which we call Ly6G$^+$ Macs hereafter. Ly6G$^+$ Macs were absent in the blood (Fig. 1E), peaked at day 10 post-IAV in the lung and could still be detected at days 15 and 20 post-IAV (Fig. 1D). Morphologically, Ly6G$^+$ Macs analyzed at day 10 post-IAV exhibited a kidney-shaped nucleus, like iMo, and possessed numerous cytoplasmic vacuolated structures and a cell membrane rich in protrusions (Fig. 1F and fig. S1C). Phenotypically, Ly6G$^+$ Macs were F4/80^{hi}SiglecF^{lo}CD11c^{lo} (fig. S1, D and E) and expressed high levels of the chemokine receptor CXCR4, of type II major histocompatibility complex (MHC-II), of CD101 and of CD319, a regulator of Mac functions (*26*, *27*) (Fig. 1, G and H). However, Ly6G$^+$ Macs exhibited low expression of the neutrophil activation marker CD177 (Fig. 1, G and H).

Next, we performed single cell (sc) RNA-sequencing (scRNA-seq) analyses of lung myeloid cells at day 10 post-IAV. Lung CD45$^+$F4/80$^+$ and/or CD11b$^+$ cells were sorted from five mock-infected and 5 IAV-infected mice and were subjected to sc droplet encapsulation (*28*), scRNA-seq and quality control filtering. The curated data were integrated with a published dataset of steady-state lung monocytes and IM (*29*) and projected to global and condition-specific uniform manifold approximation and projection (UMAP) plots (Fig. 2A). Myeloid cells from mock-infected mice mainly comprised clusters annotated as AM (*Chil3, Ear1, Fapb1*; C6), Ly6C$^-$ Mo (*Ace, Nr4a1, Fcgr4*; C3), Ly6C$^+$ Mo (*Ccr2, Ly6c2*; C4) and dendritic cells (DC; *H2-Ab1, Cd209a, Flt3;* C9) (Fig. 2A-C and fig. S2A). Few cycling Macs (*Birc5, Top2a, Mki67*; C11) were also detected in mock-infected mice, along with few CD206$^-$ IM (*C1qa, C1qc, H2-Ab1, Cd74, Tmem119;* C1) and CD206$^+$ IM (*C1qa, C1qc, Mrc1, Maf;* C8) (*29*) (Fig. 2A-C and fig. S2A). Ten days post-IAV, AM (C6) disappeared, a small cluster of IAV-associated AM was present instead (*Chil3, Ear1, Ear 2*; C12), Neu were recruited (*S100a8, S100a9, Mmp9*; C7), and IM (C1, C8) and iMo (*Ccr2, Ly6c2, Irf7*; C5) expanded (Fig. 2A-C and fig. S2A). Of note, clusters C2 and C10 were specifically triggered by IAV. C10 had an elevated content in mitochondrial genes and low numbers of detected genes (fig. S2B) and was therefore annotated as dying Macs. C2 expressed significantly higher levels of cathepsins (*Ctsb, Ctsz*), galectins (*Lgals1, Lgals3*), Arginase-1 (*Arg1*) and osteopontin (*Spp1*) as compared to the other clusters (Fig. 2D). Intracellular flow cytometry staining for Arginase-1 and osteopontin showed that the combined expression of these two proteins was restricted to Ly6G$^+$ Macs at day 10 post-IAV (Fig. 2, E and F), supporting that C2 corresponded

to Ly6G$^+$ Macs identified by flow cytometry. Of note, Ly6G$^+$ Macs expressed high levels of *Csf1r* and *Slamf7* (coding for CD319) but did not express any of the neutrophil-related transcripts *Csf3r*, *S100a8, S100a9, Mmp8, Mmp9, Mpo, Slpi* or *Cd177* (fig. S2, A and C). *Ly6g* transcripts were not detectable in Neu nor Ly6G$^+$ Macs (fig. S2, A and C). Ly6G$^+$ Macs (C2) displayed both "M1-like" or "M2-like" signature scores and genes and could not be categorized as such on the basis of their expression profile (fig. S2, D and E). Together, our data show that a phenotypically and transcriptionally distinct subset of Ly6G$^+$ Macs emerges during a specific time window corresponding to early weight recovery post-IAV.

Ly6G$^+$ Macs arise from recruited monocytes and are partially dependent on GM-CSF receptor signaling

We next investigated the origin of Ly6G$^+$ Macs and asked whether they could expand via local proliferation. We observed that the percentage of cells positive for the proliferation Ki67 was very low in Ly6G$^+$ Macs (fig. S3A). Next, we treated mice at day 10 post-IAV intraperitoneally (i.p.) with 5-ethynyl-2′-deoxyuridine (EdU) 4 hours before analysis. While the percentage of EdU$^+$ cells was higher in AM compared to all other lung myeloid cells, indicative of active proliferation, virtually no EdU$^+$ cells were detected in Ly6G$^+$ Macs, ruling out their active proliferation (fig. S3, B and C). Third, we assessed whether Ly6G$^+$ Macs arose from the BM or from local progenitor monocytes (*30*). We generated chimeric mice in which lethally irradiated, thorax-protected CD45.2 WT mice were reconstituted with BM cells from *Ms4a3*^{Cre}*R26*$^{LSL\text{tdTomato}}$ mice (subsequently referred to as *Ms4a3*^{tdTom}), in which the progeny of granulocyte monocyte progenitors (GMPs) is constitutively labelled (*31*). At week 4 after transfer, the percentages of tdTomato$^+$ blood Ly6C$^+$ Mo was around 50%, while the percentages of tdTomato$^+$ lung AM and IM were very low, confirming efficient reconstitution and thorax protection (fig. S3, D-G). At day 10 post-IAV, we found that the percentage of tdTomato$^+$ Ly6G$^+$ Macs was similar to that of Ly6C$^+$ Mo (fig. S3, H and I), consistent with a major contribution of BM-derived GMPs, but not local progenitors, to Ly6G$^+$ Macs.

The kinetics of Ly6G$^+$ Mac emergence post-IAV was comparable but delayed compared to that of Ly6C$^+$ Mo and iMo, consistent with the idea that recruited Ly6C$^+$ Mo could give rise to Ly6G$^+$ Macs. Supporting this, Slingshot trajectory analyses of the scRNA-seq data identified two main trajectories starting from Ly6C$^+$ Mo, transiting through iMo to give rise to either IM-like cells or Ly6G$^+$ Macs (*32*) (Fig. 3A). Genes that exhibited the same pattern of downregulation along pseudotime in each trajectory encompassed the classical monocyte-associated genes *Ccr2* and *Ly6c2* (Fig. 3B). We also found, in both trajectories, a time-restricted upregulation of interferon-stimulated genes (*Ifi209, Ifitm3, Ifi47, Isg15*) that likely corresponded to transitioning iMo (Fig. 3B). Finally, trajectory-specific genes were gradually and specifically upregulated along pseudotime in the IM-like (e.g., *C1qa, C1qc, C1qb, Mrc1, Cd74, H2-Ab1, H2-Eb1*) or the Ly6G$^+$ Mac (e.g., *Arg1, Spp1, Ccl2, Ccl7, Ctsb*) trajectories (Fig. 3B).

Next, we infected the monocyte fate-mapper mice *Ms4a3*^{tdTom} (*31*) and *Cx3cr1*^{GFP} (*33*) with IAV and found that, at day 10 post-IAV, Ly6G$^+$ Macs were Tomato$^+$ and GFP^{hi}, respectively, consistent with their GMP-derived monocytic origin (Fig. 3, C and D). To address the dependency of Ly6G$^+$ Mac on Ccr2-dependent BM-derived Ly6C$^+$ Mo (*34*), we generated BM competitive chimeras in which lethally irradiated CD45.1/CD45.2 WT mice were engrafted with a 1:1 mix of CD45.2 *Ccr2*$^{-/-}$ and CD45.2 *Ms4a3*^{tdTom} BM cells. At week 4 after reconstitution, most blood Ly6C$^+$ Mo were of donor Tomato$^+$ origin, as expected (fig. S3, J and K) (*34*). At day 10 post-IAV, the majority

of Ly6G$^+$ Macs was also of donor *Ms4a3^{tdTom}* origin, indicating their dependency on Ccr2 (Fig. 3, E and F).

We next sought to assess the fate and lifespan of Ly6G$^+$ Macs. The abundance of Ly6G$^+$ Macs during a limited time window post-IAV suggested that they might be short-lived. In line with this, trajectory analyses in Fig. 3A suggested that Ly6G$^+$ Macs (C2) gave rise to Macs with low RNA content (C10) (fig. S2B). We performed EdU pulse experiments at day 7 post-IAV and found that Ly6G$^+$ Macs staining positive for EdU at day 10 post-IAV were completely cleared from the lung at day 17 (Fig. 3G). Annexin V/Propidium iodide (PI) staining at day 10 post-IAV further supported that Ly6C$^+$ Mo transitioning to iMo and differentiating into Ly6G$^+$ Macs became progressively more sensitive to death, with a substantial portion of Ly6G$^+$ Macs being either early or late apoptotic (Annexin V$^+$/PI$^{+/-}$), or necrotic (Annexin V$^-$/PI$^+$) (Fig. 3H and fig. S3L). Hence, our data show that Ly6G$^+$ Macs represent a short-lived Mac subset arising from Ccr2-dependent Ly6C$^+$ Mo.

The Ly6G signal on Ly6G$^+$ Macs, considered to be neutrophil-specific, was unexpected and required careful validation. First, we verified that the Ly6G fluorescence intensity was virtually absent in unstained or isotype antibody (Ab)-stained CD11b$^+$ cells from IAV-infected WT mice (fig. S4A). Second, we evaluated whether Ly6G$^+$ Mac precursors, namely iMo, could intrinsically upregulate Ly6G on their surface when isolated from the lungs of IAV-infected mice at day 10 post-IAV. We found that iMo from IAV-infected mice and stimulated *ex vivo* with GM-CSF, and to a less extent with M-CSF, upregulated Ly6G protein on their surface (Fig. 3, I and J). Importantly, we also found that lung iMo isolated from IAV-infected *Ly6g^{CreERT2}R26^{LSL}*tdTomato mice (*Ly6g^{tdTom}*) treated with tamoxifen and stimulated with GM-CSF ex vivo became tdTomato$^+$, indicative of active *Ly6g* gene transcription in monocytic cells (Fig. 3, K and L). These data demonstrate that Ly6G can be actively expressed by Mo-Macs.

Given the ability of GM-CSF to trigger Ly6G expression on lung iMo isolated from IAV-infected mice, we assessed the dependency of Ly6G$^+$ Macs on GM-CSF receptor signaling *in vivo*. We generated BM competitive chimeras in which thorax-protected, lethally irradiated CD45.1/CD45.2 WT mice were engrafted with a 1:1 mix of CD45.1 *Csf2ra$^{-/-}$* and CD45.2 *Csf2ra$^{+/+}$* BM donor cells. At week 4 after reconstitution, blood Neu and Mo of donor origin arose equally from CD45.1 *Csf2ra$^{-/-}$* and CD45.2 *Csf2ra$^{+/+}$* BM cells (fig. S4, B and C). At day 10 post-IAV, we found that CD45.2 *Csf2ra$^{+/+}$* BM cells had a competitive advantage over CD45.1 *Csf2ra$^{-/-}$* BM cells to become Ly6G$^+$ Macs, which was not observed among most other lung myeloid cells (Fig. 3M and fig. S4C-E), and the percentage of Arg-1$^+$ cells was lower in *Csf2ra$^{-/-}$* Ly6G$^+$ Macs as compared to *Csf2ra$^{-/-}$* Ly6G$^+$ Macs (Fig. 3, N and O), indicating their partial dependency on GM-CSF receptor signaling.

Ly6G$^+$ Macs exhibit distinct ultrastructural features associated with elevated metabolic and phagocytic abilities

Gene Set Enrichment Analyses (GSEA) of the transcriptomic profile of Ly6G$^+$ Macs (C2) compared to all other clusters identified a response to interferon-γ and cytokines, chemotactic and viral processes, an active metabolic state, a highly developed endomembrane system and elevated phagocytic abilities in Ly6G$^+$ Macs (Fig. 4A). We analyzed FACS-sorted Ly6G$^+$ Macs by transmission electron microscopy at day 10 post-IAV and found that they exhibited a kidney-shaped nucleus, microvilli-rich membrane, secretory granules and a cytoplasm rich in rugous endoplasmic reticulum (RER), Golgi apparatus, lysosomes and autophagy vacuoles, distinguishing them from Neu, Ly6C$^+$ Mo and IM-like cells (Fig. 4B). The morphology of Ly6G$^+$ Macs was

reminiscent to that of an atypical population of monocytes, called SatM monocytes, which arise from particular GMPs during the fibrotic phase in lungs post-bleomycin, contribute to fibrosis and were regulated by CCAAT/enhancer binding protein β (C/EBPβ) (*35*). We conducted a single-cell regulatory network inference and clustering (SCENIC) analysis (*36*) and found that C/EBPβ activity was lower in Ly6G$^+$ Macs compared to Ly6C$^-$ Mo, Ly6C$^+$ Mo, iMo and Neu (fig. S5A). Moreover, we generated a SatM signature score based on the genes unregulated in SatM monocytes (*35*), mapped such score to our scRNA-seq data and found that Ly6G$^+$ Macs displayed a lower SatM score compared to IM, Ly6C$^+$ Mo, Ly6C$^-$ Mo or iMo (fig. S5, B and C), supporting that Ly6G$^+$ Macs are not dependent on C/EBPβ and are transcriptionally distinct from SatM monocytes (*35*).

Next, we characterized the metabolic profile of Ly6G$^+$ Macs using a metabolic flux assay and found that the extracellular acidification rate (ECAR) was higher in Ly6G$^+$ Mac compared to IM-like cells, both at baseline and under stress, supporting that the glycolytic pathway was highly active in Ly6G$^+$ Macs (Fig. 4C). Moreover, while the basal mitochondrial oxygen consumption rate (OCR) was similar between Ly6G$^+$ Mac and IM-like cells, the OCR under stress conditions was higher in Ly6G$^+$ Macs compared to IM-like cells (Fig. 4D), supporting that they possessed a high metabolic potential (Fig. 4E).

We administered infected mice with fluorescently-labeled E. coli particles intratracheally (i.t.) at day 10 post-IAV and confirmed that Ly6G$^+$ Macs were highly phagocytic compared to Neu, Ly6C$^+$ Mo, IM-like cells and AM (Fig. 4, F and G). Hence, we asked whether Ly6G$^+$ Macs could perform efferocytosis *in vivo*. To this end, we infected BM competitive chimeras in which lethally irradiated CD45.2 WT mice were engrafted with a 1:1 mix of *Cx3cr1*$^{GFP/+}$ and *Ms4a3*^{tdTom} BM cells. Of note, at day 10 post-IAV, 60% of *Cx3cr1*$^{GFP/+}$ Ly6G$^+$ Macs were also tdTomato$^+$ (Fig. 4, H and I and fig. S6, A-C), demonstrating that they were highly potent in engulfing myeloid cells *in vivo.* To assess whether Ly6G molecules could be transferred from Neu to Ly6G$^+$ Macs during efferocytosis, we infected BM competitive chimeras in which lethally irradiated CD45.1/CD45.2 WT mice were engrafted with a 1:1 mix of *Cx3cr1*$^{GFP/+}$ cells and *Ly6g*$^{-/-}$ (i.e., homozygous *Ly6g*^{CreERT2} mice) (*37*) or *Ly6g*$^{+/+}$ BM cells. At day 10 post-IAV, we found that the levels of Ly6G on *Cx3cr1*$^{GFP+}$ Ly6G$^+$ Macs from *Cx3cr1*$^{GFP+}$: *Ly6g*$^{-/-}$ BM chimeric mice, in which half of the Neu were *Ly6g*$^{-/-}$, were similar to those from *Cx3cr1*$^{GFP+}$: *Ly6g*$^{+/+}$ BM chimeric mice, supporting no evidence for a Ly6G transfer from Neu to Ly6G$^+$ Macs (fig. S6, D and E). Together, these data show that IAV-triggered Ly6G$^+$ Macs are characterized by metabolic, morphological and efferocytic properties distinct from other lung myeloid cells.

Ly6G$^+$ Macs populate the alveolar lumen of perilesional regenerating areas

Next, we investigated the localization and the spatial organization of Ly6G$^+$ Macs. First, we performed confocal microscopy staining of lung sections of infected *Cx3cr1*^{GFP} mice at day 10 post-IAV. By defining Ly6G$^+$ Macs as cells double positive for Ly6G and GFP, we found that they were located in the alveolar lumen (Fig. 5A), which was also confirmed by *in situ* electron microscopy (Fig. 5B).

To further investigate the spatial distribution of Ly6G$^+$ Macs and the molecular signatures of Ly6G$^+$ Macs-rich areas, we performed spatial transcriptomic analyses using GeoMx Digital Spatial Profiler (DSP), which allows whole-genome transcript analyses within regions of interest (ROIs). Lung sections from 2 mock- and 4 IAV-infected mice were collected at day 10 post-IAV, stained with anti-CD68 and anti-Ly6G antibodies, and ROIs were selected in control lungs (4 ROIs), extralesional zones (4 ROIs), intralesional zones (5 ROIs) and zones rich in Ly6G$^+$CD68$^+$ cells that were mostly located in the periphery of consolidated areas (perilesional, 11 ROIs) (Fig.

5C and fig. S7A). Unsupervised principal component (PC) analysis showed that perilesional ROIs were separated from the other regions (Fig. 5D). Volcano plot representation of the differentially expressed (DE) genes between conditions and the heatmap of the 522 significantly upregulated genes in perilesional areas compared to the other areas supported that perilesional areas were transcriptionally very active (fig. S7, B and C). General cellular deconvolution indicated that perilesional zones were also enriched in tissue Macs as compared to the other regions (fig. S7D). We next mapped cell signature scores of lung myeloid cell populations analyzed by scRNA-seq to the ROIs and confirmed that perilesional zones were enriched in Ly6G$^+$ Mac compared to the other zones (Fig. 5E and fig. S7E). GSEA analyses indicated that perilesional areas were enriched in biological responses related to cytoskeleton activity, epithelial cell migration and elevated metabolic activity compared to intralesional areas, consistent with intense remodeling activities (Fig. 5F).

Next, we took advantage of a publicly available scRNA-seq dataset of alveolar epithelial cell states present during alveolar regeneration after bleomycin-induced lung injury (*38*) and containing type 1 and type 2 alveolar epithelial cells (AT1 and AT2, respectively), as well as transitional states appearing during AT2 to AT1 differentiation, called primed AT2 and damage-associated transient progenitors (DATPs) (*38*). By mapping the signature scores of such transitional epithelial cell states to the ROIs, we found that Ly6G$^+$ Mac-rich perilesional zones were enriched in primed AT2 and DATPs compared to control and intralesional zones (fig. S7, F and G). Accordingly, the Ly6G$^+$ Mac score correlated positively with those of primed AT2 and DATPs (Fig. 5G). We also confirmed by confocal microscopy that Ly6G$^+$ Macs were particularly abundant in the periphery of consolidated areas and clustered with AT2 cells, while intralesional consolidated areas, which exhibited low levels of staining for AT1 and AT2, contained few Ly6G$^+$ Macs (Fig. 5H and fig. S8). Altogether, these data are consistent with perilesional areas serving as the site of active epithelial regeneration post IAV, and that Ly6G$^+$ Macs, which cluster in such areas, contribute to this process.

Ly6G$^+$ Macs promote alveolar epithelial regeneration through IL-4R signaling

To formally assess the function of Ly6G$^+$ Macs *in vivo*, we aimed to generate a transgenic mouse strain in which Ly6G$^+$ Mac differentiation was impaired. Thus, we applied the SCENIC algorithm to our scRNA-seq data to map gene regulatory networks and predict transcription factor activities in Ly6G$^+$ Macs (*36*). Of note, c-Maf and MafB exhibited a high regulon activity in Ly6G$^+$ Macs and IM-like cells, as described (*39*), but not in other lung myeloid cells (Fig. 6A and fig. S9). Elevated c-Maf and MafB protein levels were also detected in Ly6G$^+$ Macs at day 10 post-IAV by flow cytometry (Fig. 6, B and C), and *Maf* and *Mafb* transcript levels were elevated in lung Ly6G$^+$ Mac-rich perilesional areas of IAV-infected mice (Fig. 6D). We generated mice with myeloid-restricted *Maf* and *Mafb* deficiency by crossing *Maf* and *Mafb* floxed mice (*Maf*/*Mafb*$^{fl/fl}$) with mice constitutively expressing Cre recombinase under the control of the lysozyme M promoter (*Lyz2*^{Cre}), called *Maf/Mafb*^{MyeloKO} mice hereafter. At day 10 post-IAV, *Maf/Mafb*^{MyeloKO} mice showed a virtual absence of Ly6G$^+$ Macs, while numbers of Neu, AM, IM-like cells, Ly6C$^+$ Mo and iMo were similar and numbers of Ly6C$^-$ Mo were higher compared to control mice (Fig. 6E). Hence, we employed this model to address the consequences of Ly6G$^+$ Mac deficiency on viral control, morbidity and alveolar epithelial repair following IAV infection.

We assessed the levels of lung mRNA coding for the non-structural influenza protein NS1 post-IAV and found that they were not significantly different between *Maf/Mafb*^{MyeloKO} and controls and returned to baseline at day 10 post-IAV (Fig. 6F), supporting that Ly6G$^+$ Macs did not substantially influence host viral control. However, *Maf/Mafb*^{MyeloKO} mice lost more weight post-IAV compared to controls (Fig. 6G), suggestive of a more severe IAV-induced pathology.

Histopathological analyses of lung sections at day 20 post-IAV indicated broader lesional areas in *Maf/Mafb*^{MyeloKO} mice compared to controls, as well as more pronounced dysplastic repair and bronchiolization of the alveoli, based on quantification of mucus area in lung lesional areas (Fig. 6H-J). These results suggested that, in the absence of Ly6G$^+$ Macs, the classical pathway of alveolar epithelial regeneration involving progenitor AT2 expansion and differentiation towards AT1 (*40*, *41*) was defective and compensated by dysplastic repair. Next, we evaluated the numbers of AT1, AT2 and regenerating AT2 (regAT2) at day 20 post-IAV in *Maf/Mafb*^{MyeloKO} and control mice by flow cytometry and observed a significant decrease in the numbers of AT2 and regAT2 in *Maf/Mafb*^{MyeloKO} mice compared to controls (Fig. 6, K and L), confirming that AT2 were less able to expand and differentiate into AT1 in the absence of Ly6G$^+$ Macs. Of note, i.t. transfer of Ly6G$^+$ Macs isolated from lungs of WT mice at day 10 post-IAV into IAV-infected *Maf/Mafb*^{MyeloKO} mice partially improved weight recovery and restored numbers of AT2 to the levels observed in IAV-infected control mice (Fig. 6, M and N). These results suggest that Ly6G$^+$ Macs are key players of euplastic epithelial regeneration after IAV-induced lung injury.

To determine whether Ly6G$^+$ Mac-rich perilesional areas were imprinted by a type 2 reparative environment (*19*, *42*, *43*), we mapped a type 2 signature score based on genes involved in IL-4 receptor downstream signaling pathways to the DSP spatial transcriptomic data and found that perilesional areas exhibited the highest type 2 score as compared to the other ROIs (Fig. 7A). Hence, we asked whether IL-4 receptor signaling, whose activation is known to induce a repair phenotype in Macs (*19*, *42*, *43*), was involved in Ly6G$^+$ Mac identity and function. First, we found that Ly6G$^+$ Macs expressed high levels of the IL-4 receptor α chain (IL-4Rα) (Fig. 7, B and C). Next, we generated BM competitive chimeras in which lethally irradiated CD45.1/CD45.2 WT mice were engrafted with a 1:1 mix of CD45.2 *Il4ra*$^{-/-}$ and CD45.2 *Ms4a3*^{tdTom} BM cells. At week 4 after reconstitution, efficient BM reconstitution was confirmed in the blood (fig. S10, A and B). At day 10 post-IAV, we found that Ly6G$^+$ Macs of donor *Ms4a3*^{tdTom} origin exhibited a competitive advantage over those of donor *Il4ra*$^{-/-}$ origin, which was not observed among other lung myeloid cells (Fig. 7D and fig. S10, C and D), and the remaining *Il4ra*$^{-/-}$ Ly6G$^+$ Macs were impaired in their ability to express Arg-1 (Fig. 7, E and F). Finally, WT chimeric mice fully reconstituted with *Il4ra*$^{-/-}$ or WT BM cells were generated (*Il4ra*$^{-/-}$ BM -> WT or WT BM -> WT, respectively) and infected with IAV. We found, like in *Maf/Mafb*^{MyeloKO} mice, that *Il4ra*$^{-/-}$ BM -> WT mice had an impaired recovery post-IAV compared to WT BM -> WT mice (Fig. 7G). These data suggest that Ly6G$^+$ Macs exert their function via IL-4R-dependent pathways, at least in part.

Finally, we asked whether Ly6G$^+$ Macs could directly influence AT2 fate and whether cell-cell contacts were needed. To this end, we performed a scratch assay *in vitro* using the MLE-12 mouse AT2 cell line and evaluated the confluence of AT2 cells 12 hours post-scratch in the presence or absence of Ly6G$^+$ Macs isolated from infected lung at day 10 post-IAV. Co-culture with Ly6G$^+$ Macs, but not with Neu, IM-like cells or iMo was associated with an increase in cell confluence (Fig. 7H), indicating that Ly6G$^+$ Macs can directly and specifically promote wound healing in vitro. A similar scratch assay was also performed using conditioned medium (CM) from FACS-sorted Ly6G$^+$ Macs that were cultured overnight with or without the type 2 cytokines IL-4 and IL-13. In this setting, CM from IL-4/13-pulsed Ly6G$^+$ Macs could promote wound healing compared to control medium (containing only IL-4 and IL-13) or CM from unpulsed Ly6G$^+$ Macs (Fig. 7, I and J). We performed proteome profiling on such CM and found that Ly6G$^+$ Macs were highly potent in secreting soluble factors, among which were chemokines (CCL5, CXCL16, CCL12, CXCL10), cytokines (TNF-α, IL-10, IL-1α) and osteopontin, some of which were increased upon IL-4R activation (Fig. 7K). Some of the molecules detected in the CM of Ly6G$^+$ Macs had their transcript levels significantly upregulated in Ly6G$^+$ Macs (C2) as compared to other clusters (fig.

S11). Altogether, our data demonstrate that Ly6G$^+$ Macs can release soluble factors upon IL-4 receptor triggering that act directly on AT2 to promote epithelial regeneration (fig. S12).

Ly6G$^+$ Macs belong to a conserved host response to injury across organs, triggers and species

We evaluated whether Ly6G$^+$ Macs were specifically recruited in the IAV model or were also triggered in other models of injury. First, we used a model of non-infectious lung injury based on bleomycin (bleo) instillation and performed time-course flow cytometry analyses. Ly6G$^+$ Macs expressing high levels of Arg-1 and CXCR4 were mostly present between day 7 and day 14 post-bleo, which correlated with signs of epithelial damage, as reflected by the decrease in numbers of AT1 and AT2 (Fig. 8A-E). We also found similar Ly6G$^+$ Macs peaking at days 1 and 2 post-treatment in an acute model of acetaminophen-induced liver injury, which correlated with the release of alanine aminotransaminase (ALT) in plasma (Fig. 8F-I). Our data thus suggested that Ly6G$^+$ Macs are a component of a conserved response to tissue damage, regardless of the organ or trigger.

Finally, we asked whether Macs sharing a similar transcriptomic signature were also present in the broncho-alveolar lavage fluid (BALF) of diseased humans. We performed scRNA-seq analyses of BALF cells from 7 patients with a suspicion of pneumonia and manually annotated the cell clusters based on the most upregulated genes (Fig. 8, J and K and fig. S13). Next, we mapped a Ly6G$^+$ Mac score based on orthologous genes in humans to the BALF cells and found that cells exhibiting the highest Ly6G$^+$ Mac score belonged to the same cluster C9 identified as Mo-Macs based on their high expression of monocyte genes and their low expression of AM-associated genes (Fig. 8, L and M). SCENIC analyses (*36*) predicted higher MAF and MAFB activities in the Mo-Mac cluster compared to other clusters (Fig. 8N), further supporting that the airspace of human pneumonia lungs contains Mo-Macs that are transcriptionally similar to mouse Ly6G$^+$ Macs.

Discussion

Restoration of gas exchanges after lung injury is critical for life and relies on appropriate regulation of inflammation and regeneration of the damaged alveoli. While recent progress has been made in understanding the epithelial-intrinsic mechanisms underlying alveolar regeneration post-injury (*3*, *38*, *41*, *44–47*), an important gap resides in our understanding of the innate immune-epithelial crosstalk taking place to promote epithelial repair and host recovery. While recruited Mo-Macs are often seen as culprits and drivers of disease progression in different contexts, such as in Covid-19, interstitial fibrosis or lung cancer (*13*, *17*, *18*, *48*), advances in single cell and spatial technologies have enabled new opportunities to investigate the spatiotemporal regulation of Mo-Mac responses in-depth. Here, using such approaches combined with lineage tracing, BM chimeras, gene targeting, multi-parameter flow cytometry and imaging, our work identifies a previously undescribed atypical population of short-lived recruited Ly6G$^+$ Macs that critically contributes to alveolar epithelial regeneration post-injury in mice.

To our knowledge, there is no report of such Ly6G$^+$ Macs in the literature. Of note, Ly6G is largely considered as a neutrophil-specific marker (*49*), and, in many studies employing cytometry, anti-Ly6G antibodies are included to gate out "neutrophils" before gating on Macs. Hence, Ly6G$^+$ Macs might have been previously overlooked and considered as part of the neutrophil compartment. Here, we provide evidence that the Ly6G signal is specific and that lung iMo, the precursors of Ly6G$^+$ Macs, can actively express Ly6G gene and protein upon GM-CSF stimulation *ex vivo*. Of note, GM-CSF is mainly produced by AT2 cells (*41*, *50*), which are located in the vicinity of Ly6G$^+$ Macs, and Ly6G$^+$ Macs were dependent on GM-CSF receptor signaling for their generation and Arg-1 expression post-IAV infection *in vivo*. Further supporting an intrinsic upregulation of Ly6G, we found no evidence of Ly6G protein transfer from neutrophils to Ly6G$^+$ Macs. In addition to Ly6G expression, Ly6G$^+$ Macs were phenotypically and transcriptionally distinct from neutrophils and exhibited key developmental, phenotypic and transcriptomic macrophage features including their dependency on Ccr2, elevated Cx3cr1 expression, and their dependency on the transcription factors c-Maf and MafB. However, *Ly6g* does not appear as a target gene of c-Maf and MafB in the ChiP atlas, suggesting alternative gene regulatory mechanisms.

We found that Ly6G$^+$ Macs were transiently recruited to the alveolar spaces of particular lung areas and remained phenotypically and transcriptionally distinct from tissue-resident AM. Our data thus suggest that the local microenvironment of Ly6G$^+$ Macs, which can shape Mac identity (*13*, *51–53*), is dynamically regulated and distinct from that of AM. First, we found that Ly6G$^+$ Macs originate from BM-derived monocytes recruited to the lung in a Ccr2-dependent manner. Second, we showed that such inflammatory monocytes differentiating into Ly6G$^+$ Macs could phagocytose GMP-derived myeloid cells, such as neutrophils, *in vivo*. Interestingly, such a process has been shown to trigger a metabolic rewiring that is associated with Arg-1 activity and aerobic respiration and is important for the resolution of inflammation and tissue repair (*54*, *55*). Third, we provided evidence that GM-CSF and type 2 cytokine signaling through the IL-4 receptor are involved in generation of Ly6G$^+$ Macs and their function. While the cellular source of type 2 cytokines remains unknown, a peak of T helper type 2 (Th2) and type 2 innate lymphoid cells (ILC2s) has been reported in lungs of IAV-infected mice around day 10 post-infection (*56*), a time point that coincides with the peak of Ly6G$^+$ Macs. Moreover, Ly6G$^+$ Macs can release the Th2-attracting and ILC2-activating signals CCL22 and IL-33, respectively, consistent with the idea that Ly6G$^+$ Macs can contribute to the type 2 milieu that promotes their repair phenotype (*57–59*). Fourth, we found that Ly6G$^+$ Macs were spatially-restricted to perilesional areas, zones that were enriched in transitional epithelial cell states involved in AT2-mediated alveolar regeneration (*38*). Perilesional

areas were also sites of intense cytoskeleton activity, aerobic respiration, extracellular matrix deposition and cell migration, all of which are involved in active alveolar epithelial regeneration (*3*, *9*, *41*). Our findings are in line with a previous report that identified damaged zones of IAV-infected lungs that were in the periphery of consolidated areas and were sites of active tissue regeneration and AT2 cell proliferation and differentiation (*47*).

By disrupting myeloid-specific cMaf and MafB-dependent pathways, we obtained *Maf/Mafb*^{MyleoKO} mice in which Ly6G$^+$ Macs were no longer able to differentiate post-IAV, thus representing a valuable tool to address their functions. We identified Ly6G$^+$ Macs as essential actors to license optimal alveolar epithelial regeneration requiring the differentiation of progenitor AT2 cells towards AT1 cells (*41*). In the absence of Ly6G$^+$ Macs, AT2-to-AT1 transitioning cells were virtually absent and a more pronounced dysplastic alveolar repair associated with a bronchiolization of the alveoli was observed. Such epithelial phenotype was associated with exacerbated morbidity and is reminiscent of what is observed in severe forms of respiratory viral infections (*3*, *41*). Additionally, local adoptive transfer of Ly6G$^+$ Macs in IAV-infected *Maf/Mafb*^{MyeloKO} mice improved weight recovery and restored AT2 numbers to levels seen in IAV-infected control mice, suggesting that Ly6G$^+$ Macs could support AT2 expansion post-injury. We further dissected the underlying mechanisms *ex vivo* and found that Ly6G$^+$ Macs could directly promote wound healing of murine AT2 cells through IL-4 receptor-mediated release of soluble factors. Among these factors, osteopontin is expressed by Ly6G$^+$ Macs and is a ligand for the receptor CD44 (*60*). Of note, CD44^{hi} AT2 cells represent a subset of AT2 cells with stem cell properties (*61*), consistent with the hypothesis that the osteopontin-CD44 axis might trigger alveolar regeneration, even though osteopontin release was not potentiated by type 2 cytokine stimulation of Ly6G$^+$ Macs under the experimental conditions tested. The elevated Arg-1 expression by Ly6G$^+$ Macs could also influence AT2 cells, either via the local deprivation of L-Arginine or the generation of ornithine and polyamines (*62*, *63*). Finally, Ly6G$^+$ Macs can also secrete pro-inflammatory cytokines, such as IL-1 and TNF-α, which have been shown to support alveolar regeneration (*38*, *64*).

In the last part of the work, we provided evidence that Macs similar to Ly6G$^+$ Macs are part of a host response to injury that is independent of the organ or the initial trigger and that is conserved across species. Indeed, we found that Ly6G$^+$ Macs were also recruited in a bleomycin-induced model of non-infectious lung injury and in a model of acute acetaminophen-induced liver injury in mice. Even though Ly6G$^+$ Mac numbers were lower in these models compared to the IAV model, it is noteworthy that the peak of Ly6G$^+$ Macs correlated with the presence of damage, as attested by the drop in AT1 and AT2 in the lungs or the release of the hepatic enzyme ALT in the liver. These data are consistent with the idea that they may contribute to tissue repair in these models as well, even though it remains to be addressed experimentally. Interestingly, we also reported the presence of transcriptionally similar Macs in the BALF of pneumonia patients by performing scRNA-seq analyses of BALF cells. Of note, cells exhibiting an elevated Ly6G$^+$ Mac score belonged to a cluster identified as Mo-Macs, and SCENIC analyses suggested that such Mo-Macs displayed high MAF and MAFB activities, reminiscent of Ly6G$^+$ Macs in mice. Speculating that such Mo-Macs also depend on GM-CSF and exhibit similar reparative functions in human lungs, our findings provide a rationale to investigate the benefits of inhaled GM-CSF, beyond the restoration of the AM niche (*65*), to improve epithelial regeneration after severe viral-induced disorders. Indeed, one could speculate that the fate or functions of Ly6G$^+$ Macs are modified and become dysregulated in uncontrolled forms of respiratory viral infections or in chronic fibrotic diseases. Of note, *SPP1*, which encodes osteopontin, has been linked to fibrosis and is often used as a proxy for "pro-fibrotic", pathogenic Macs (*48*, *66–68*). Our data support that Spp1$^+$ Mo-Macs,

like Ly6G$^+$ Macs, can also exert beneficial roles, while other Spp1$^+$ Mo-Macs can become dysregulated, persistent and pathogenic, like in chronic Covid-19 or idiopathic pulmonary fibrosis. Understanding what drives beneficial or pathological responses of *SPP1*$^+$ Macs represents an interesting avenue for future research.

No therapeutic options exist to promote lung regeneration so far. By characterizing in-depth a short-lived atypical Mac population that licenses alveolar regeneration post-injury, our findings could serve as a basis to devise novel myeloid-centered regenerative strategies for medically relevant conditions such as severe or chronic respiratory viral infections or acute respiratory distress syndrome.

Materials and Methods

Study design

In this study, we investigated the spatio-temporal distribution, transcriptional regulation, fate, identity and function of Ly6G$^+$ Macs in an infectious model of lung injury. To this end, we employed flow cytometry, microscopy, single-cell and spatial transcriptomic approaches, bone marrow (BM) chimeras, monocyte fate-mapping and gene targeting. In most of the mouse experiments, 4 to 10 mice per group per time point were used to identify differences between groups with at least 80% power and 5% significance level. In some experiments, no statistical methods were used to pre-determine sample sizes but our sample sizes are similar to those reported in previous publications (*39*, *69*, *74*, *75*). No statistical methods to pre-determine sample size were used for the analyses of human BALF cells from pneumonia patients. Data from independent experiments were pooled for analysis in each data panel, unless otherwise indicated. No data were excluded from the analyses and all attempts at replication were successful and gave similar results. Histopathological examination of lung sections was blinded. Allocation of animals into experimental groups was done randomly at the start of the experiments. The specific numbers of mice, the number of experimental replicates and the statistical tests performed are all included in the respective figure legends.

Mice

All experiments, unless otherwise specified, were performed on age-matched 8–12-wk-old male and female mice on the C57BL/6 background. Details about the transgenic strains can be found in the Supplementary Materials. Mice were housed under specific pathogen-free conditions and maintained in a 12-h light–dark cycle with food and water ad libitum. All animal experiments described in this study were carried out in an animal biosafety level 3 containment unit. Experiments were reviewed and approved by the Institutional Animal Care and Use Committee of the University of Liège (ethical approval #2276). The 'Guide for the Care and Use of Laboratory Animals,' prepared by the Institute of Laboratory Animal Resources, National Research Council, and published by the National Academy Press, as well as European and local legislations, was followed carefully. Accordingly, the temperature and relative humidity were 21°C and 45-60%, respectively

In vivo models of injury

The mouse-adapted influenza strain A/Puerto Rico/8/34 (H1N1; PR8) was kindly provided by F. Trottein (Institut Pasteur, France). The viral stock suspension (10^8 Plaque Forming Units [PFU] ml^{-1}) was diluted and 5 PFU were administered intranasally (i.n.) to isoflurane-anesthetized mice in 50 µl of PBS (Thermo Fisher). Control groups received an equal volume of PBS i.n. for mock infection.

For bleomycin-induced lung injury, isoflurane-anesthetized mice were treated intratracheally (i.t.) with a single instillation of 0.06 IU of bleomycin (Bio-Connect) in a volume of 50µl PBS. Control animals received 50µl PBS alone.

For acetaminophen-induced liver injury, mice were fasted during 15 hours with free access to water and were injected intraperitoneally (i.p.) with 300mg kg^{-1} of acetaminophen (Sigma) in saline solution (NaCl 0.9%). Free access to food was allowed after treatment.

Reagents and antibodies

A complete list of the reagents and antibodies used in this manuscript can be found in Tables S2 and S3, respectively.

Flow cytometry

Staining reactions were performed in the dark at 4°C for 30 minutes with 2% v/v of Fc block (BD Biosciences) to avoid nonspecific binding. For intracellular staining, extracellular-stained cells were fixed and permeabilized with the Foxp3/Transcription factor Staining Buffer Set (Thermo Fisher). For EdU staining, extracellular-stained cells were permeabilized and stained using Click-iT EdU Alexa Fluor 488 Flow Cytometry Assay Kit (Thermo Fisher), according to the manufacturer's instructions.

Cell viability was assessed using 7-AAD (BD Bioscience) or Fixable Viability Dye eFluor™ 780 (Thermo Fisher). Cell suspensions was analysed with a FACSCANTO II or a LSRFortessa (BD Biosciences). Results were analyzed using FlowJo software (Tree Star). For scRNA-seq, transmission electron microscopy, cytological examination and *ex vivo* experiments, lung myeloid cells were sorted using a FACSAria III (BD Biosciences) or a Sony MA900.

***In vivo* treatments**

For EdU incorporation experiments shown in fig. S3, B and C, mice were injected i.p. at day 10 post-IAV with 1 mg EdU (Santa Cruz Biotechnology) in 200 µl PBS 4 hours before sacrifice. For experiments addressing the lifespan of $Ly6G^+$ Macs (Fig. 3G), 1mg EdU in 200 µl PBS was injected i.p. twice 5 hours apart at day 7 post-IAV, and EdU incorporation was evaluated in blood leucocytes at day 8 post-IAV. The incorporation of EdU in lung myeloid cells was evaluated at days 10, 14 and 17 post-IAV. Assessment of phagocytic activity was performed as previously described (*69*). Briefly, isoflurane-anesthetized mice were instilled i.t. with 2.10^8 pHrodo™ Green E. coli BioParticules (Thermo Fisher) in 100 µl PBS. Lungs were harvested 3 hours later for flow cytometry analyses.

Generation of BM (competitive) chimeras

CD45.2, CD45.1 or CD45.1/CD45.2 WT mice were anesthetized by i.p. injection of 200 µl PBS containing ketamine (Nimatek, Dechra, 75 mg kg^{-1}) and xylazine (Rompun, Bayer, 10 mg kg^{-1}). When mentioned, the thoracic cavity was protected with a 0.6-cm-thick lead cover. Mice were irradiated with two consecutive doses of 6 Gy 15 minutes apart. Once recovered from the anaesthesia, mice were reconstituted by intravenous (i.v.) administration of 2.10^6 BM cells from *Ms4a3*^{tdtom} or *Il4ra*$^{-/-}$ mice, for full chimeras. For mixed BM chimeras, mice were reconstituted i.v. with 2.10^6 BM cells consisting of a 1:1 mix of BM cells obtained from the following mice: CD45.1 WT, *Ms4a3*^{tdtom}, *Ccr2*$^{-/-}$, CD45.1 *Csf2ra*$^{-/-}$, CD45.2 *Csf2ra*$^{+/+}$, *Cx3cr1*$^{GFP+}$, *Il4ra*$^{-/-}$, or homozygous *Ly6g*^{CreERT2} mice *(*also called *Ly6g*$^{-/-}$ mice). From the day of irradiation, mice were treated for 4 weeks with 0.05 mg ml^{-1} of enrofloxacin (Baytril, Bayer) in drinking water. Chimerism was assessed by flow cytometry in the blood 4 weeks after irradiation.

scRNA-sequencing and analyses

For mouse experiments, lung myeloid cells were FACS-sorted as living singlet $CD45^+$, $F4/80^+$ and/or $CD11b^+$ cells from lung single-cell suspensions pooled from 5 mock-infected and IAV-infected C57BL/6 male WT mice at day 10 post-IAV. For each sample, an aliquot of Trypan blue-treated cells was examined under the microscope for counting, viability and aggregate assessment following FACS sorting. Viability was above 90% for all samples and no aggregates were observed. Cell preparations were centrifuged and pellets were resuspended in calcium- and

magnesium-free PBS containing 0.4 mg ml^{-1} UltraPure BSA (Thermo Fisher Scientific). The 10X Genomics platform (Single Cell 3' Solution) was used. For library preparation, approximately 2,000 (Mock group) and 6,000 (IAV group) cells were loaded into the Chromium Controller, in which they were partitioned, their polyA RNAs captured and barcoded using Chromium Single Cell 3' GEM, Library & Gel Bead Kit v3 (10X Genomics). The cDNAs were amplified and libraries compatible with Illumina sequencers were generated using Chromium Single Cell 3' GEM, Library & Gel Bead Kit v3 (10X Genomics).

For human BALF cell analyses, chromium Fixed RNA Profiling for multiplexed samples (10X Genomics) was used for scRNA-seq analysis of human BALF cells, allowing the storage of fixed cells and enabling analysis of multiple samples in one single GEM reaction. Fresh samples were directly fixed in a 4% formaldehyde solution after collection for storage at -80°C. For GEM creation, the Multiplex-compatible Chromium Next GEM Single Cell Fixed RNA Human Transcriptome Probe Kit including a Probe Barcode that permits sample multiplexing and subsequent demultiplexing was used.

Details about scRNA-seq analyses can be found in the Supplementary Materials.

Transmission electron microscopy

FACS-sorted myeloid cell populations or lung tissues from IAV-infected mice at day 10 post-IAV were fixed in 2.5% glutaraldehyde (diluted in Sorensen's buffer: 0.1 M Na2HPO4/NaH2PO4 buffer, pH 7.4) for 1h at 4 °C and postfixed for 30 min in 2% OsO4 (diluted in 0.1 M Sorensen's Buffer). After dehydration in graded ethanol, samples were embedded in Epon resin. Ultrathin sections obtained with a Reichert Ultracut S ultramicrotome (Reichert Technologies) were contrasted with 2% uranyl acetate and 4% lead citrate. For ultrastructural analyses, random fields of cells were examined under a Jeol TEM JEM-1400 Transmission Electron Microscope at 80 kV, and photographed using an 11-megapixel camera system (Quemesa, Olympus).

Extracellular flux analysis

Oxygen consumption rate (OCR) was measured using Seahorse XF Cell Mito Stress Test (Agilent) according to manufacturer's recommendations and as described previously (*70*, *71*). Briefly, Neu, IM-like cells and Ly6G$^+$ Macs were FACS-sorted at day 10 post-IAV and seeded (10.10^4, 7.10^4 and 8.10^4 cells/well, respectively) in XFp mini-plates (Agilent) pre-coated with CellTak. Cells were kept in unbuffered serum-free DMEM supplemented with pyruvate (1mM), glutamine (2mM), glucose (10mM), at pH 7.4, 37 °C and ambient CO_2 for 1h before the assay. Analysis was performed using the XFp analyser (Seahorse Bioscience) as per manufacturer's instructions. Additional details can be found in the Supplementary Materials.

Spatial transcriptomic analyses using Digital Spatial Profiling (DSP)

Five-µm-thick formalin-fixed, paraffin-embedded (FFPE) sections were prepared using the protocol from NanoString Technologies. Briefly, 2 tissue slides, each containing 1 mock and 2 IAV samples harvested 10 days post-IAV, were analyzed. Slides were first stained with antibodies against CD68, Ly6G (clone 1A8), and DNA was visualized with 500 nM Syto83. Mouse Whole Transcriptome Atlas probes targeting more than 19,000 targets were hybridized, and slides were loaded on the GeoMx DSP. Briefly, entire slides were imaged at x20 magnification, and Regions of Interest (ROIs) were chosen based on serial Hematoxylin & Eosin sections and on morphological markers to select lesional, perilesional and extralesional areas. ROIs were exposed to ultraviolet light, releasing the indexing oligos and collecting them in a 96-well plate for

subsequent processing and sequencing, as described (*72*). Raw count, third quartile (Q3)–normalized count data of target genes from ROIs were provided by the vendor, which were used as input to downstream analyses. Additional details can be found in the Supplementary Materials.

Immunofluorescence

Immunofluorescence staining of mouse lungs were performed as previously described (*39*). Briefly, lungs from WT or *Cx3cr1*$^{GFP+}$ mice were perfused with 5 ml PBS through the right ventricle then with 5 ml paraformaldehyde (PFA) 4% (Thermo Fisher) in PBS, and lungs were collected. Lungs were fixed for 4 h in 4% PAF at 4 °C, then cryoprotected overnight in 30% sucrose (VWR) in PBS at 4 °C, followed by embedding in optimal cutting temperature compound (OCT) (VWR) and stored at −80 °C. Seven-µm-thick sections were cut and left in a methanol 100% (Merck) bath at −20 °C for 20 minutes prior to be stained. Additional details can be found in the Supplementary Materials. All images were acquired on an LSM 980 with Airyscan 2 inverted confocal microscope (Zeiss) using a LD C-Apochromat ×40/1.1 W objective and Zen Black software. Additional details can be found in the Supplementary Materials.

***Ex vivo* experiments**

For *ex vivo* stimulation and co-culture experiments, single cell suspensions isolated from IAV-infected lungs of WT or *Ly6g*^{tdTom} mice at day 10 post-IAV were enriched in CD11b^{+} cells by a magnetic-activated cell sorting (MACS) using CD11b MicroBeads (Myltenyi). Cells were then stained and FACS-sorted using the gating strategy shown in Fig. 1A. After sorting, cells were counted, spinned down, and either directly added to the co-culture with MLE-12 cells, or seeded in 96 wells at a concentration 5.10^{4} cells/well in complete RPMI (ThermoFischer), containing 1mM sodium pyruvate, 1% vol/vol MEM non-essential amino acids, 50 U ml^{-1} Penicillin-Streptomycin and 10% vol/vol FBS. For stimulation experiments, recombinant mouse GM-CSF (20 ng ml^{-1}, Peprotech), mouse M-CSF (20 ng ml^{-1}, Peprotech), mouse IL-4 (20 ng ml^{-1}, Peprotech) or mouse IL-13 (20 ng ml^{-1}, Peprotech) were added. When required, Cre-ERT2 activation was achieved by adding 0.02 mg ml^{-1} of 4-hydroxytamoxifen (Sigma-Aldrich). After 18 hours of culture, cell supernatants were collected (conditioned medium, CM) and cells were harvested for flow cytometry phenotyping.

Murine lung epithelial (MLE)-12 cells (ATCC, CVCL_3751) were used. Scratch Wound Assay were performed using IncucyteS3 (Sartorius). MLE-12 cells were seeded in 96-well (Sartorius) at density of 4.10^{4} cells/well and incubated 24 hours in DMEM/F12 medium. An open wound area was created in the cell monolayer using the IncuCyte ® Wound Maker tool, and subsequently co-cultured with FCAS-sorted cells or incubated with CM from unpulsed or IL-4/IL-13-pulsed Ly6G^{+} Macs.

Additional details can be found in the Supplementary Materials.

Adoptive transfer of Ly6G^{+} Macs *in vivo*

Ly6G^{+} Macs were isolated from the lungs of CD45.2 WT mice at day 10 poist-IAV. Lung single cell suspensions were first enriched in CD11b^{+} cells by MACS using CD11b MicroBeads (Miltenyi Biotec) and were FACS-sorted using a Sony MA900. Four hundred thousand (4 x 10^{5}) Ly6G^{+} Macs were resuspended in 50 µl sterile PBS and were instilled i.t. in lightly isoflurane-anesthetized *Maf/Mafb*^{MyeloKO} mice at days 8, 11, 13, 15 post-IAV. Control *Maf/Mafb*^{MyeloKO} mice and WT mice received 50 µl PBS as vehicle.

Human BALFs

The use of human BALF cells was approved in 2022 by the Ethics Reviewing Board of the University Hospital of Liege, Belgium (ref. 2022/159). The characteristics of the patients are summarized in Table S1. Human BALFs were fixed directly after collection for storage and scRNA-seq analyses.

Statistical analysis

Graphs were prepared with GraphPad Prism 9 (GraphPad software) or R Bioconductor (3.5.1) (*73*). Data distribution was assumed to be normal when parametric tests were performed. Data from independent experiments were pooled for analysis in each data panel, unless otherwise indicated. No data were excluded from the analyses. Statistical analyses were performed with Prism 9 (GraphPad software), and with R Bioconductor (3.5.1) (*73*) and Seurat (*76*) for scRNA-seq data, respectively. The statistical analyses performed for each experiment are indicated in the respective figure legends. We considered a *P* value lower than 0.05 to be significant (*, $P < 0.05$; **, $P < 0.01$; ***, $P < 0.001$; ****, $P < 0.0001$; ns, not significant).

Additional sections and details about Materials and Methods can be found in the Supplemental Materials.

Supplementary Materials

References and notes

1. A. C. Kalil, P. G. Thomas, Influenza virus-related critical illness: pathophysiology and epidemiology. *Crit Care* **23**, 258 (2019).

2. S. Herold, C. Becker, K. M. Ridge, G. R. S. Budinger, Influenza virus-induced lung injury: pathogenesis and implications for treatment. *Eur Respir J* **45**, 1463–1478 (2015).

3. X. Wei, H. Narasimhan, B. Zhu, J. Sun, Host Recovery from Respiratory Viral Infection. *Annu Rev Immunol*, **41**, 277-300 (2023).

4. Burden of disease - Global Influenza Programme. https://www.who.int/teams/global-influenza-programme/surveillance-and-monitoring/burden-of-disease.

5. A. D. Iuliano, K. M. Roguski, H. H. Chang, D. J. Muscatello, R. Palekar, S. Tempia, C. Cohen, J. M. Gran, D. Schanzer, B. J. Cowling, P. Wu, J. Kyncl, L. W. Ang, M. Park, M. Redlberger-Fritz, H. Yu, L. Espenhain, A. Krishnan, G. Emukule, L. van Asten, S. Pereira da Silva, S. Aungkulanon, U. Buchholz, M.-A. Widdowson, J. S. Bresee, Global Seasonal Influenza-associated Mortality Collaborator Network, Estimates of global seasonal influenza-associated respiratory mortality: a modelling study. *Lancet* **391**, 1285–1300 (2018).

6. P. Bost, A. Giladi, Y. Liu, Y. Bendjelal, G. Xu, E. David, R. Blecher-Gonen, M. Cohen, C. Medaglia, H. Li, A. Deczkowska, S. Zhang, B. Schwikowski, Z. Zhang, I. Amit, Host-Viral Infection Maps Reveal Signatures of Severe COVID-19 Patients. *Cell* **181**, 1475-1488.e12 (2020).

7. M. Merad, J. C. Martin, Pathological inflammation in patients with COVID-19: a key role for monocytes and macrophages. *Nat Rev Immunol* **20**, 355–362 (2020).

8. M. Guilliams, A. Mildner, S. Yona, Developmental and Functional Heterogeneity of Monocytes. *Immunity* **49**, 595–613 (2018).

9. C. Ruscitti, C. Radermecker, T. Marichal, Journey of monocytes and macrophages upon influenza A virus infection. *Curr Opin Virol* **66**, 101409 (2024).

10. L. Rodriguez-Rodriguez, L. Gillet, B. Machiels, Shaping of the alveolar landscape by respiratory infections and long-term consequences for lung immunity. *Front Immunol* **14** (2023).

11. B. Machiels, M. Dourcy, X. Xiao, J. Javaux, C. Mesnil, C. Sabatel, D. Desmecht, F. Lallemand, P. Martinive, H. Hammad, M. Guilliams, B. Dewals, A. Vanderplasschen, B. N. Lambrecht, F. Bureau, L. Gillet, A gammaherpesvirus provides protection against allergic asthma by inducing the replacement of resident alveolar macrophages with regulatory monocytes. *Nat Immunol* **18**, 1310–1320 (2017).

12. H. Aegerter, J. Kulikauskaite, S. Crotta, H. Patel, G. Kelly, E. M. Hessel, M. Mack, S. Beinke, A. Wack, Influenza-induced monocyte-derived alveolar macrophages confer prolonged antibacterial protection. *Nat Immunol* **21**, 145–157 (2020).

13. H. Aegerter, B. N. Lambrecht, C. V. Jakubzick, Biology of lung macrophages in health and disease. *Immunity* **55**, 1564–1580 (2022).

14. M. Guilliams, F. R. Svedberg, Does tissue imprinting restrict macrophage plasticity? *Nat Immunol* **22**, 118–127 (2021).

15. F. Li, F. Piattini, L. Pohlmeier, Q. Feng, H. Rehrauer, M. Kopf, Monocyte-derived alveolar macrophages autonomously determine severe outcome of respiratory viral infection. *Sci Immunol* **7**, eabj5761 (2022).

16. K. L. Lin, Y. Suzuki, H. Nakano, E. Ramsburg, M. D. Gunn, CCR2+ monocyte-derived dendritic cells and exudate macrophages produce influenza-induced pulmonary immune pathology and mortality. *J Immunol* **180**, 2562–2572 (2008).

17. S. T. Chen, M. D. Park, D. M. Del Valle, M. Buckup, A. Tabachnikova, R. C. Thompson, N. W. Simons, K. Mouskas, B. Lee, D. Geanon, D. D'Souza, T. Dawson, R. Marvin, K. Nie, Z. Zhao, J. LeBerichel, C. Chang, H. Jamal, G. Akturk, U. Chaddha, K. Mathews, S. Acquah, S.-A. Brown, M. Reiss, T. Harkin, M. Feldmann, C. A. Powell, J. L. Hook, S. Kim-Schulze, A. H. Rahman, B. D. Brown, Mount Sinai COVID-19 Biobank Team, N. D. Beckmann, S. Gnjatic, E. Kenigsberg, A. W. Charney, M. Merad, A shift in lung macrophage composition is associated with COVID-19 severity and recovery. *Sci Transl Med* **14**, eabn5168 (2022).

18. M. D. Park, A. Silvin, F. Ginhoux, M. Merad, Macrophages in health and disease. *Cell* **185**, 4259–4279 (2022).

19. T. A. Wynn, K. M. Vannella, Macrophages in Tissue Repair, Regeneration, and Fibrosis. *Immunity* **44**, 450–62 (2016).

20. S. P. Nobs, M. Kopf, Tissue-resident macrophages: guardians of organ homeostasis. *Trends Immunol* **42**, 495–507 (2021).

21. F. Ginhoux, M. Guilliams, Tissue-Resident Macrophage Ontogeny and Homeostasis. *Immunity* **44**, 439–49 (2016).

22. F.-F. Huang, P. F. Barnes, Y. Feng, R. Donis, Z. C. Chroneos, S. Idell, T. Allen, D. R. Perez, J. A. Whitsett, K. Dunussi-Joannopoulos, H. Shams, GM-CSF in the lung protects against lethal influenza infection. *Am J Respir Crit Care Med* **184**, 259–268 (2011).

23. C. Schneider, S. P. Nobs, A. K. Heer, M. Kurrer, G. Klinke, N. van Rooijen, J. Vogel, M. Kopf, Alveolar macrophages are essential for protection from respiratory failure and associated morbidity following influenza virus infection. *PLoS Pathog* **10**, e1004053 (2014).

24. B. B. Ural, S. T. Yeung, P. Damani-Yokota, J. C. Devlin, M. de Vries, P. Vera-Licona, T. Samji, C. M. Sawai, G. Jang, O. A. Perez, Q. Pham, L. Maher, P. Loke, M. Dittmann, B. Reizis, K. M. Khanna, Identification of a nerve-associated, lung-resident interstitial macrophage subset with distinct localization and immunoregulatory properties. *Sci Immunol* **5**, eaax8756 (2020).

25. C. C. Bain, A. S. MacDonald, The impact of the lung environment on macrophage development, activation and function: diversity in the face of adversity. *Mucosal Immunol* **15**, 223-234 (2022).

26. J. Chen, M.-C. Zhong, H. Guo, D. Davidson, S. Mishel, Y. Lu, I. Rhee, L.-A. Pérez-Quintero, S. Zhang, M.-E. Cruz-Munoz, N. Wu, D. C. Vinh, M. Sinha, V. Calderon, C. A. Lowell, J. S. Danska, A. Veillette, SLAMF7 is critical for phagocytosis of haematopoietic tumour cells via Mac-1 integrin. *Nature* **544**, 493–497 (2017).

27. Y. Wu, Q. Wang, M. Li, J. Lao, H. Tang, S. Ming, M. Wu, S. Gong, L. Li, L. Liu, X. Huang, SLAMF7 regulates the inflammatory response in macrophages during polymicrobial sepsis. *J Clin Invest* **133**, e150224 (2023).

28. G. X. Zheng, J. M. Terry, P. Belgrader, P. Ryvkin, Z. W. Bent, R. Wilson, S. B. Ziraldo, T. D. Wheeler, G. P. McDermott, J. Zhu, M. T. Gregory, J. Shuga, L. Montesclaros, J. G. Underwood, D. A. Masquelier, S. Y. Nishimura, M. Schnall-Levin, P. W. Wyatt, C. M. Hindson, R. Bharadwaj, A. Wong, K. D. Ness, L. W. Beppu, H. J. Deeg, C. McFarland, K. R. Loeb, W. J. Valente, N. G. Ericson, E. A. Stevens, J. P. Radich, T. S. Mikkelsen, B. J. Hindson, J. H. Bielas, Massively parallel digital transcriptional profiling of single cells. *Nat Commun* **8**, 14049 (2017).

29. D. Vanneste, Q. Bai, S. Hasan, W. Peng, D. Pirottin, J. Schyns, P. Maréchal, C. Ruscitti, M. Meunier, Z. Liu, C. Legrand, L. Fievez, F. Ginhoux, C. Radermecker, F. Bureau, T. Marichal, MafB-restricted local monocyte proliferation precedes lung interstitial macrophage differentiation. *Nat Immunol* **24**, 827-840 (2023).

30. C. Sabatel, C. Radermecker, L. Fievez, G. Paulissen, S. Chakarov, C. Fernandes, S. Olivier, M. Toussaint, D. Pirottin, X. Xiao, P. Quatresooz, J. C. Sirard, D. Cataldo, L. Gillet, H. Bouabe, C. J. Desmet, F. Ginhoux, T. Marichal, F. Bureau, Exposure to Bacterial CpG DNA Protects from Airway Allergic Inflammation by Expanding Regulatory Lung Interstitial Macrophages. *Immunity* **46**, 457–473 (2017).

31. Z. Liu, Y. Gu, S. Chakarov, C. Bleriot, I. Kwok, X. Chen, A. Shin, W. Huang, R. J. Dress, C.-A. Dutertre, A. Schlitzer, J. Chen, L. G. Ng, H. Wang, Z. Liu, B. Su, F. Ginhoux, Fate Mapping via Ms4a3-Expression History Traces Monocyte-Derived Cells. *Cell* **178**, 1509-1525.e19 (2019).

32. K. Street, D. Risso, R. B. Fletcher, D. Das, J. Ngai, N. Yosef, E. Purdom, S. Dudoit, Slingshot: cell lineage and pseudotime inference for single-cell transcriptomics. *BMC Genomics* **19**, 477 (2018).

33. S. Yona, K. W. Kim, Y. Wolf, A. Mildner, D. Varol, M. Breker, D. Strauss-Ayali, S. Viukov, M. Guilliams, A. Misharin, D. A. Hume, H. Perlman, B. Malissen, E. Zelzer, S. Jung, Fate mapping reveals origins and dynamics of monocytes and tissue macrophages under homeostasis. *Immunity* **38**, 79–91 (2013).

34. N. V. Serbina, E. G. Pamer, Monocyte emigration from bone marrow during bacterial infection requires signals mediated by chemokine receptor CCR2. *Nat Immunol* **7**, 311–7 (2006).

35. T. Satoh, K. Nakagawa, F. Sugihara, R. Kuwahara, M. Ashihara, F. Yamane, Y. Minowa, K. Fukushima, I. Ebina, Y. Yoshioka, A. Kumanogoh, S. Akira, Identification of an atypical monocyte and committed progenitor involved in fibrosis. *Nature* **541**, 96–101 (2017).

36. S. Aibar, C. B. González-Blas, T. Moerman, V. A. Huynh-Thu, H. Imrichova, G. Hulselmans, F. Rambow, J.-C. Marine, P. Geurts, J. Aerts, J. van den Oord, Z. K. Atak, J. Wouters, S. Aerts, SCENIC: single-cell regulatory network inference and clustering. *Nat. Methods* **14**, 1083–1086 (2017).

37. I. Ballesteros, A. Rubio-Ponce, M. Genua, E. Lusito, I. Kwok, G. Fernández-Calvo, T. E. Khoyratty, E. van Grinsven, S. González-Hernández, J. Á. Nicolás-Ávila, T. Vicanolo, A. Maccataio, A. Benguría, J. L. Li, J. M. Adrover, A. Aroca-Crevillen, J. A. Quintana, S. Martín-Salamanca, F. Mayo, S. Ascher, G. Barbiera, O. Soehnlein, M. Gunzer, F. Ginhoux, F. Sánchez-Cabo, E. Nistal-Villán, C. Schulz, A. Dopazo, C. Reinhardt, I. A. Udalova, L. G. Ng, R. Ostuni, A. Hidalgo, Co-option of Neutrophil Fates by Tissue Environments. *Cell* **183**, 1282-1297.e18 (2020).

38. J. Choi, J.-E. Park, G. Tsagkogeorga, M. Yanagita, B.-K. Koo, N. Han, J.-H. Lee, Inflammatory Signals Induce AT2 Cell-Derived Damage-Associated Transient Progenitors that Mediate Alveolar Regeneration. *Cell Stem Cell* **27**, 366-382.e7 (2020).

39. D. Vanneste, Q. Bai, S. Hasan, W. Peng, D. Pirottin, J. Schyns, P. Maréchal, C. Ruscitti, M. Meunier, Z. Liu, C. Legrand, L. Fievez, F. Ginhoux, C. Radermecker, F. Bureau, T. Marichal, MafB-restricted local monocyte proliferation precedes lung interstitial macrophage differentiation. *Nat Immunol* **24**, 827–840 (2023).

40. I. Y. Adamson, D. H. Bowden, The type 2 cell as progenitor of alveolar epithelial regeneration. A cytodynamic study in mice after exposure to oxygen. *Lab Invest* **30**, 35–42 (1974).

41. J. D. Planer, E. E. Morrisey, After the Storm: Regeneration, Repair, and Reestablishment of Homeostasis Between the Alveolar Epithelium and Innate Immune System Following Viral Lung Injury. *Annu Rev Pathol* **18**, 337–359 (2023).

42. C. M. Minutti, L. H. Jackson-Jones, B. García-Fojeda, J. A. Knipper, T. E. Sutherland, N. Logan, E. Ringqvist, R. Guillamat-Prats, D. A. Ferenbach, A. Artigas, C. Stamme, Z. C. Chroneos, D. M. Zaiss, C. Casals, J. E. Allen, Local amplifiers of IL-4Rα-mediated macrophage activation promote repair in lung and liver. *Science* **356**, 1076–1080 (2017).

43. L. Bosurgi, Y. G. Cao, M. Cabeza-Cabrerizo, A. Tucci, L. D. Hughes, Y. Kong, J. S. Weinstein, P. Licona-Limon, E. T. Schmid, F. Pelorosso, N. Gagliani, J. E. Craft, R. A. Flavell, S. Ghosh, C. V. Rothlin, Macrophage function in tissue repair and remodeling requires IL-4 or IL-13 with apoptotic cells. *Science* **356**, 1072–1076 (2017).

44. M. C. Basil, J. Katzen, A. E. Engler, M. Guo, M. J. Herriges, J. J. Kathiriya, R. Windmueller, A. B. Ysasi, W. J. Zacharias, H. A. Chapman, D. N. Kotton, J. R. Rock, H.-W. Snoeck, G. Vunjak-Novakovic, J. A. Whitsett, E. E. Morrisey, The Cellular and Physiological Basis for Lung Repair and Regeneration: Past, Present, and Future. *Cell Stem Cell* **26**, 482–502 (2020).

45. W. J. Zacharias, D. B. Frank, J. A. Zepp, M. P. Morley, F. A. Alkhaleel, J. Kong, S. Zhou, E. Cantu, E. E. Morrisey, Regeneration of the lung alveolus by an evolutionarily conserved epithelial progenitor. *Nature* **555**, 251–255 (2018).

46. A. N. Nabhan, D. G. Brownfield, P. B. Harbury, M. A. Krasnow, T. J. Desai, Single-cell Wnt signaling niches maintain stemness of alveolar type 2 cells. *Science* **359**, 1118–1123 (2018).

47. D. C. Liberti, M. M. Kremp, W. A. Liberti, I. J. Penkala, S. Li, S. Zhou, E. E. Morrisey, Alveolar epithelial cell fate is maintained in a spatially restricted manner to promote lung regeneration after acute injury. *Cell Rep* **35**, 109092 (2021).

48. A. V. Misharin, L. Morales-Nebreda, P. A. Reyfman, C. M. Cuda, J. M. Walter, A. C. McQuattie-Pimentel, C.-I. Chen, K. R. Anekalla, N. Joshi, K. J. N. Williams, H. Abdala-Valencia, T. J. Yacoub, M. Chi, S. Chiu, F. J. Gonzalez-Gonzalez, K. Gates, A. P. Lam, T. T. Nicholson, P. J. Homan, S. Soberanes, S. Dominguez, V. K. Morgan, R. Saber, A. Shaffer, M. Hinchcliff, S. A. Marshall, A. Bharat, S. Berdnikovs, S. M. Bhorade, E. T. Bartom, R. I. Morimoto, W. E. Balch, J. I. Sznajder, N. S. Chandel, G. M. Mutlu, M. Jain, C. J. Gottardi, B. D. Singer, K. M. Ridge, N. Bagheri, A. Shilatifard, G. R. S. Budinger, H. Perlman, Monocyte-derived alveolar macrophages drive lung fibrosis and persist in the lung over the life span. *J Exp Med* **214**, 2387–2404 (2017).

49. P. Y. Lee, J.-X. Wang, E. Parisini, C. C. Dascher, P. A. Nigrovic, Ly6 family proteins in neutrophil biology. *J Leukoc Biol* **94**, 585–594 (2013).

50. L. Cakarova, L. M. Marsh, J. Wilhelm, K. Mayer, F. Grimminger, W. Seeger, J. Lohmeyer, S. Herold, Macrophage tumor necrosis factor-alpha induces epithelial expression of granulocyte-macrophage colony-stimulating factor: impact on alveolar epithelial repair. *Am J Respir Crit Care Med* **180**, 521–532 (2009).

51. Y. Lavin, D. Winter, R. Blecher-Gonen, E. David, H. Keren-Shaul, M. Merad, S. Jung, I. Amit, Tissue-resident macrophage enhancer landscapes are shaped by the local microenvironment. *Cell* **159**, 1312–1326 (2014).

52. L. van de Laar, W. Saelens, S. De Prijck, L. Martens, C. L. Scott, G. Van Isterdael, E. Hoffmann, R. Beyaert, Y. Saeys, B. N. Lambrecht, M. Guilliams, Yolk Sac Macrophages, Fetal Liver, and Adult Monocytes Can Colonize an Empty Niche and Develop into Functional Tissue-Resident Macrophages. *Immunity* **44**, 755–768 (2016).

53. P. Loos, J. Baiwir, C. Maquet, J. Javaux, R. Sandor, F. Lallemand, T. Marichal, B. Machiels, L. Gillet, Dampening type 2 properties of group 2 innate lymphoid cells by a gammaherpesvirus infection reprograms alveolar macrophages. *Sci Immunol* **8**, eabl9041 (2023).

54. M. Schilperoort, D. Ngai, S. R. Sukka, K. Avrampou, H. Shi, I. Tabas, The role of efferocytosis-fueled macrophage metabolism in the resolution of inflammation. *Immunol Rev* **319**, 65-80 (2023).

55. S. Zhang, S. Weinberg, M. DeBerge, A. Gainullina, M. Schipma, J. M. Kinchen, I. Ben-Sahra, D. R. Gius, L. Yvan-Charvet, N. S. Chandel, P. T. Schumacker, E. B. Thorp,

Efferocytosis Fuels Requirements of Fatty Acid Oxidation and the Electron Transport Chain to Polarize Macrophages for Tissue Repair. *Cell Metab* **29**, 443-456.e5 (2019).

56. B. W. S. Li, M. J. W. de Bruijn, M. Lukkes, M. van Nimwegen, I. M. Bergen, A. KleinJan, C. H. GeurtsvanKessel, A. Andeweg, G. F. Rimmelzwaan, R. W. Hendriks, T cells and ILC2s are major effector cells in influenza-induced exacerbation of allergic airway inflammation in mice. *Eur J Immunol* **49**, 144–156 (2019).

57. L. A. Monticelli, G. F. Sonnenberg, M. C. Abt, T. Alenghat, C. G. K. Ziegler, T. A. Doering, J. M. Angelosanto, B. J. Laidlaw, C. Y. Yang, T. Sathaliyawala, M. Kubota, D. Turner, J. M. Diamond, A. W. Goldrath, D. L. Farber, R. G. Collman, E. J. Wherry, D. Artis, Innate lymphoid cells promote lung-tissue homeostasis after infection with influenza virus. *Nat Immunol* **12**, 1045–1054 (2011).

58. R. L. Gieseck, M. S. Wilson, T. A. Wynn, Type 2 immunity in tissue repair and fibrosis. *Nat Rev Immunol* **18**, 62–76 (2018).

59. A. J. Lechner, I. H. Driver, J. Lee, C. M. Conroy, A. Nagle, R. M. Locksley, J. R. Rock, Recruited Monocytes and Type 2 Immunity Promote Lung Regeneration following Pneumonectomy. *Cell Stem Cell* **21**, 120-134.e7 (2017).

60. G. F. Weber, S. Ashkar, M. J. Glimcher, H. Cantor, Receptor-ligand interaction between CD44 and osteopontin (Eta-1). *Science* **271**, 509–512 (1996).

61. Q. Chen, V.S. Kumar, J. Finn, D. Jiang, J. Liang, Y-Y. Zhao, Y. Liu, CD44high alveolar type II cells show stem cell properties during steady-state alveolar homeostasis. *Am J Physiol Lung Cell Mol Physiol* **313**, L41-L51 (2017).

62. K. S. Burrack, T. E. Morrison, The role of myeloid cell activation and arginine metabolism in the pathogenesis of virus-induced diseases. *Front Immunol* **5**, 428 (2014).

63. R. A. Crompton, H. Williams, L. Campbell, L. Hui Kheng, C. Saville, D. M. Ansell, A. Reid, J. Wong, L. A. Vardy, M. J. Hardman, S. M. Cruickshank, An Epidermal-Specific Role for Arginase1 during Cutaneous Wound Repair. *J Invest Dermatol* **142**, 1206-1216.e8 (2022).

64. H. Katsura, Y. Kobayashi, P. R. Tata, B. L. M. Hogan, IL-1 and TNFα Contribute to the Inflammatory Niche to Enhance Alveolar Regeneration. *Stem Cell Reports* **12**, 657–666 (2019).

65. C. Bosteels, K. F. A. Van Damme, E. De Leeuw, J. Declercq, B. Maes, V. Bosteels, L. Hoste, L. Naesens, N. Debeuf, J. Deckers, B. Cole, M. Pardons, D. Weiskopf, A. Sette, Y. V. Weygaerde, T. Malfait, S. J. Vandecasteele, I. K. Demedts, H. Slabbynck, S. Allard, P. Depuydt, E. Van Braeckel, J. De Clercq, L. Martens, S. Dupont, R. Seurinck, N. Vandamme, F. Haerynck, D. F. Roychowdhury, L. Vandekerckhove, M. Guilliams, S. J. Tavernier, B. N. Lambrecht, Loss of GM-CSF-dependent instruction of alveolar macrophages in COVID-19 provides a rationale for inhaled GM-CSF treatment. *Cell Rep Med* **3**, 100833 (2022).

66. P. A. Reyfman, J. M. Walter, N. Joshi, K. R. Anekalla, A. C. McQuattie-Pimentel, S. Chiu, R. Fernandez, M. Akbarpour, C.-I. Chen, Z. Ren, R. Verma, H. Abdala-Valencia, K. Nam,

M. Chi, S. Han, F. J. Gonzalez-Gonzalez, S. Soberanes, S. Watanabe, K. J. N. Williams, A. S. Flozak, T. T. Nicholson, V. K. Morgan, D. R. Winter, M. Hinchcliff, C. L. Hrusch, R. D. Guzy, C. A. Bonham, A. I. Sperling, R. Bag, R. B. Hamanaka, G. M. Mutlu, A. V. Yeldandi, S. A. Marshall, A. Shilatifard, L. A. N. Amaral, H. Perlman, J. I. Sznajder, A. C. Argento, C. T. Gillespie, J. Dematte, M. Jain, B. D. Singer, K. M. Ridge, A. P. Lam, A. Bharat, S. M. Bhorade, C. J. Gottardi, G. R. S. Budinger, A. V. Misharin, Single-Cell Transcriptomic Analysis of Human Lung Provides Insights into the Pathobiology of Pulmonary Fibrosis. *Am J Respir Crit Care Med* **199**, 1517–1536 (2019).

67. C. Morse, T. Tabib, J. Sembrat, K. L. Buschur, H. T. Bittar, E. Valenzi, Y. Jiang, D. J. Kass, K. Gibson, W. Chen, A. Mora, P. V. Benos, M. Rojas, R. Lafyatis, Proliferating SPP1/MERTK-expressing macrophages in idiopathic pulmonary fibrosis. *Eur Respir J* **54** (2019).

68. T. S. Adams, J. C. Schupp, S. Poli, E. A. Ayaub, N. Neumark, F. Ahangari, S. G. Chu, B. A. Raby, G. DeIuliis, M. Januszyk, Q. Duan, H. A. Arnett, A. Siddiqui, G. R. Washko, R. Homer, X. Yan, I. O. Rosas, N. Kaminski, Single-cell RNA-seq reveals ectopic and aberrant lung-resident cell populations in idiopathic pulmonary fibrosis. *Sci Adv* **6**, eaba1983 (2020).

69. J. Schyns, Q. Bai, C. Ruscitti, C. Radermecker, S. De Schepper, S. Chakarov, F. Farnir, D. Pirottin, F. Ginhoux, G. Boeckxstaens, F. Bureau, T. Marichal, Non-classical tissue monocytes and two functionally distinct populations of interstitial macrophages populate the mouse lung. *Nat Commun* **10**, 3964 (2019).

70. M.-J. Nokin, F. Durieux, J. Bellier, O. Peulen, K. Uchida, D. A. Spiegel, J. R. Cochrane, C. A. Hutton, V. Castronovo, A. Bellahcène, Hormetic potential of methylglyoxal, a side-product of glycolysis, in switching tumours from growth to death. *Sci Rep* **7**, 11722 (2017).

71. G. Rademaker, V. Hennequière, L. Brohée, M.-J. Nokin, P. Lovinfosse, F. Durieux, S. Gofflot, J. Bellier, B. Costanza, M. Herfs, R. Peiffer, L. Bettendorff, C. Deroanne, M. Thiry, P. Delvenne, R. Hustinx, A. Bellahcène, V. Castronovo, O. Peulen, Myoferlin controls mitochondrial structure and activity in pancreatic ductal adenocarcinoma, and affects tumor aggressiveness. *Oncogene* **37**, 4398–4412 (2018).

72. K. H. Dinnon, S. R. Leist, K. Okuda, H. Dang, E. J. Fritch, K. L. Gully, G. De la Cruz, M. D. Evangelista, T. Asakura, R. C. Gilmore, P. Hawkins, S. Nakano, A. West, A. Schäfer, L. E. Gralinski, J. L. Everman, S. P. Sajuthi, M. R. Zweigart, S. Dong, J. McBride, M. R. Cooley, J. B. Hines, M. K. Love, S. D. Groshong, A. VanSchoiack, S. J. Phelan, Y. Liang, T. Hether, M. Leon, R. E. Zumwalt, L. M. Barton, E. J. Duval, S. Mukhopadhyay, E. Stroberg, A. Borczuk, L. B. Thorne, M. K. Sakthivel, Y. Z. Lee, J. S. Hagood, J. R. Mock, M. A. Seibold, W. K. O'Neal, S. A. Montgomery, R. C. Boucher, R. S. Baric, SARS-CoV-2 infection produces chronic pulmonary epithelial and immune cell dysfunction with fibrosis in mice. *Sci Transl Med* **14**, eabo5070 (2022).

73. W. Huber, V. J. Carey, R. Gentleman, S. Anders, M. Carlson, B. S. Carvalho, H. C. Bravo, S. Davis, L. Gatto, T. Girke, R. Gottardo, F. Hahne, K. D. Hansen, R. A. Irizarry, M. Lawrence, M. I. Love, J. MacDonald, V. Obenchain, A. K. Oles, H. Pages, A. Reyes, P.

Shannon, G. K. Smyth, D. Tenenbaum, L. Waldron, M. Morgan, Orchestrating high-throughput genomic analysis with Bioconductor. *Nat Methods* **12**, 115–21 (2015).

74. C. Radermecker, C. Sabatel, C. Vanwinge, C. Ruscitti, P. Maréchal, F. Perin, J. Schyns, N. Rocks, M. Toussaint, D. Cataldo, S. L. Johnston, F. Bureau, T. Marichal, Locally instructed CXCR4hi neutrophils trigger environment-driven allergic asthma through the release of neutrophil extracellular traps. *Nat Immunol* **20**, 1444–1455 (2019).

75. C. L. Scott, F. Zheng, P. De Baetselier, L. Martens, Y. Saeys, S. De Prijck, S. Lippens, C. Abels, S. Schoonooghe, G. Raes, N. Devoogdt, B. N. Lambrecht, A. Beschin, M. Guilliams, Bone marrow-derived monocytes give rise to self-renewing and fully differentiated Kupffer cells. *Nat Commun* **7**, 10321 (2016).

76. T. Stuart, A. Butler, P. Hoffman, C. Hafemeister, E. Papalexi, W. M. Mauck, Y. Hao, M. Stoeckius, P. Smibert, R. Satija, Comprehensive Integration of Single-Cell Data. *Cell* **177**, 1888-1902.e21 (2019).

77. S. Jung, J. Aliberti, P. Graemmel, M. J. Sunshine, G. W. Kreutzberg, A. Sher, D. R. Littman, Analysis of fractalkine receptor CX(3)CR1 function by targeted deletion and green fluorescent protein reporter gene insertion. *Mol Cell Biol* **20**, 4106–14 (2000).

78. L. Boring, J. Gosling, S. W. Chensue, S. L. Kunkel, R. V. Farese, H. E. Broxmeyer, I. F. Charo, Impaired monocyte migration and reduced type 1 (Th1) cytokine responses in C-C chemokine receptor 2 knockout mice. *J Clin Invest* **100**, 2552–2561 (1997).

79. L. Madisen, T. A. Zwingman, S. M. Sunkin, S. W. Oh, H. A. Zariwala, H. Gu, L. L. Ng, R. D. Palmiter, M. J. Hawrylycz, A. R. Jones, E. S. Lein, H. Zeng, A robust and high-throughput Cre reporting and characterization system for the whole mouse brain. *Nat Neurosci* **13**, 133–140 (2010).

80. H. Wende, S. G. Lechner, C. Cheret, S. Bourane, M. E. Kolanczyk, A. Pattyn, K. Reuter, F. L. Munier, P. Carroll, G. R. Lewin, C. Birchmeier, The transcription factor c-Maf controls touch receptor development and function. *Science* **335**, 1373–1376 (2012).

81. B. E. Clausen, C. Burkhardt, W. Reith, R. Renkawitz, I. Forster, Conditional gene targeting in macrophages and granulocytes using LysMcre mice. *Transgenic research* **8**, 265–77 (1999).

82. C. Schneider, S. P. Nobs, A. K. Heer, E. Hirsch, J. Penninger, O. M. Siggs, M. Kopf, Frontline Science: Coincidental null mutation of Csf2rα in a colony of PI3Kγ-/- mice causes alveolar macrophage deficiency and fatal respiratory viral infection. *J Leukoc Biol* **101**, 367–376 (2017).

83. F. Andreata, C. Blériot, P. Di Lucia, G. De Simone, V. Fumagalli, X. Ficht, C. G. Beccaria, M. Kuka, F. Ginhoux, M. Iannacone, Isolation of mouse Kupffer cells for phenotypic and functional studies. *STAR Protoc* **2**, 100831 (2021).

84. A. M. Rieger, K. L. Nelson, J. D. Konowalchuk, D. R. Barreda, Modified annexin V/propidium iodide apoptosis assay for accurate assessment of cell death. *J Vis Exp*, 2597 (2011).

85. K. Van den Berge, H. Roux de Bézieux, K. Street, W. Saelens, R. Cannoodt, Y. Saeys, S. Dudoit, L. Clement, Trajectory-based differential expression analysis for single-cell sequencing data. *Nat Commun* **11**, 1201 (2020).

86. Z. Gu, R. Eils, M. Schlesner, Complex heatmaps reveal patterns and correlations in multidimensional genomic data. *Bioinformatics* **32**, 2847–2849 (2016).

87. A. Subramanian, P. Tamayo, V. K. Mootha, S. Mukherjee, B. L. Ebert, M. A. Gillette, A. Paulovich, S. L. Pomeroy, T. R. Golub, E. S. Lander, J. P. Mesirov, Gene set enrichment analysis: a knowledge-based approach for interpreting genome-wide expression profiles. *Proc Natl Acad Sci U S A* **102**, 15545–50 (2005).

88. P. Danaher, Y. Kim, B. Nelson, M. Griswold, Z. Yang, E. Piazza, J. M. Beechem, Advances in mixed cell deconvolution enable quantification of cell types in spatial transcriptomic data. *Nat Commun* **13**, 385 (2022).

89. M. Foroutan, D. D. Bhuva, R. Lyu, K. Horan, J. Cursons, M. J. Davis, Single sample scoring of molecular phenotypes. *BMC Bioinformatics* **19**, 404 (2018).

Acknowledgments

We thank all members of the Immunophysiology laboratory (GIGA Institute, Liège, Belgium) for discussions; N. Maloujahmoum (Metastasis Research Laboratory, GIGA Institute) for expert technical assistance; S. Ormenese, R. Stefan, A. Hego, G. Lefevre and C. Vanwinge from the GIGA *In Vitro* Imaging Platform; P. Drion, G. Lambert, L., B. Remy and all staff members from the GIGA Mouse facility and Transgenics Platform; W. Coppieters, L. Karim, M. Deckers, A. Mayer, A. Lavergne and members from the GIGA Genomics Platform; R. Fares, I. Sbai and A. Lio for their excellent administrative support.

Funding: Supported by:
FRFS-Welbio Advanced Grant WELBIO-CR-2022A-10 (TM)
ERC Starting Grant ERC StG 2018 IM-ID: 801823 (TM)
Baillet Latour Biomedical Fund (TM)
Research Project of the F.R.S.-FNRS T015021F (TM)
Research Concerted Action of the Fédération Wallonie-Bruxelles (TM)

Author contributions

T.M. and C.Ra. conceived, supervised and secured funding for the project; C.Ru., C.Ra. and T.M. designed the experiments; C.Ru. did most of the experiments, compiled the data and prepared the figures. J.A. performed all the bioinformatic analyses. P.M., M.M., D.V. and C.Ra. helped with *in vivo*-related experiments. C. de m. and M-M. G. were implicated in experiments related to the histopathological analyses of myeloid-restricted *Maf* and *Mafb*-deficient mice. P.J., J.G. and F.S. were involved in human BALF collection and processing. M.D. and B.M. performed viral titrations and helped with viral RNA quantifications. M.T. performed electron microscopy experiments and analyses. F.B., C.S., A.H., F.G and B.G.D. were implicated in experiments involving BM chimeric mice. A.B. performed extracellular flux analyses. C.Ru, C.Ra and T.M. wrote the manuscript. All authors provided feedback on the original and revised manuscript.

Competing interests

Authors declare that they have no competing interests.

Data and materials availability

Ms4a3^{Cre} mice are used under the terms of a material transfer agreement (MTA) signed between Singapore Immunology Network (SIgN), A*STAR Research Entities (Singapore) and the University of Liege (Belgium). *Ly6g*^{CreERT2} mice are used under the terms of an MTA signed between Centro Nacional de Investigaciones Cardiovasculares Carlos III (CNIC, Madrid, Spain), and the University of Liege (Belgium). Mouse and human single-cell RNA-seq data have been deposited at GEO and are available under GEO accession GSE244765. All original codes have been deposited at Zenodo and are available via this link: https://zenodo.org/records/11354523. Requests for *Mab*$^{fl/fl}$ mice should be addressed to t.marichal@uliege.be and will be shared via an MTA.

Fig. 1. Ly6G$^+$ Macs culminate during the early recovery phase post-IAV infection. (**A**) Representative flow cytometry gating strategy showing live CD45$^+$CD11b$^+$Ly6G$^+$CD64$^-$ neutrophils (Neu), CD45$^+$CD11b$^+$Ly6G$^+$CD64$^+$ macrophages (Ly6G$^+$ Mac), CD45$^+$Ly6G$^-$CD11c$^+$SiglecF$^+$ alveolar macrophages (AM), CD45$^+$Ly6G$^-$SiglecF$^-$F4/80$^+$CD11b$^+$Ly6C$^+$CD64$^-$ monocytes (Ly6C$^+$ Mo), CD45$^+$Ly6G$^-$SiglecF$^-$F4/80$^+$CD11b$^+$Ly6C$^-$CD64$^-$ monocytes (Ly6C$^-$ Mo), CD45$^+$Ly6G$^-$SiglecF$^-$F4/80$^+$CD11b$^+$Ly6C$^+$CD64$^+$ inflammatory monocytes (iMo) and CD45$^+$Ly6G$^-$SiglecF$^-$F4/80$^+$CD11b$^+$Ly6C$^-$CD64$^+$ IM-like cells in lungs of C57BL/6 wild-type (WT) mice at day 10 post-IAV. (**B**) Time course of absolute numbers of Neu, AM, Ly6C$^-$ Mo, Ly6C$^+$ Mo, iMo and IM-like cells quantified by flow cytometry at days 0, 5, 10, 15 and 20 post-IAV in WT mice. (**C**) Representative contour plots of CD64 and CD11b expression within lung CD45$^+$CD11b$^+$Ly6G$^+$ cells at day 10 p.i. in mock-infected or IAV-infected WT mice. (**D**) Time course of absolute numbers of Ly6G$^+$ Macs quantified by flow cytometry, as in (B). (**E**) Percentage of Neu and Ly6G$^+$ Macs within Ly6G$^+$CD11b$^+$ cells quantified by flow cytometry in the blood and lungs of WT mice at day 10 post-IAV. (**F**) Photographs of Neu, Ly6G$^+$ Macs, IM-like cells and iMo sorted by FACS from IAV-infected WT mice at day 10 p.i.. Pictures are representative of 1 of 3 independent sorting experiments, each giving similar results. (**G**) Representative histograms of CXCR4, MHC-II, CD101, CD319 and CD177 expression in the indicated myeloid cell populations, quantified by flow cytometry at day 10 post-IAV in WT mice. (**H**) Quantification of expression of the indicated markers, as in (G). (B,D) Data show mean (centerline) ± SEM (colored area) and are pooled from 2-3 independent experiments (n=6 mice per time point); (E,H) mean + SEM and are pooled from 2 independent experiments (n=5-6 mice). (B,D,H) P values were calculated using a one-way ANOVA with Dunnett's post hoc tests. *, P<0.05; ***, P<0.001; ****, P<0.0001. FMO, fluorescence minus one; ns, not significant; p.i., post-infection. (F) Scale bars: 5 µm.

Fig. 2. Ly6G$^+$ Macs are transcriptionally distinct from other lung myeloid cells at day 10 post-IAV. (**A**) UMAP plots of scRNA-seq data depicting the transcriptional identity of FACS-sorted lung live CD45$^+$F4/80$^+$ and/or CD11b$^+$ cells from mock- or IAV-infected WT mice 10 days p.i. (pooled from 5 mice per conditions), merged with a published dataset of steady-state lung monocytes and IMs (*29*). (**B**) Frequency of each cluster within each experimental condition, as in (A). (**C**) Heatmap depicting the single cell expression of the most upregulated genes within each cluster. (**D**) Expression of the indicated genes within each cluster, as depicted by violin plots (height: expression; width: abundance of cells). (**E**) Representative histograms of intracellular Arg-1 and osteopontin expression in the indicated lung myeloid cell populations, quantified by flow cytometry at day 10 post-IAV in WT mice. (**F**) Quantification of Arg-1 and osteopontin expression, as in (E). (F) Data show mean + SEM and are pooled from 2 independent experiments (n=6 mice). P values were calculated using (D) a Wilcoxon rank sum test and compare C2 vs. all other clusters or (F) a one-way ANOVA with Dunnett's post hoc tests. *, P<0.05; **, P<0.01; ***, P<0.001; ****, P<0.0001. FMO, fluorescence minus one; p.i., post-infection.

Fig. 3. IAV-triggered Ly6G$^+$ Macs are recruited from classical monocytes and are short-lived. (**A**) UMAP plot depicting the transcriptional identity and cell trajectories (top), and pseudotime trajectory values (below) of lung Ly6C$^+$ Mo, iMo, Ly6G$^+$ Mac, dying Mac, CD206$^-$ IM and CD206$^+$ IM, as in Fig. 2A, evaluated by Slingshot trajectory analyses. (**B**) Heatmap plot depicting the differentially expressed genes along pseudotime evaluated by tradeSeq in the trajectory starting from Ly6C$^+$ Mo and ending either in IM or in Ly6G$^+$ Mac. (**C**) Representative histograms of tdTomato (left) and GFP (right) expression in the indicated myeloid cell populations, quantified by flow cytometry at day 10 post-IAV in *Ms4a3^{tdTom}* and *Cx3Cr1^{GFP}* mice, respectively. (**D**) Quantification of tdTomato$^+$ cells (left) and GFP expression (right), as in (C). (**E**) Representative tdTomato and CD45.1 contour plots and (**F**) bar graph showing % of host, donor *Ccr2$^{-/-}$* and donor *Ms4a3^{tdTom+}* chimerism in the indicated cell populations from lethally-irradiated CD45.1/CD45.2 mice reconstituted with a 1:1 mix of CD45.2 *Ccr2$^{-/-}$* and *Ms4a3^{tdTom+}* BM cells, infected with IAV 4 weeks later and evaluated at day 10 post-IAV. (**G**) Time course of absolute numbers of EdU$^+$ Ly6G$^+$ Macs and EdU$^+$ IM-like cells quantified by flow cytometry at days 7, 10, 14 and 17 post-IAV in EdU-pulsed WT mice at day 7 post-IAV. (**H**) Pie chart representation of the mean frequency of Annexin V and PI negative and/or positive fractions within lung Ly6C$^+$ Mo, iMo and Ly6G$^+$ Macs, quantified at day 10 post-IAV in WT mice. (**I**) Representative Ly6G and FSC contour plots and (**J**) bar graph showing % of Ly6G$^+$ cells within lung iMo sorted from WT mice at day 10 post-IAV and cultured 18 hours *ex vivo* with vehicle, M-CSF or GM-CSF. (**K**) Representative confocal microscopy pictures and (**L**) representative flow cytometry histograms of tdTomato expression within lung iMo sorted from *Ly6g^{tdTom}* mice at day 10 post-IAV and treated *ex vivo* with tamoxifen and GM-CSF or vehicle for 18 hours. (**M**) Bar graph showing donor *Csf2ra$^{-/-}$* chimerism relative to donor *Csf2ra$^{+/+}$* chimerism in the indicated cell populations from thorax-protected, lethally-irradiated CD45.1/CD45.2 mice reconstituted with a 1:1 mix of CD45.1 *Csf2ra$^{-/-}$* and CD45.2 *Csf2ra$^{+/+}$* BM cells, infected with IAV 4 weeks later and evaluated at day 10 post-IAV. (**N**) Representative histograms and (**O**) quantification of Arg-1$^+$ cells (%) in Ly6G$^+$ Macs from donor *Csf2ra$^{+/+}$* and *Csf2ra$^{-/-}$* BM cells, as in (M). Data show (D,F,J,M,O) mean + SEM and (D,F) are representative of 1 of 3 independent experiments (n=3-4 mice), (J) are pooled from 3 independent sorting experiments, each dot representing one biological replicate, (M,O) are pooled from 2 independent experiments (n=10 mice); (G) mean (centerline) ± SEM (colored area) and are pooled from 2 independent experiments (n=6 mice per time point). *P* values compare CD45.2 donor *Ccr2$^{-/-}$* chimerism in (F). *P* values were calculated using (D) a one-way ANOVA with Dunnett's post hoc tests, (F) a two-way ANOVA with Tukey's post hoc tests, (G,J) a one-way ANOVA with Tukey's post hoc tests, (M) a two-way ANOVA with Sidak's post hoc tests, (O) a two-tailed Student's *t* test. *, P<0.05; ***, P<0.001; ****, P<0.0001. FMO, fluorescence minus one; ns, not significant.

Fig. 4. Ly6G$^+$ Macs exhibit an atypical morphology and possess distinct metabolic, phagocytic and efferocytic capabilities. (**A**) GSEA analyses of Ly6G$^+$ Mac (C2) profile compared to other clusters using KEGG, Cellular Components and Biological Process gene sets. The Normalized Enrichment Score (NES), False Discovery Rate (FDR) and the size of the gene set are shown for each process. (**B**) Representative transmission electron microscopy pictures of Neu, Ly6G$^+$ Mac, IM-like cells and iMo FACS-sorted from lungs of WT mice at day 10 post-IAV. (**C**) Extracellular acidification rate (ECAR) of FACS-sorted Ly6G$^+$ Mac, Neu and IM-like cells, as in (B), quantified at baseline and under stress over time using a Seahorse assay. (**D**) Oxygen consumption rate (OCR) of Ly6G$^+$ Mac, Neu and IM-like cells, as in (C). (**E**) ECAR and OCR of Ly6G$^+$ Macs, Neu and IM-like cells, as in (C,D). (**F**) Representative histograms of E. coli-FITC signal in the indicated myeloid cell populations, quantified by flow cytometry at day 10 post-IAV and 3 hours after i.t. injection of E. coli-FITC particles. Non-injected mice were used as controls (grey line). (**G**) Quantification of E. coli-FITC$^+$ cells, as in (F). (**H**) Representative tdTomato and CD11b contour plots of and (**I**) bar graph showing % of tdTomato$^+$ cells in the indicated *Cx3cr1*$^{GFP+}$ donor cell populations from lethally-irradiated CD45.2 WT mice reconstituted with a 1:1 mix of CD45.2 *Cx3cr1*$^{GFP+}$ and *Ms4a3*$^{tdTom+}$ BM cells, infected with IAV 4 weeks later and evaluated at day 10 post-IAV. Data show (C,D) mean ± SEM and are representative of 1 of 3 independent experiments, each giving similar results; (G,I) mean + SEM and are pooled from 2 independent experiments (n=6 mice). P values (C,D) compare Ly6G$^+$ Macs vs. IM-like cells or Neu and were calculated using a two-way ANOVA with Bonferroni's post hoc tests; (G,I) were calculated using a one-way ANOVA with Dunnett's post hoc tests. **, P<0.01; ****, P<0.0001. (B) Scale bars: 2 μm.

Fig. 5. Ly6G$^+$ Macs populate the alveoli of perilesional regenerating areas. (**A**) Representative confocal microscopy picture of lung sections from *Cx3cr1*^{GFP} mice at day 10 post-IAV, with Ly6G$^+$ Macs identified as Ly6G$^+$*Cx3cr1*$^{GFP+}$ cells. (**B**) Representative *in situ* electron microscopy picture of Ly6G$^+$ Macs in the vicinity of AT2 and AT1 cells, identified on lung sections from WT mice at day 10 post-IAV. (**C**) Representative examples of regions of interest (ROIs) selected on lung sections from mock- or IAV-infected WT mice at day 10 post-IAV stained with anti-Ly6G and anti-CD68 antibodies. (**D**) Unsupervised Principal Component (PC) analysis of the ROIs analyzed by DSP. Percentages indicate the variability explained by each component. (**E**) Ly6G$^+$ Mac signature score within control, extralesional, perilesional and intralesional ROIs, as depicted by violin plots (height: scores; width: abundance of cells). (**F**) GSEA analysis of perilesional ROIs compared to intralesional ROIs using Cellular Components, Molecular Function and Biological Process gene sets. The Normalized Enrichment Score (NES), False Discovery Rate (FDR) and the size of the gene set are shown for each process. (**G**) Correlation of Ly6G$^+$ Mac score with primed AT2 (top) and DATP (bottom) scores of the ROIs. (**H**) Representative picture of perilesional Ly6G$^+$ Macs (i.e., Ly6G$^+$MHC-II$^+$ cells), pSPC$^+$ AT2 and podoplanin$^+$ AT1 identified by confocal microscopy on lung sections from WT mice at day 10 post-IAV. (A,B,H) Pictures are representative of one of 6 mice, each giving similar results. (E) *P* values were calculated using a one-way ANOVA with Tukey's post hoc tests. (G) The correlation analysis used was parametric Pearson correlation coefficient. **, $P<0.01$; ***, $P<0.001$. Scale bars: (A) 15, (B) 5, (C) 100, (D) 10 µm.

Fig. 6. C-Maf/MafB-dependent Ly6G$^+$ Macs promote euplastic alveolar epithelial regeneration. (**A**) Heatmap depicting predicted activities of c-Maf and MafB across lung myeloid cells post-IAV, evaluated by SCENIC analysis of the scRNA-seq data, as in Fig. 2A. (**B**) Representative histograms of intracellular c-Maf and MafB expression in the indicated lung myeloid cell populations, quantified at day 10 post-IAV. (**C**) Quantification of expression of intracellular c-Maf and MafB, as in (B). (**D**) Expression of *Maf* and *Mafb* within control, extralesional, perilesional and intralesional ROIs, as depicted by violin plots (height: normalized counts; width: abundance of cells). (**E**) Absolute numbers of the indicated lung myeloid cell populations, quantified at day 10 post-IAV in control and *Maf/Mafb*^{MyeloKO} mice. (**F**) Time course of relative lung NS1 RNA expression, assessed by RT-qPCR at days 0, 7 and 10 post-IAV in control and *Maf/Mafb*^{MyeloKO} mice. (**G**) Time course of weight, expressed as the % of the original weight at day 0 and assessed at days 0, 7, 10, 15, 20 post-IAV in control and *Maf/Mafb*^{MyeloKO} mice. (**H-I**) Representative (H) Hematoxylin & Eosin and (I) Periodic Acid Schiff (PAS, bottom) pictures of lung sections of control and *Maf/Mafb*^{MyeloKO} mice at day 20 post-IAV. Pictures are representative of 1 of 7 mice analyzed. (**J**) Percentage of PAS$^+$ cells in lung lesional areas of control and *Maf/Mafb*^{MyeloKO} mice at day 20 post-IAV. (**K**) Representative pSPC and Pdpn contour plots of CD45$^-$CD31$^-$EpCam$^+$ cells in mock- or IAV-infected mice at day 20 post-IAV. (**L**) Absolute numbers of pSPC$^+$Pdpn$^-$ AT2, pSPC$^-$Pdpn$^+$ AT1 and pSPC$^+$Pdpn$^+$ regenerating AT2 (reg AT2), quantified as in (K). (**M**) Time course of weight, expressed as the % of the original weight at day 8 and assessed at days 8, 11, 13, 15 and 20 post-IAV in control mice, in *Maf/Mafb*^{MyeloKO} mice instilled i.t. at days 8, 11, 13 and 15 post-IAV with PBS or with 3 x 10^5 Ly6G$^+$ Macs isolated from WT mice at day 10 post-IAV. (**N**) Absolute numbers of pSPC$^+$Pdpn$^-$ AT2, pSPC$^-$Pdpn$^+$ AT1 and pSPC$^+$Pdpn$^+$ regenerating AT2 (reg AT2), quantified at day 20 post-IAV, as in (M). (C,E,J,L,N) Data show mean + SEM and are pooled from 2 independent experiments (C:*n*=5 mice; E,N: *n*=6 mice/group; J: *n*=7 mice/group; L: *n*=8 mice/group). (F,G,M) Data show mean (centerline) ± SEM (colored area) and are pooled from 2-3 independent experiments (F: *n*=10 mice/group; G: *n*=7 mice/group; M: *n*=6 mice/group). *P* values were calculated using (A) a Wilcoxon rank sum test, (C) a one-way ANOVA with Dunnett's post hoc tests, (D,L) a one-way ANOVA with Tukey's post hoc tests, (E,F,G,M) a two-way ANOVA with Sidak's post hoc tests, (J) a two-tailed Student's *t* test, *, *P<0.05;* **, *P*<0.01; ***, *P*<0.001; ****, *P*<0.0001. FMO, fluorescence minus one; ns, not significant; p.i., post-infection. Scale bars: (H, top) 2 mm, (H, bottom; I) 200 µm.

Fig. 7. IL-4R-dependent Ly6G$^+$ Macs release soluble factors that improve alveolar regeneration from AT2 cells. (**A**) Type 2 signature score within control, extralesional, perilesional and intralesional ROIs, as depicted by violin plots (height: scores; width: abundance of cells). (**B**) Representative histograms of IL-4R expression in the indicated lung myeloid cell populations, quantified at day 10 post-IAV. (**C**) Quantification of IL-4R expression, as in (H). (**D**) Bar graph showing donor *Il4ra*$^{-/-}$ chimerism relative to donor *Ms4a3*$^{tdTom+}$ chimerism in the indicated cell populations from lethally-irradiated CD45.1 mice reconstituted with a 1:1 mix of CD45.2 *Il4ra*$^{-/-}$ and *Ms4a3*$^{tdTom+}$ BM cells, infected with IAV 4 weeks later and evaluated at day 10 post-IAV. (**E**) Representative histograms and (**F**) quantification of Arg-1$^+$ cells (%) in Ly6G$^+$ Macs from donor *Il4ra*$^{-/-}$ or *Ms4a3*$^{tdTom+}$ BM cells, as in (F). (**G**) Time course of weight, expressed as the % of the original weight at day 0 and assessed at days 0, 7, 10, 15, 20 post-IAV in lethally-irradiated CD45.1/CD45.2 WT mice reconstituted with CD45.2 *Il4ra*$^{-/-}$ BM cells (*Il4ra*$^{-/-}$ BM -> WT) or CD45.2 WT BM cells (WT BM -> WT) and infected with IAV 4 weeks later. (**H**) Cell confluence of AT2 cells (MLE-12) quantified 12 hours after a standardized scratch by live cell analysis when AT2 cells were co-cultured in the presence of Neu, IM-like cells, iMo or Ly6G$^+$ Macs isolated from the lungs of WT mice at day 10 post-IAV. (**I**) Representative picture of cell confluence of AT2 cells at 0 and 12 hours post-scratch when AT2 cells were cultured with IL-4/13 or with conditioned medium (CM) of unpulsed or IL-4/13-pulsed Ly6G$^+$ Macs isolated from the lungs of WT mice at day 10 post-IAV. (**J**) Bar graph of cell confluence of AT2 cells quantified 0, 12 and 18 hours after scratch, as in (K). (**K**) Heatmap showing the proteome profiling of CM of vehicle and IL-4/13-treated Ly6G$^+$ Macs isolated from the lungs of WT mice at day 10 post-IAV. (C,D,F,H,J) Data show mean + SEM and (C,D,F) are pooled from 2 independent experiments (C: n=6 mice; D,F: n= 8 mice); (H,J) are pooled from 3 independent sorting experiments. (G) Data show mean (centerline) ± SEM (colored area) and are pooled from 2 independent experiments (n=6 mice per group). P values were calculated using (C) a one-way ANOVA with Dunnett's post hoc tests, (D,G) a two-way ANOVA with Sidak's post hoc tests, (F) a two-tailed Student's t test, (H) a one-way or (J) a two-way ANOVA with Tukey's post hoc tests. *, $P<0.05$; **, $P<0.01$; ****, $P<0.0001$. FMO, fluorescence minus one; ns, not significant; p.i., post-infection.

Fig. 8. Ly6G$^+$ Macs are triggered by other insults and have a human counterpart. (**A**) Time course of weight, expressed as the % of the original weight at day 0 and assessed at days 0, 3, 7, 10, 14 and 18 post-injection in C57BL/6 WT mice instilled i.t. with bleomycin (bleo). (**B**) Time course of absolute numbers of lung Ly6G$^+$ Macs quantified at days 0, 5, 10, 14 and 18 post-bleo in WT mice. (**C**) Representative histograms of intracellular Arg-1 and CXCR4 expression in the indicated lung myeloid cell populations, quantified at day 14 post-bleo. (**D**) Quantification of intracellular Arg-1 and CXCR4 expression, as in (C). (**E**) Time course of absolute numbers of pSPC$^-$Pdpn$^+$ AT1 and pSPC$^+$Pdpn$^-$ AT2, quantified at days 0, 7, 10, 14 and 18 post-bleo. (**F**) Amount of alanine aminotransferase (ALT) in the plasma of WT mice injected i.p. with acetaminophen at days 0, 1, 2, 3 and 4 post-injection. (**G**) Time course of absolute numbers of liver Ly6G$^+$ Macs quantified at days 0, 1, 2, 3 and 4 post-acetominophen. (**H**) Representative histograms of intracellular Arg-1 and CXCR4 expression in liver neutrophils (Neu) and Ly6G$^+$ Macs, quantified at day 1 post-acetominophen. (**I**) Quantification of intracellular Arg-1 and CXCR4 expression, as in (H). (**J**) UMAP plot depicting the transcriptional identity of human BALF cells collected from 7 patients suspected of pneumonia and analyzed by scRNA-seq. Annotations of cell clusters are shown. (**K**) Representation of each patient within each cluster, shown as frequency. (**L**) UMAP feature plot, as in (J), according to the Ly6G$^+$ Mac signature score. The score level in cluster C9 is shown for each patient. (**M**) Ly6G$^+$ Mac signature score of single cells within each cluster, as depicted by violin plots (height: score; width: abundance of cells). (**N**) Heatmap depicting predicted activities of MAFB and MAF across BALF cell populations, evaluated by SCENIC analysis of the scRNA-seq data shown in (**J**). (A,B,E,F,G) Data show mean (centerline) ± SEM (colored area) and are pooled from 2 independent experiments (n=5-6 mice). (D,I) Data show mean + SEM and are pooled from 2 independent experiments (n=5-7 mice). P values were calculated using (A) a two-way ANOVA, (B,D,E,F,G) a one-way ANOVA with Dunnett's post hoc tests, (I) a two-tailed Student's t test or (M,N) a Wilcoxon rank sum test. (M) P values compare C9 vs. all other clusters. *, $P<0.05$; **, $P<0.01$; ***, $P<0.001$; ****, $P<0.0001$. FMO, fluorescence minus one.

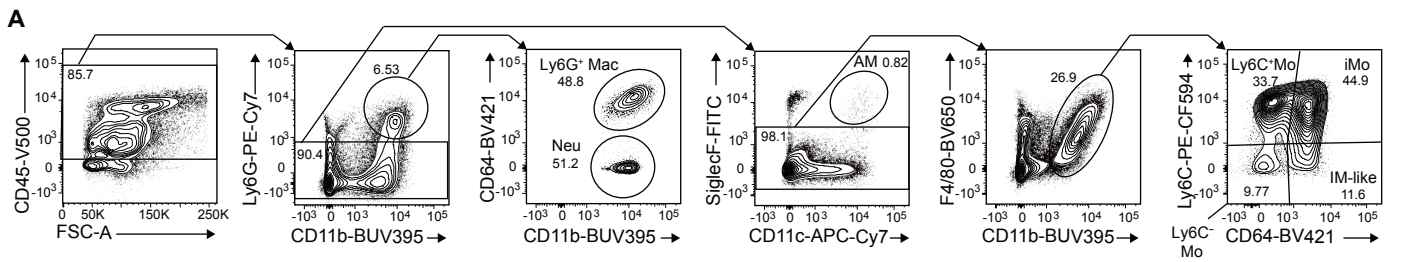
A
CD45-V500
FSC-A
85.7
Ly6G-PE-Cy7
CD11b-BUV395
6.53
90.4
CD64-BV421
Ly6G+ Mac
48.8
Neu
51.2
SiglecF-FITC
CD11c-APC-Cy7
AM 0.82
98.1
F4/80-BV650
26.9
Ly6C-PE-CF594
Ly6C+Mo
33.7
iMo
44.9
IM-like
11.6
9.77
Ly6C- Mo

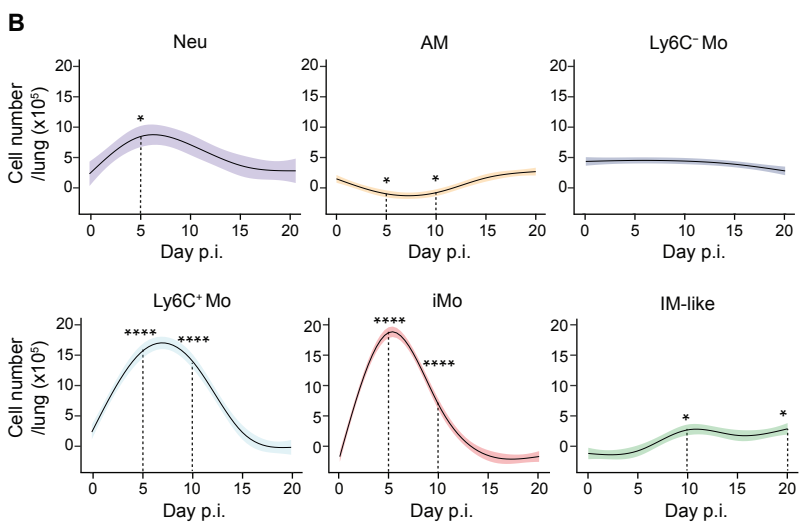
B
Neu
AM
Ly6C- Mo
Ly6C+ Mo
iMo
IM-like
Cell number /lung (x10^5)
Day p.i.

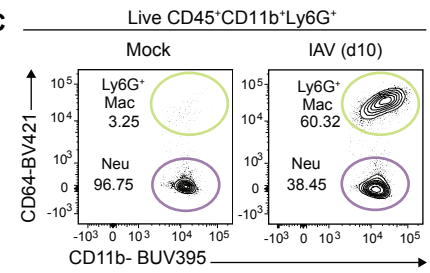
C
Live CD45+CD11b+Ly6G+
Mock
IAV (d10)
CD64-BV421
CD11b- BUV395
Ly6G+ Mac
3.25
Neu
96.75
60.32
38.45

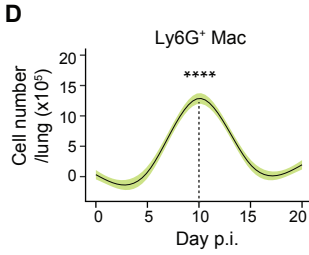
D
Ly6G+ Mac
Cell number /lung (x10^5)
Day p.i.

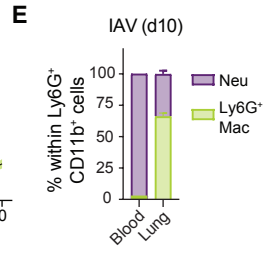
E
IAV (d10)
% within Ly6G+ CD11b+ cells
Neu
Ly6G+ Mac
Blood
Lung

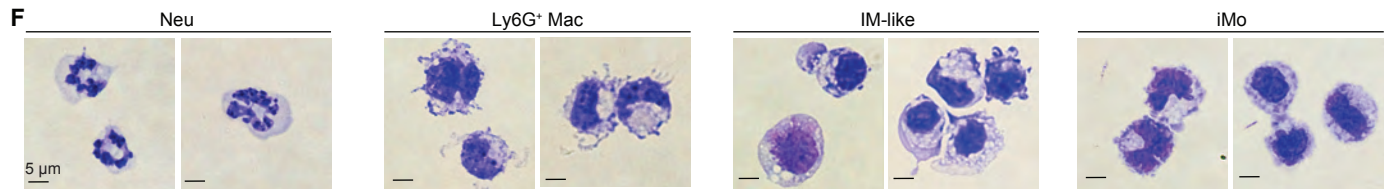
F
Neu
Ly6G+ Mac
IM-like
iMo
5 µm

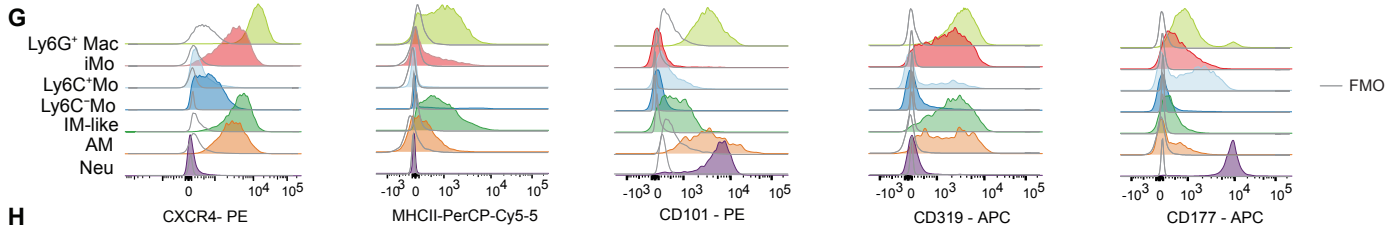
G
Ly6G+ Mac
iMo
Ly6C+Mo
Ly6C-Mo
IM-like
AM
Neu
FMO
CXCR4- PE
MHCII-PerCP-Cy5-5
CD101 - PE
CD319 - APC
CD177 - APC

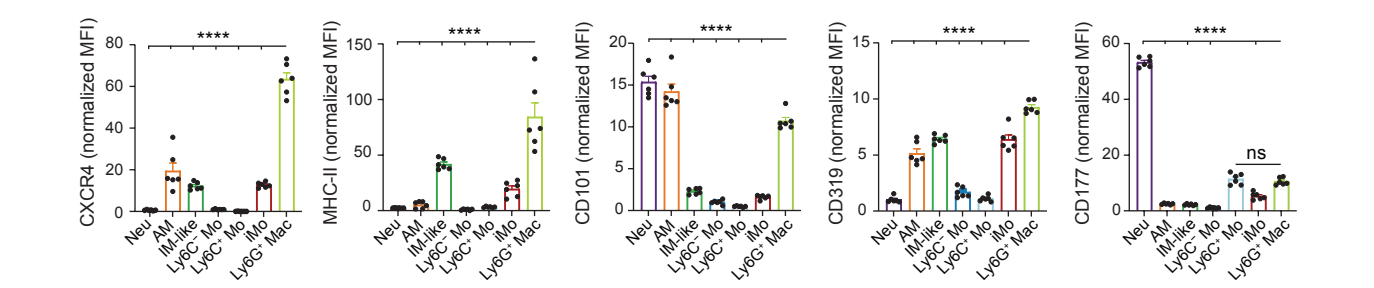
H
CXCR4 (normalized MFI)
MHC-II (normalized MFI)
CD101 (normalized MFI)
CD319 (normalized MFI)
CD177 (normalized MFI)
****
ns
Neu
AM
IM-like
Ly6C- Mo
Ly6C+ Mo
iMo
Ly6G+ Mac

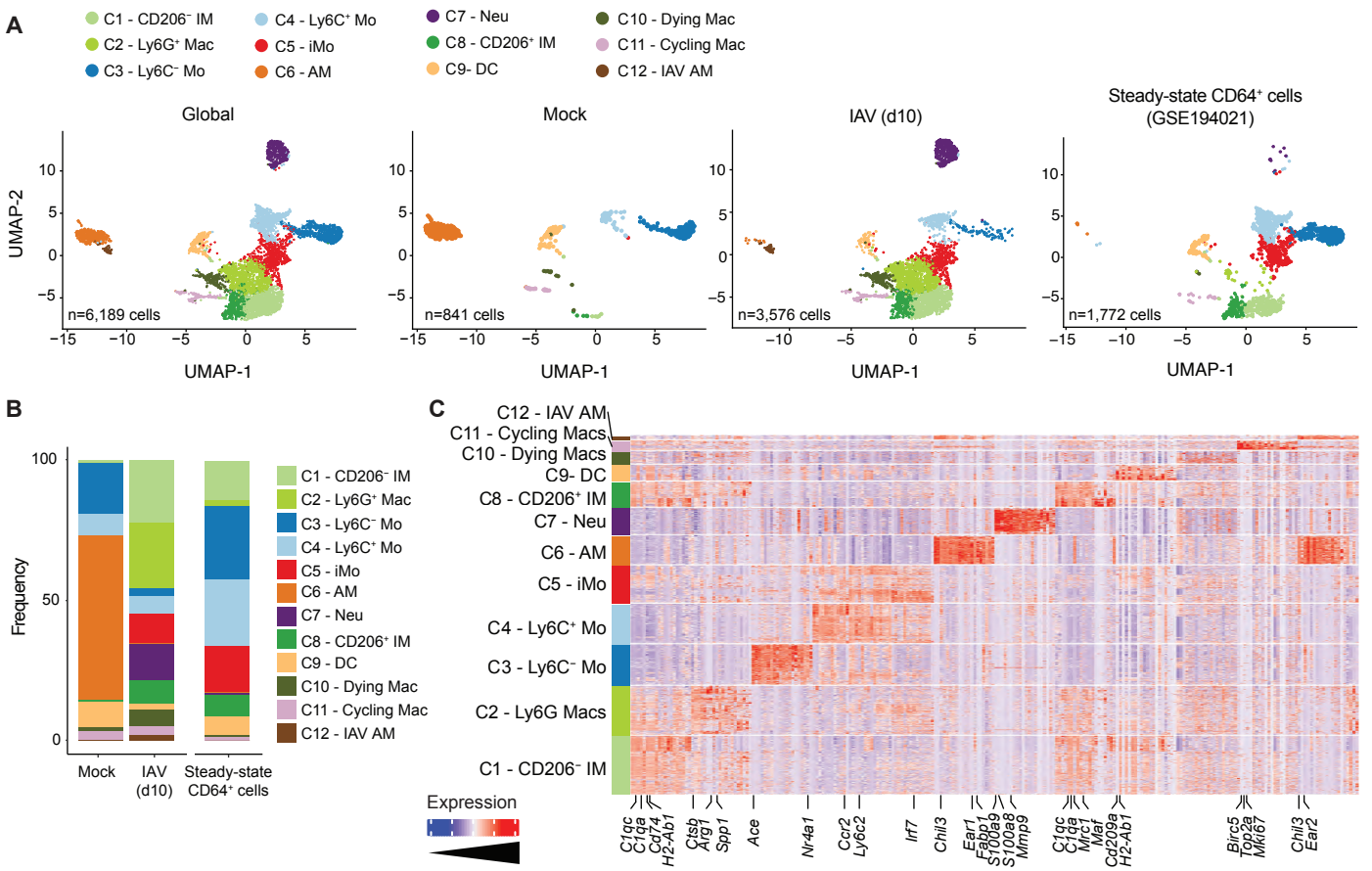
A
C1 - CD206⁻ IM
C2 - Ly6G⁺ Mac
C3 - Ly6C⁻ Mo
C4 - Ly6C⁺ Mo
C5 - iMo
C6 - AM
C7 - Neu
C8 - CD206⁺ IM
C9- DC
C10 - Dying Mac
C11 - Cycling Mac
C12 - IAV AM
Global
Mock
IAV (d10)
Steady-state CD64⁺ cells (GSE194021)
UMAP-2
UMAP-1
n=6,189 cells
n=841 cells
n=3,576 cells
n=1,772 cells

B
Frequency
Mock
IAV (d10)
Steady-state CD64⁺ cells

C
Expression
C1qc
C1qa
Cd74
H2-Ab1
Ctsb
Arg1
Spp1
Ace
Nr4a1
Ccr2
Ly6c2
Irf7
Chil3
Ear1
Fabp1
S100a9
S100a8
Mmp9
C1qc
C1qa
Mrc1
Maf
Cd209a
H2-Ab1
Birc5
Top2a
Mki67
Chil3
Ear2

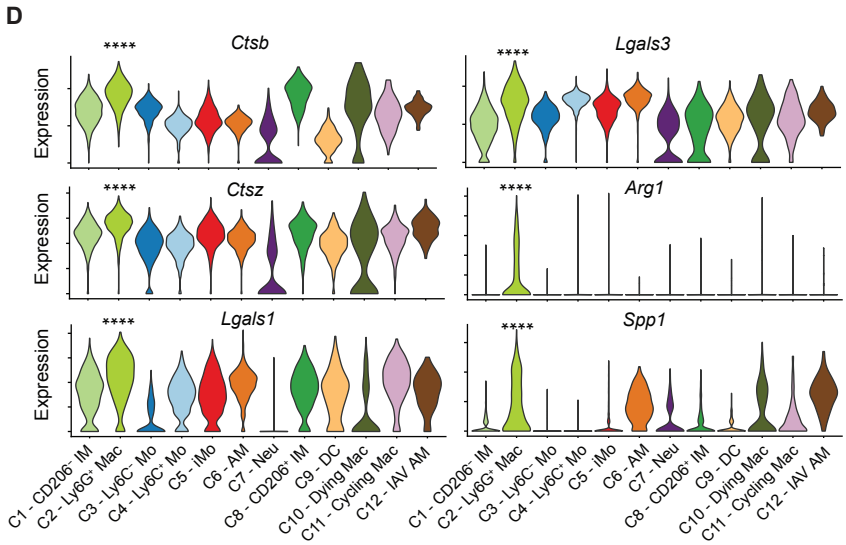
D
Ctsb
Lgals3
Ctsz
Arg1
Lgals1
Spp1
Expression
****

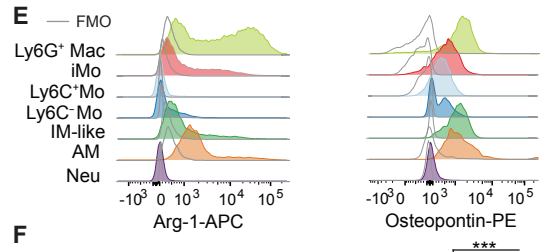
E
FMO
Ly6G⁺ Mac
iMo
Ly6C⁺Mo
Ly6C⁻Mo
IM-like
AM
Neu
Arg-1-APC
Osteopontin-PE

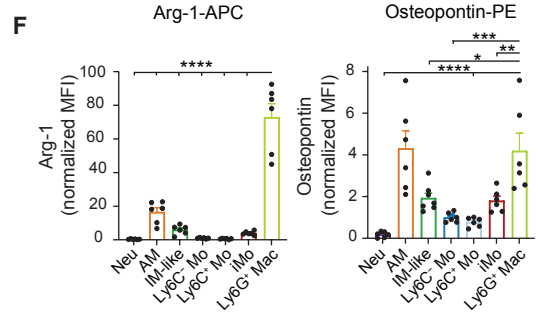
F
Arg-1 (normalized MFI)
Osteopontin (normalized MFI)
Neu
AM
IM-like
Ly6C⁻ Mo
Ly6C⁺ Mo
iMo
Ly6G⁺ Mac

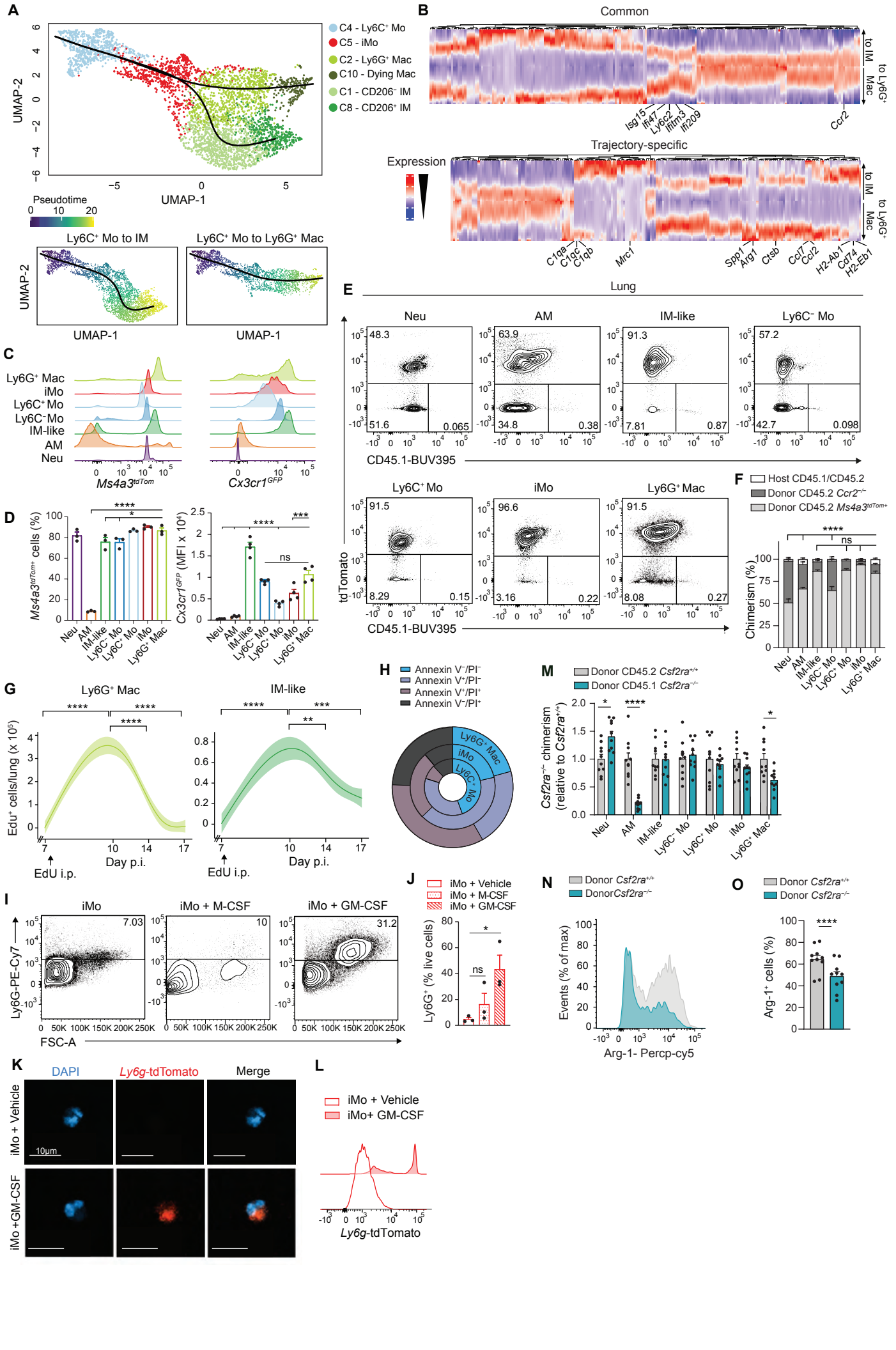
A
C4 - Ly6C+ Mo
C5 - iMo
C2 - Ly6G+ Mac
C10 - Dying Mac
C1 - CD206- IM
C8 - CD206+ IM
UMAP-2
UMAP-1
Pseudotime
Ly6C+ Mo to IM
Ly6C+ Mo to Ly6G+ Mac
B
Common
to IM
to Ly6G+ Mac
Isg15
Ifi47
Ly6c2
Ifitm3
Ifi209
Ccr2
Trajectory-specific
Expression
C1qa
C1qc
C1qb
Mrc1
Spp1
Arg1
Ctsb
Ccl7
Ccl2
H2-Ab1
Cd74
H2-Eb1
C
Ly6G+ Mac
iMo
Ly6C+ Mo
Ly6C- Mo
IM-like
AM
Neu
Ms4a3tdTom
Cx3cr1GFP
D
Ms4a3tdTom+ cells (%)
Cx3cr1GFP (MFI x 10⁴)
E
Lung
Neu
AM
IM-like
Ly6C- Mo
Ly6C+ Mo
iMo
Ly6G+ Mac
CD45.1-BUV395
tdTomato
F
Host CD45.1/CD45.2
Donor CD45.2 Ccr2-/-
Donor CD45.2 Ms4a3tdTom+
Chimerism (%)
G
Ly6G+ Mac
IM-like
Edu+ cells/lung (x 10⁵)
Day p.i.
EdU i.p.
H
Annexin V-/PI-
Annexin V+/PI-
Annexin V+/PI+
Annexin V-/PI+
I
iMo
iMo + M-CSF
iMo + GM-CSF
Ly6G-PE-Cy7
FSC-A
J
iMo + Vehicle
iMo + M-CSF
iMo + GM-CSF
Ly6G+ (% live cells)
K
DAPI
Ly6g-tdTomato
Merge
iMo + Vehicle
iMo +GM-CSF
10µm
L
iMo + Vehicle
iMo+ GM-CSF
Ly6g-tdTomato
M
Donor CD45.2 Csf2ra+/+
Donor CD45.1 Csf2ra-/-
Csf2ra-/- chimerism (relative to Csf2ra+/+)
N
Donor Csf2ra+/+
Donor Csf2ra-/-
Events (% of max)
Arg-1- Percp-cy5
O
Donor Csf2ra+/+
Donor Csf2ra-/-
Arg-1+ cells (%)

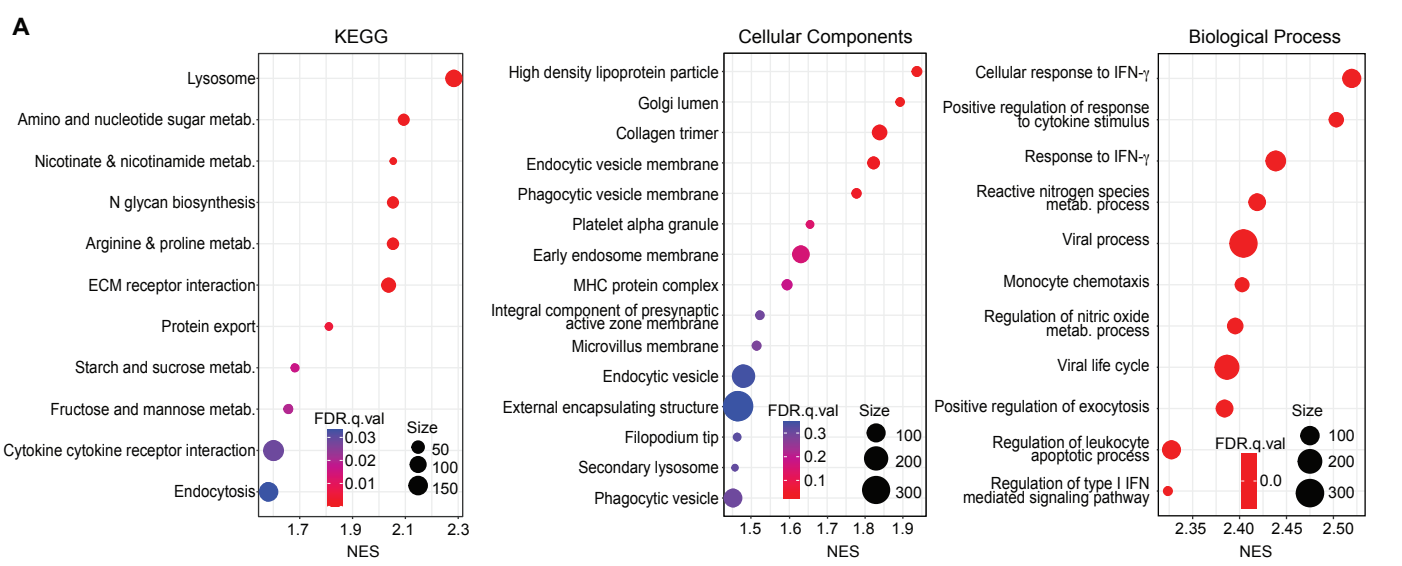
A
KEGG
Lysosome
Amino and nucleotide sugar metab.
Nicotinate & nicotinamide metab.
N glycan biosynthesis
Arginine & proline metab.
ECM receptor interaction
Protein export
Starch and sucrose metab.
Fructose and mannose metab.
Cytokine cytokine receptor interaction
Endocytosis
FDR.q.val
0.03
0.02
0.01
Size
50
100
150
1.7
1.9
2.1
2.3
NES
Cellular Components
High density lipoprotein particle
Golgi lumen
Collagen trimer
Endocytic vesicle membrane
Phagocytic vesicle membrane
Platelet alpha granule
Early endosome membrane
MHC protein complex
Integral component of presynaptic active zone membrane
Microvillus membrane
Endocytic vesicle
External encapsulating structure
Filopodium tip
Secondary lysosome
Phagocytic vesicle
FDR.q.val
0.3
0.2
0.1
Size
100
200
300
1.5
1.6
1.7
1.8
1.9
NES
Biological Process
Cellular response to IFN-γ
Positive regulation of response to cytokine stimulus
Response to IFN-γ
Reactive nitrogen species metab. process
Viral process
Monocyte chemotaxis
Regulation of nitric oxide metab. process
Viral life cycle
Positive regulation of exocytosis
Regulation of leukocyte apoptotic process
Regulation of type I IFN mediated signaling pathway
FDR.q.val
0.0
Size
100
200
300
2.35
2.40
2.45
2.50
NES

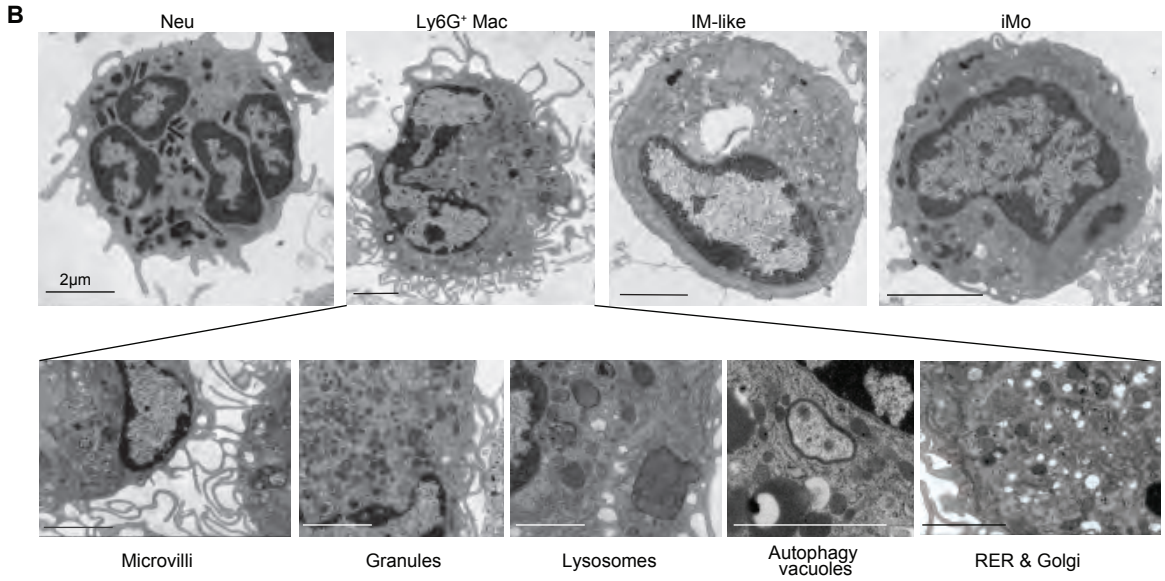
B
Neu
Ly6G⁺ Mac
IM-like
iMo
2μm
Microvilli
Granules
Lysosomes
Autophagy vacuoles
RER & Golgi

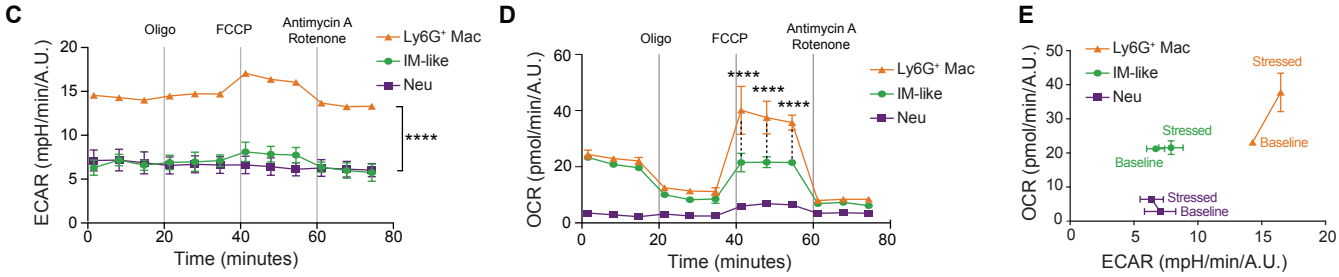
C
Oligo
FCCP
Antimycin A
Rotenone
Ly6G⁺ Mac
IM-like
Neu
****
ECAR (mpH/min/A.U.)
Time (minutes)
D
Oligo
FCCP
Antimycin A
Rotenone
****
****
****
Ly6G⁺ Mac
IM-like
Neu
OCR (pmol/min/A.U.)
Time (minutes)
E
Ly6G⁺ Mac
IM-like
Neu
Stressed
Baseline
Stressed
Baseline
Stressed
Baseline
OCR (pmol/min/A.U.)
ECAR (mpH/min/A.U.)

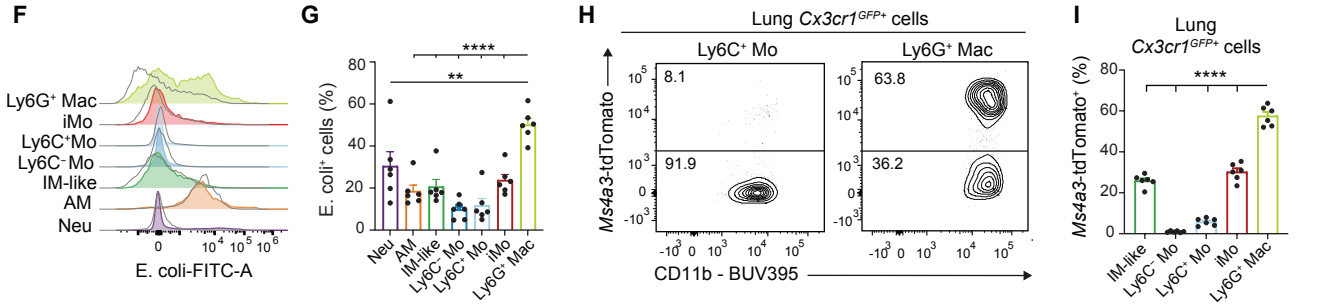
F
Ly6G⁺ Mac
iMo
Ly6C⁺Mo
Ly6C⁻ Mo
IM-like
AM
Neu
E. coli-FITC-A
G
****
**
E. coli⁺ cells (%)
Neu
AM
IM-like
Ly6C⁻ Mo
Ly6C⁺ Mo
iMo
Ly6G⁺ Mac
H
Lung Cx3cr1GFP+ cells
Ly6C⁺ Mo
Ly6G⁺ Mac
8.1
91.9
63.8
36.2
Ms4a3-tdTomato
CD11b - BUV395
I
Lung
Cx3cr1GFP+ cells
****
Ms4a3-tdTomato⁺ (%)
IM-like
Ly6C⁻ Mo
Ly6C⁺ Mo
iMo
Ly6G⁺ Mac

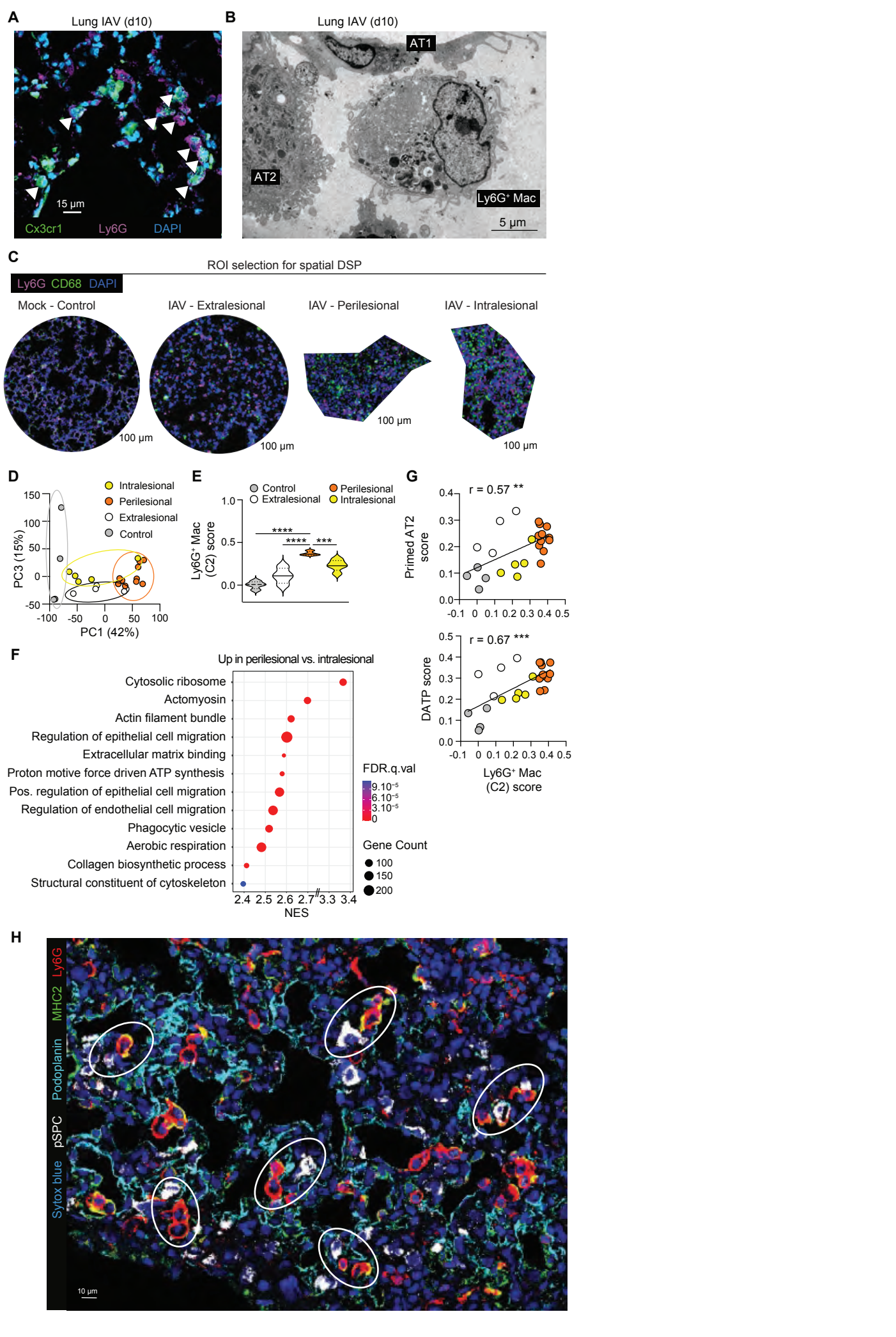
A
Lung IAV (d10)
15 µm
Cx3cr1
Ly6G
DAPI
B
Lung IAV (d10)
AT1
AT2
Ly6G⁺ Mac
5 µm
C
ROI selection for spatial DSP
Ly6G CD68 DAPI
Mock - Control
IAV - Extralesional
IAV - Perilesional
IAV - Intralesional
100 µm
D
Intralesional
Perilesional
Extralesional
Control
PC3 (15%)
PC1 (42%)
E
Control
Extralesional
Perilesional
Intralesional
Ly6G⁺ Mac (C2) score
****
****
***
G
r = 0.57 **
Primed AT2 score
r = 0.67 ***
DATP score
Ly6G⁺ Mac (C2) score
F
Up in perilesional vs. intralesional
Cytosolic ribosome
Actomyosin
Actin filament bundle
Regulation of epithelial cell migration
Extracellular matrix binding
Proton motive force driven ATP synthesis
Pos. regulation of epithelial cell migration
Regulation of endothelial cell migration
Phagocytic vesicle
Aerobic respiration
Collagen biosynthetic process
Structural constituent of cytoskeleton
NES
FDR.q.val
Gene Count
H
Ly6G
MHC2
Podoplanin
pSPC
Sytox blue
10 µm

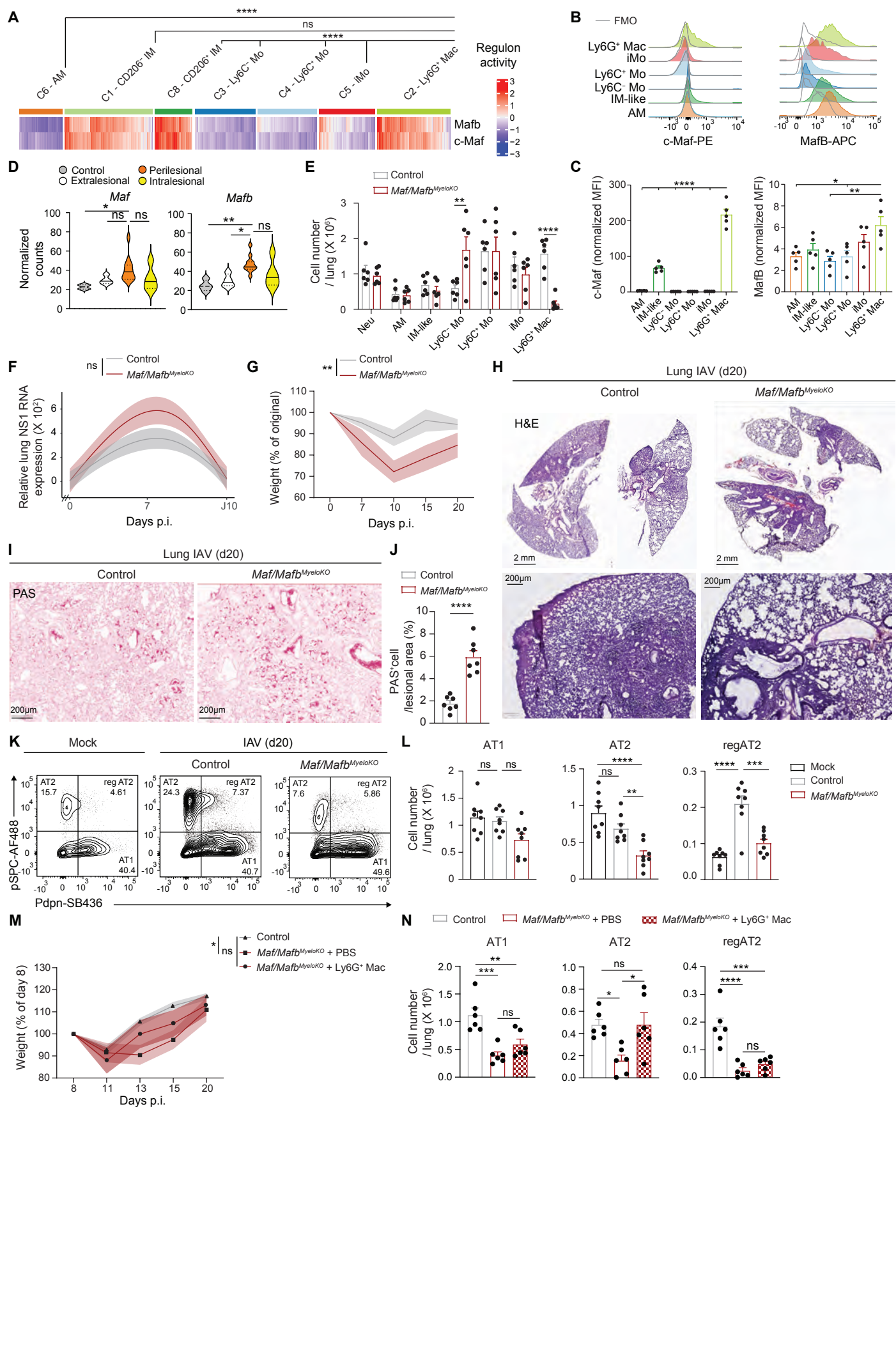
A
C6 - AM
C1 - CD206- IM
C8 - CD206+ IM
C3 - Ly6C- Mo
C4 - Ly6C+ Mo
C5 - iMo
C2 - Ly6G+ Mac
Regulon activity
Mafb
c-Maf
B
FMO
Ly6G+ Mac
iMo
Ly6C+ Mo
Ly6C- Mo
IM-like
AM
c-Maf-PE
MafB-APC
C
c-Maf (normalized MFI)
MafB (normalized MFI)
D
Control
Extralesional
Perilesional
Intralesional
Maf
Mafb
Normalized counts
E
Control
Maf/MafbMyeloKO
Cell number / lung (X 10^6)
Neu
AM
IM-like
Ly6C- Mo
Ly6C+ Mo
iMo
Ly6G+ Mac
F
Relative lung NS1 RNA expression (X 10^2)
Days p.i.
G
Weight (% of original)
Days p.i.
H
Lung IAV (d20)
Control
Maf/MafbMyeloKO
H&E
2 mm
200µm
I
Lung IAV (d20)
Control
Maf/MafbMyeloKO
PAS
200µm
J
PAS+cell /lesional area (%)
K
Mock
IAV (d20)
AT2
reg AT2
AT1
pSPC-AF488
Pdpn-SB436
L
AT1
AT2
regAT2
Cell number / lung (X 10^6)
M
Weight (% of day 8)
Days p.i.
Maf/MafbMyeloKO + PBS
Maf/MafbMyeloKO + Ly6G+ Mac
N

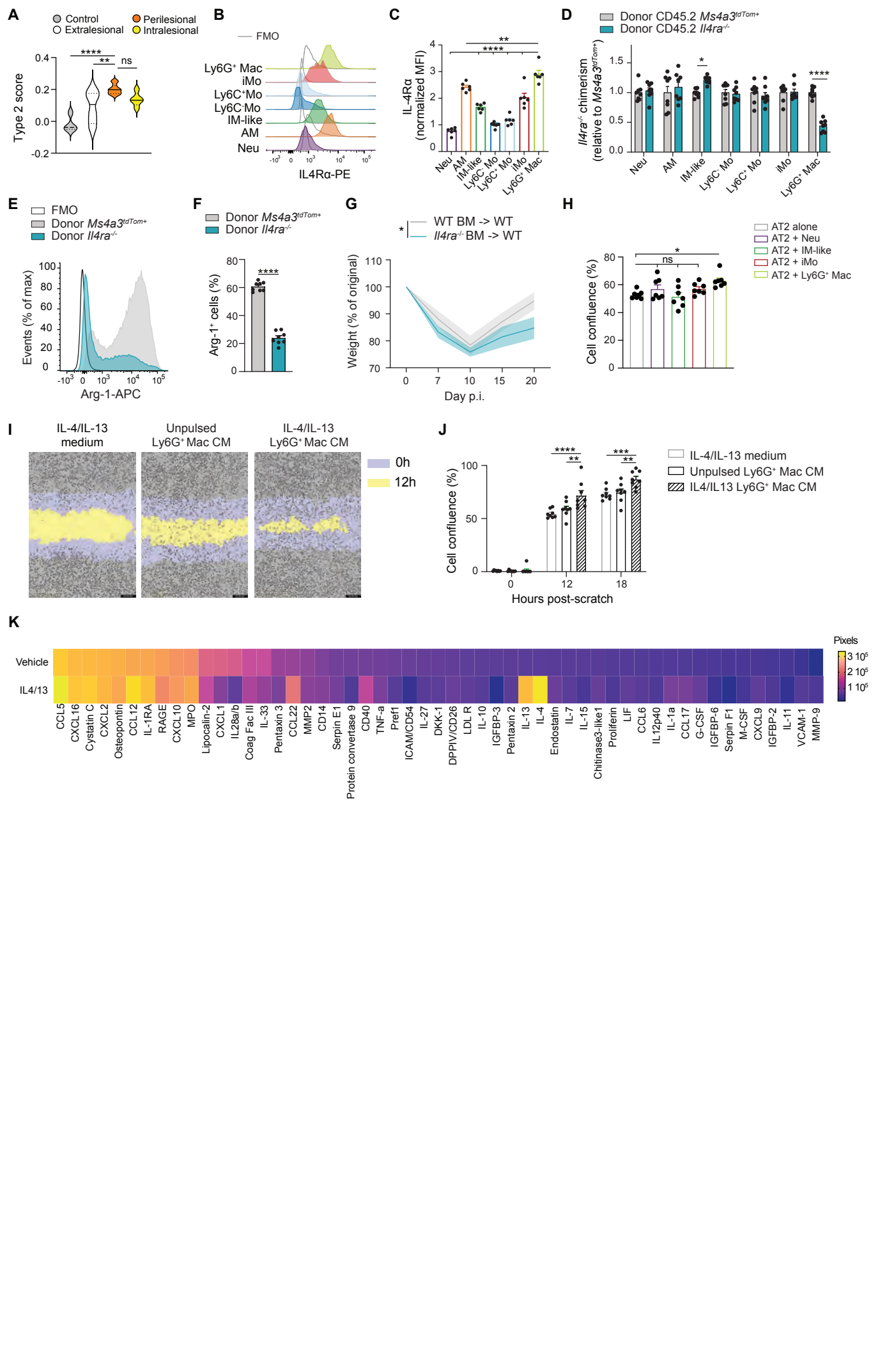
A
Control
Extralesional
Perilesional
Intralesional
Type 2 score
****
**
ns
B
FMO
Ly6G+ Mac
iMo
Ly6C+Mo
Ly6C-Mo
IM-like
AM
Neu
IL4Rα-PE
C
IL-4Rα (normalized MFI)
Neu
AM
IM-like
Ly6C- Mo
Ly6C+ Mo
iMo
Ly6G+ Mac
D
Donor CD45.2 Ms4a3tdTom+
Donor CD45.2 Il4ra-/-
Il4ra-/- chimerism (relative to Ms4a3tdTom+)
E
FMO
Donor Ms4a3tdTom+
Donor Il4ra-/-
Events (% of max)
Arg-1-APC
F
Donor Ms4a3tdTom+
Donor Il4ra-/-
Arg-1+ cells (%)
G
WT BM -> WT
Il4ra-/- BM -> WT
Weight (% of original)
Day p.i.
H
AT2 alone
AT2 + Neu
AT2 + IM-like
AT2 + iMo
AT2 + Ly6G+ Mac
Cell confluence (%)
I
IL-4/IL-13 medium
Unpulsed Ly6G+ Mac CM
IL-4/IL-13 Ly6G+ Mac CM
0h
12h
J
IL-4/IL-13 medium
Unpulsed Ly6G+ Mac CM
IL4/IL13 Ly6G+ Mac CM
Cell confluence (%)
Hours post-scratch
K
Vehicle
IL4/13
Pixels
CCL5
CXCL16
Cystatin C
CXCL2
Osteopontin
CCL12
IL-1RA
RAGE
CXCL10
MPO
Lipocalin-2
CXCL1
IL28a/b
Coag Fac III
IL-33
Pentaxin 3
CCL22
MMP2
CD14
Serpin E1
Protein convertase 9
CD40
TNF-a
Pref1
ICAM/CD54
IL-27
DKK-1
DPPIV/CD26
LDL R
IL-10
IGFBP-3
Pentaxin 2
IL-13
IL-4
Endostatin
IL-7
IL-15
Chitinase3-like1
Proliferin
LIF
CCL6
IL12p40
IL-1a
CCL17
G-CSF
IGFBP-6
Serpin F1
M-CSF
CXCL9
IGFBP-2
IL-11
VCAM-1
MMP-9

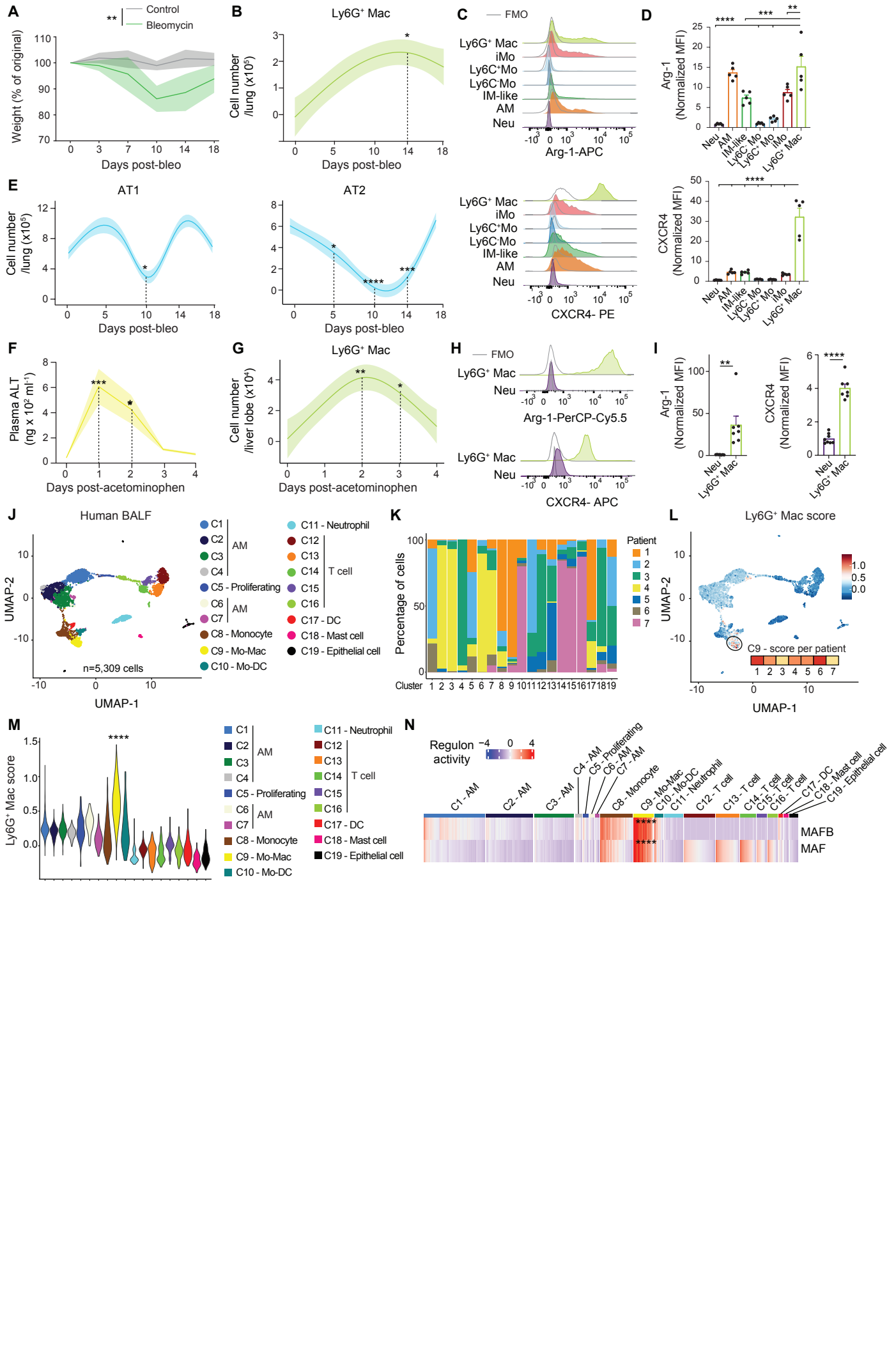
A
Control
Bleomycin
Weight (% of original)
Days post-bleo
B
Ly6G+ Mac
Cell number /lung (x10^5)
Days post-bleo
C
FMO
Ly6G+ Mac
iMo
Ly6C+Mo
Ly6C-Mo
IM-like
AM
Neu
Arg-1-APC
CXCR4- PE
D
Arg-1 (Normalized MFI)
CXCR4 (Normalized MFI)
E
AT1
AT2
Cell number /lung (x10^5)
Days post-bleo
F
Plasma ALT (ng x 10^2 ml^-1)
Days post-acetominophen
G
Ly6G+ Mac
Cell number /liver lobe (x10^4)
Days post-acetominophen
H
FMO
Ly6G+ Mac
Neu
Arg-1-PerCP-Cy5.5
CXCR4- APC
I
Arg-1 (Normalized MFI)
CXCR4 (Normalized MFI)
J
Human BALF
n=5,309 cells
UMAP-1
UMAP-2
C1
C2
C3
C4
AM
C5 - Proliferating
C6
C7
AM
C8 - Monocyte
C9 - Mo-Mac
C10 - Mo-DC
C11 - Neutrophil
C12
C13
C14
C15
C16
T cell
C17 - DC
C18 - Mast cell
C19 - Epithelial cell
K
Percentage of cells
Cluster
Patient
L
Ly6G+ Mac score
C9 - score per patient
M
Ly6G+ Mac score
N
Regulon activity
MAFB
MAF

Supplementary Materials for

Recruited atypical Ly6G$^+$ macrophages license alveolar regeneration after lung injury

C. Ruscitti[1,2], J. Abinet[1,2], P. Maréchal[1,2], M. Meunier[1,2], C. de meeûs[2,3], D. Vanneste[1,2], P. Janssen[1,2], M. Dourcy[2,4], M. Thiry[5], F. Bureau[2,6], C. Schneider[7], B. Machiels[2,4], A. Hidalgo[8,9], F. Ginhoux[10,11,12,13], B.G. Dewals[2,4], J. Guiot[14,15], F. Schleich[14,15], M-M. Garigliany[2,3], A. Bellahcène[16], C. Radermecker[1,2,*], T. Marichal[1,2,17,*]

Corresponding authors: c.radermecker@uliege.be; t.marichal@uliege.be

The PDF file includes:

Materials and Methods

Mice

All experiments, unless otherwise specified, were performed on age-matched 8–12-wk-old male and female mice on the C57BL/6 background. The following strains of mice were used: CD45.2 wild-type (WT) C57BL/6J (The Jackson Laboratory, #000664); CD45.1 WT (The Jackson Laboratory, #002014); *Cx3cr1*$^{GFP/+}$ (*77*) (The Jackson Laboratory, #005582); *Ccr2*$^{-/-}$ (*78*) (The Jackson Laboratory, #004999); *Ms4a3*^{Cre} (*31*); *Ly6g*^{CreERT2} (*37*); *R26*$^{LSL\text{tdTomato}}$ (*79*) (The Jackson Laboratory, #007909); *Maf*$^{fl/fl}$ (*80*), *Mafb*$^{fl/fl}$ (*39*); *Lyz2*^{Cre} (*81*) (The Jackson Laboratory, #004781); *Il4ra*$^{-/-}$; CD45.1 *Csf2ra*$^{-/-}$ (*82*). *Il4ra*$^{-/-}$ mice were kindly provided by Bernhard Ryffel (CNRS Orléans, France). CD45.1/CD45.2 WT C57BL/6J mice were obtained from CD45.1 WT crossed with CD45.2 WT mice. Myeloid-restriced c-Maf and Mafb depletion was achieved by crossing *Maf*$^{fl/fl}$ and *Mafb*$^{fl/fl}$ mice with Lyz2^{Cre} mice. *Ms4a3*^{tdTom} and *Ly6g*^{tdTom} mice were obtained by crossing *R26*$^{LSL\text{tdTomato}}$ with *Ms4a3*^{Cre} and *Ly6g*^{CreERT2} mice, respectively.

Mice were housed under specific pathogen-free conditions and maintained in a 12-h light–dark cycle with food and water ad libitum. All animal experiments described in this study were carried out in an animal biosafety level 3 containment unit. Experiments were reviewed and approved by the Institutional Animal Care and Use Committee of the University of Liège (ethical approval #2276). The 'Guide for the Care and Use of Laboratory Animals,' prepared by the Institute of Laboratory Animal Resources, National Research Council, and published by the National Academy Press, as well as European and local legislations, was followed carefully. Accordingly, the temperature and relative humidity were 21°C and 45-60%, respectively

In vivo models of injury

The mouse-adapted influenza strain A/Puerto Rico/8/34 (H1N1; PR8) was kindly provided by F. Trottein (Institut Pasteur, France). The viral stock suspension (10^8 Plaque Forming Units [PFU] ml^{-1}) was diluted and 5 PFU were administered intranasally (i.n.) to isoflurane-anesthetized mice in 50 µl of PBS (Thermo Fisher). Control groups received an equal volume of PBS i.n. for mock infection.

For bleomycin-induced lung injury, isoflurane-anesthetized mice were treated intratracheally (i.t.) with a single instillation of 0.06 IU of bleomycin (Bio-Connect) in a volume of 50µl PBS. Control animals received 50µl PBS alone.

For acetaminophen-induced liver injury, mice were fasted during 15 hours with free access to water and were injected intraperitoneally (i.p.) with 300mg kg^{-1} of acetaminophen (Sigma) in saline solution (NaCl 0.9%). Free access to food was allowed after treatment.

Assessment of viral NS1 mRNA levels

Whole lungs were excised and total mRNA was isolated from homogenized tissues according to the Immgen protocol (www.immgen.org). cDNA was obtained with RevertAid First Strand cDNA Synthesis Kit (Thermo Fisher), and qPCR was performed in duplicate with iTaq Universal SYBR green supermix (BioRad). Primer sequences were as follows: 5′-TTCACCATTGCCTTCTCTTC-3′ and 5′-CCCATTCTCATTACTGCTTC-3′ for viral NS1, 5′-CATGGCTCGCTCGGTGACC-3′ and 5′-AATGTGAGGCGGGTGGAACTG-3′ for housekeeping gene B2m. Expression levels of NS1 were normalized relative B2M control gene.

Reagents and antibodies

A complete list of the reagents and antibodies used in this manuscript can be found in Tables S2 and S3, respectively.

Bone marrow, blood and tissue cell isolation

Cell isolation was achieved as previously described (*39*, *74*). Briefly, for BM cells, femurs were dissected and cleaned of soft adhering tissue. Distal and proximal ends were opened, and BM cells were flushed out. After centrifugation, cell pellets were re-suspended in ice-cold PBS containing 10 mM EDTA and cell suspensions were filtered using a cell strainer (70 µM, Corning) to obtain a single cell suspension. Blood was collected from the tail vein in a 100 mM EDTA (Merck Millipore)-containing tube, and red blood cells were lysed with RBC lysis buffer (ThermoFischer). For the isolation of lung leucocytes and structural cells, lung vessels were perfused with 5 ml PBS through the right ventricle and 1 ml HBSS (Lonza) containing 0.5 UI dispase II (Sigma-Aldrich), 0.1mg ml^{-1} elastase (MedChemExpress), 0.075 mg ml^{-1} DNAse (Roche) was injected i.t. before dissecting the lung and digesting it for 30 minutes at 37°C in the same digestion medium. After 30 minutes of digestion, lungs were cut into small pieces with razor blades and further digested for 30 minutes at 37°C in HBSS containing 5% vol/vol FBS (Thermo Fisher), 0.5 UI dispase II, 0.05 mg ml^{-1} DNAse, 1 mg ml^{-1} collagenase A (Roche). After 30 minutes, the cell suspension was flushed using a 18-gauge needle to dissociate aggregates. Ice-cold PBS containing 10 mM EDTA was added to stop the digestion process and cell suspensions were filtered using a 70 µm cell strainer. Residual red blood cells were lysed with RBC lysis buffer. Leucocytes isolation from the liver was obtained as previously described (*83*). Briefly, after sacrifice, mice were perfused with 10 ml PBS through right ventricle, the liver middle lobe was dissected and the gallbladder removed. The liver was cut into small pieces with razor blades and digested for 45 minutes at 37°C in 10 ml HBSS containing 0.2mg ml^{-1} collagenase IV (ThermoFisher), 5U ml^{-1} DNase I and 10% vol/vol FBS (Thermo Fischer). After incubation, the homogenized liver suspension was filtered using a 70 µm cell strainer, washed with 10 ml ice-cold PBS containing 10mM EDTA and centrifuged at 50 rcf for 3 minutes. The aqueous phase was recovered, filtered in a new tube and centrifuged at 400 rfc for 5 minutes. The cell pellet was suspended in RBC lysis buffer for 2 minutes, then washed with 10 ml ice-cold PBS containing 10mM EDTA. In all experiments, the number of cells was counted using an automatic cell counter (iPrasense Norma XS).

Flow cytometry

Staining reactions were performed in the dark at 4°C for 30 minutes with 2% v/v of Fc block (BD Biosciences) to avoid nonspecific binding. For intracellular stainings, extracellular-stained cells were fixed and permeabilized with the Foxp3/Transcription factor Staining Buffer Set (Thermo Fisher). For EdU stainings, extracellular-stained cells were permeabilized and stained using Click-iT EdU Alexa Fluor 488 Flow Cytometry Assay Kit (Thermo Fisher), according to the manufacturer's instructions.

Cell viability was assessed using 7-AAD (BD Bioscience) or Fixable Viability Dye eFluor™ 780 (Thermo Fisher). Cell suspensions was analysed with a FACSCANTO II or a LSRFortessa (BD Biosciences). Results were analyzed using FlowJo software (Tree Star). For scRNA-seq, transmission electron microscopy, cytological examination and *ex vivo* experiments, lung myeloid cells were sorted using a FACSAria III (BD Biosciences) or a Sony MA900.

Cytologic examination

Cytologic examination of FACS-sorted neutrophils, iMo, IM-like cells, iMo and Ly6G$^+$ Macs at 10 days post-IAV was performed on cytospin preparations stained with Hemacolor (Merck KgaA). Sections were examined with an Echo Revolve microscope.

Annexin V/Propidium iodide assay

Annexin V/Propidium iodide (PI) apoptosis assay was performed as described (*84*). Briefly, after lung cell isolation, cells were resuspended in Annexin V binding buffer (ThermoFisher) and 2.10^6 cells were stained with Annexin V-APC and incubated in the dark for 15 minutes at room temperature. Cells were washed with 100 µl of Annexin V binding buffer and 2 µg ml^{-1} PI (ThermoFisher) were added to each sample and incubated in the dark for 15 minutes at room temperature. After washing with 500µl of Annexin V buffer, cells were centrifuged, cell pellet was resuspended in fixative solution of 1% vol/vol formaldehyde in PBS and incubated for 10 minutes on ice. Cells were washed with PBS, centrifuged, resuspended in PBS supplemented with 50 µg ml^{-1} RNase A (Merck Millipore) and incubated for 15 minutes at 37°C. Cell suspension was washed with PBS, centrifuged and resuspended for flow cytometry stainings.

***In vivo* treatments**

For EdU incorporation experiments shown in fig. S3, B and C, mice were injected i.p. at day 10 post-IAV with 1 mg EdU (Santa Cruz Biotechnology) in 200 µl PBS 4 hours before sacrifice. For experiments addressing the lifespan of Ly6G$^+$ Macs (Fig. 3G), 1mg EdU in 200 µL PBS was injected i.p. twice 5 hours apart at day 7 post-IAV, and EdU incorporation was evaluated in blood leucocytes at day 8 post-IAV. The incorporation of EdU in lung myeloid cells was evaluated at days 10, 14 and 17 post-IAV. Assessment of phagocytic activity was performed as previously described (*69*). Briefly, isoflurane-anesthetized mice were instilled i.t. with 2.10^8 pHrodo™ Green E. coli BioParticules (Thermo Fisher) in 100 µl PBS. Lungs were harvested 3 hours later for flow cytometry analyses.

Generation of BM (competitive) chimeras

CD45.2, CD45.1 or CD45.1/CD45.2 WT mice were anesthetized by i.p. injection of 200 µl PBS containing ketamine (Nimatek, Dechra, 75 mg kg^{-1}) and xylazine (Rompun, Bayer, 10 mg kg^{-1}). When mentioned, the thoracic cavity was protected with a 0.6-cm-thick lead cover. Mice were irradiated with two consecutive doses of 6 Gy 15 minutes apart. Once recovered from the anaesthesia, mice were reconstituted by intravenous (i.v.) administration of 2.10^6 BM cells from *Ms4a3*^{tdtom} or *Il4ra*$^{-/-}$ mice, for full chimeras. For mixed BM chimeras, mice were reconstituted i.v. with 2.10^6 BM cells consisting of a 1:1 mix of BM cells obtained from the following mice: CD45.1 WT, *Ms4a3*^{tdtom}, *Ccr2*$^{-/-}$, CD45.1 *Csf2ra*$^{-/-}$, CD45.2 *Csf2ra*$^{+/+}$, *Cx3cr1*$^{GFP+}$, *Il4ra*$^{-/-}$, or homozygous *Ly6g*^{CreERT2} mice *(*also called *Ly6g*$^{-/-}$ mice). From the day of irradiation, mice were treated for 4 weeks with 0.05 mg ml^{-1} of enrofloxacin (Baytril, Bayer) in drinking water. Chimerism was assessed by flow cytometry in the blood 4 weeks after irradiation.

scRNA-sequencing and analyses

Mouse scRNA-seq analyses

Lung myeloid cells were FACS-sorted as living singlet CD45$^+$, F4/80$^+$ and/or CD11b$^+$ cells from lung single-cell suspensions pooled from 5 mock-infected and IAV-infected C57BL/6 male WT

mice at day 10 post-IAV. For each sample, an aliquot of Trypan blue-treated cells was examined under the microscope for counting, viability and aggregate assessment following FACS sorting. Viability was above 90% for all samples and no aggregates were observed. Cell preparations were centrifuged and pellets were resuspended in calcium- and magnesium-free PBS containing 0.4 mg ml^{-1} UltraPure BSA (Thermo Fisher Scientific).

The 10X Genomics platform (Single Cell 3' Solution) was used. For library preparation, approximately 2,000 (Mock group) and 6,000 (IAV group) cells were loaded into the Chromium Controller, in which they were partitioned, their polyA RNAs captured and barcoded using Chromium Single Cell 3' GEM, Library & Gel Bead Kit v3 (10X Genomics). The cDNAs were amplified and libraries compatible with Illumina sequencers were generated using Chromium Single Cell 3' GEM, Library & Gel Bead Kit v3 (10X Genomics). The libraries were sequenced on an Illumina NovaSeq sequencer on an SP100 cell flow (Read1: 28 cy, read2: 76 cy, index1: 10cy, index2: 10cy) at a depth of 50,000 reads per cell.

The Cell Ranger (v6.1.2) application (10x Genomics) was used to demultiplex the BCL files into FASTQ files (cellranger mkfastq), to perform alignment (to Cell Ranger mouse genome references 6.1.2 GRCm38/release 102), filtering and unique molecular identifier counting and to produce gene-barcode matrices.

Filtered matrix files were used for further scRNA-seq analyses with R Bioconductor (3.17) and Seurat (4.3.0) (31178118). Briefly, filtered matrices containing cell IDs and feature names in each sample were used to build a Seurat object. We performed quality control by filtering out the cells with less than 200 detected genes, the genes detected in less than three cells and the cells exhibiting more than 10% of mitochondrial genes. Gene counts in each sample were normalized separately by default method 'LogNormalize' with a scale factor of 10,000 and log transformation. Two thousand highly variable features were identified with the 'vst' method. After merging cells from all samples, cell contaminants were removed based on the expression of cell-specific genes, and 12 clusters were identified in the remaining cells using the FindClusters function (15 Principal Components [PC] included and a resolution of 0.7 was selected) and the differentially expressed genes (DEGs) were calculated using the FindAllMarkers function (Seurat package). ScRNA_seq datasets containing steady-state $CD64^+$ lung cells (GSE194021) were integrated with the lung myeloid cells of this study using FindIntegrationAnchors function (Seurat) with anchor.features = 2000.

Single-cell regulatory network inference and clustering analysis

To predict the potential active transcription factors, lung myeloid cells analyzed by scRNA-seq were subjected to SCENIC analysis (*36*). The normalized counts, nFeature_RNA and nCount_RNA in the merged Seurat object were used for the initial SCENIC analysis. The genes expressed with a value of 3 in 0.1% of the cells and detected in 1% of the cells were kept, and coexpression network analysis was made with GENIE3 in the SCENIC package. To represent the SCENIC results, the results of the '3.4_regulonAUC' output were added to the metadata of Seurat object so that regulon AUC scores could be plotted as a heatmap.

Slingshot and tradeSeq pseudotime trajectory analyses

To evaluate trajectory-based differential expression analysis, $CD206^-$ IMs, $Ly6G^+$ Macs, $Ly6C^+$ Mos, iMos, $CD206^+$ IMs and dying Macs were subjected to Slingshot analysis (*32*). The trajectories along pseudotime were built using umap embedding from the Seurat object. To

compare the expression patterns of DEGs across pseudotime, the counts matrix, pseudotime and cell weights calculated above were then used as input in fitGAM function (tradeSeq package) (*85*). The association of average expression of each gene with pseudotime was tested using associationTest and the DEGs between IMs and Ly6G$^+$ Mac trajectories were calculated with the patternTest function. The value of the estimated smoother on a grid of pseudotimes was estimated for each DEG using predictSmooth. The 200 DEGs with the biggest FcMedian and waldStat > 200 were annotated as 'changed genes', meaning that their expression patterns were different in IMs and Ly6G$^+$ Mac trajectories, while the 200 genes whose average expression was associated with pseudotime in both lineages were selected based on their Fold change and labeled as 'unchanged genes'. Genes whose expression patterns appeared to be influenced by a small number of cells behaving as outliers were manually removed. Finally, the scaled estimated smoothers calculated by predictSmooth were used to build heat maps with the ComplexHeatmap package (*86*).

Gene Set Enrichment Analyses (GSEA)

In order to analyse enrichment of published signatures in the scRNA-seq data, the normalized counts were used as expression datasets in GSEA. GSEA was carried out using the GSEA software (version 4.1.0) (*87*). We used the hallmark gene sets from the Molecular Signatures Database (MSigDB) to test for enrichment. The analyses involved a gene set permutation method with 1,000 permutations to calculate the enrichment scores.

scRNA-seq of human BALF cells

Chromium Fixed RNA Profiling for multiplexed samples (10X Genomics) was used for scRNA-seq analysis of human BALF cells, allowing the storage of fixed cells and enabling analysis of multiple samples in one single GEM reaction. Fresh samples were directly fixed in a 4% formaldehyde solution after collection for storage at -80°C. For GEM creation, the Multiplex-compatible Chromium Next GEM Single Cell Fixed RNA Human Transcriptome Probe Kit including a Probe Barcode that permits sample multiplexing and subsequent demultiplexing was used. The Cell Ranger (v7.1.0) application (10x Genomics) was used to demultiplex the BCL files into FASTQ files (cellranger mkfastq), to perform alignment (to Cell Ranger human genome reference GRCh38-2020-A), filtering and unique molecular identifier counting and to produce gene-barcode matrices. Filtered matrix files were used for further scRNA-seq analyses. Samples from two different multiplexed batches were integrated with FindIntegrationAnchorsfunction (using canonical correlation analysis). A total of 19 clusters were identified, with 16 PCs were included and a resolution of 0.9.

Orthologous genes of the Ly6G$^+$ Mac signature in humans were manually identified using the gene database of NCBI. The signature was then used to calculate the score for each cell using AddModuleScore function (Seurat). The scores were stored in the seurat object and plotted using FeaturePlot function.

Single-cell regulatory network inference and clustering analysis was performed on scRNA-seq data from human BALF cells, as explained above.

Transmission electron microscopy

FACS-sorted myeloid cell populations or lung tissues from IAV-infected mice at day 10 post-IAV were fixed in 2.5% glutaraldehyde (diluted in Sorensen's buffer: 0.1 M Na2HPO4/NaH2PO4 buffer, pH 7.4) for 1h at 4 °C and postfixed for 30 min in 2% OsO4 (diluted in 0.1 M Sorensen's

Buffer). After dehydration in graded ethanol, samples were embedded in Epon resin. Ultrathin sections obtained with a Reichert Ultracut S ultramicrotome (Reichert Technologies) were contrasted with 2% uranyl acetate and 4% lead citrate.

For ultrastructural analyses, random fields of cells were examined under a Jeol TEM JEM-1400 Transmission Electron Microscope at 80 kV, and photographed using an 11-megapixel camera system (Quemesa, Olympus).

Extracellular flux analysis

Oxygen consumption rate (OCR) was measured using Seahorse XF Cell Mito Stress Test (Agilent) according to manufacturer's recommendations and as described previously (*70*, *71*). Briefly, Neu, IM-like cells and Ly6G$^+$ Macs were FACS-sorted at day 10 post-IAV and seeded (10.10^4, 7.10^4 and 8.10^4 cells/well, respectively) in XFp mini-plates (Agilent) pre-coated with CellTak. Cells were kept in unbuffered serum-free DMEM supplemented with pyruvate (1mM), glutamine (2mM), glucose (10mM), at pH 7.4, 37 °C and ambient CO_2 for 1h before the assay. Analysis was performed using the XFp analyser (Seahorse Bioscience) as per manufacturer's instructions. Cells were sequentially challenged with 1 µM oligomycin, 1 µM carbonyl cyanide p-(trifluoromethoxy) phenylhydrazone (FCCP), and rotenone/antimycin mix (0.5 µM each). All results were normalized according to the cell number evaluated by Hoechst (2 mg ml^{-1}) incorporation after cold methanol/acetone fixation.

Spatial transcriptomic analyses using Digital Spatial Profiling (DSP)

Five-µm-thick formalin-fixed, paraffin-embedded (FFPE) sections were prepared using the protocol from NanoString Technologies. Briefly, 2 tissue slides, each containing 1 mock and 2 IAV samples harvested 10 days post-IAV, were analyzed. Slides were first stained with antibodies against CD68, Ly6G (clone 1A8), and DNA was visualized with 500 nM Syto83. Mouse Whole Transcriptome Atlas probes targeting more than 19,000 targets were hybridized, and slides were loaded on the GeoMx DSP. Briefly, entire slides were imaged at x20 magnification, and Regions of Interest (ROIs) were chosen based on serial Hematoxylin & Eosin sections and on morphological markers to select lesional, perilesional and extralesional areas. ROIs were exposed to ultraviolet light, releasing the indexing oligos and collecting them in a 96-well plate for subsequent processing and sequencing, as described (*72*). Raw count, third quartile (Q3)–normalized count data of target genes from ROIs were provided by the vendor, which were used as input to downstream analyses. Pairwise differential expression analysis between perilesional, lesional, extralesional and control ROIs were performed using the GeoMx Digital Spatial Profiler Data Analysis Suite (DSPDA version 3.0.0.111). The R script SpatialDecon (*88*) was loaded into the DSPDA and run using the Mouse Adult Lung profile matrix. For cell signature scoring, the gene signatures were obtained from scRNA-seq data using the 20 most specific markers obtained using the FindAllMarkers function (Seurat package), genes were then ordered according to their average log_2FC. Lung myeloid cell signature scores were obtained from our own scRNA-seq datasets, while the AT2, primed AT2, DATPs and AT1 signature score were calculated from previously published data (*38*) using the same procedure. The geneset from the activation pathway of IL4 (BIOCARTA_IL4_PATHWAY) was download from MSigDB and was used to generate the type 2 signature score shown in Fig. 7A. The signatures were then used to calculate the score for each ROI using the simpleScore function (singscore package) (*89*) on the ranked gene expression matrix.

Immunofluorescence

Immunofluorescence stainings of mouse lungs were performed as previously described (*39*). Briefly, lungs from WT or *Cx3cr1*$^{GFP+}$ mice were perfused with 5 ml PBS through the right ventricle then with 5 ml paraformaldehyde (PFA) 4% (Thermo Fisher) in PBS, and lungs were collected. Lungs were fixed for 4 h in 4% PAF at 4 °C, then cryoprotected overnight in 30% sucrose (VWR) in PBS at 4 °C, followed by embedding in optimal cutting temperature compound (OCT) (VWR) and stored at −80 °C.

For staining of lungs from *Cx3cr1*$^{GFP+}$ mice (Fig. 5A), 7-µm-thick sections were cut and left in a methanol 100% (Merck) bath at −20 °C for 20 minutes prior to be stained for 2h at room temperature with a rabbit anti-GFP antibody (ThermoFischer) and a rat anti-mouse Ly6G (BDBioscience). After washing samples with PBS, a secondary anti-rat AF594 (Invitrogen) was added in blocking buffer and incubated for 2 hours in the dark at room temperature.

For stainings of WT lungs (Fig. 5H and fig. S8), 7-µm-thick sections were cut and left in a methanol 100% (Merck) bath at −20 °C for 20 minutes prior to be stained overnight at 4°C in blocking buffer (PBS with 0.3% Triton X-100 [Merck], 2% donkey serum [Merck]) with the following antibodies: rabbit anti-mouse pSPC (Abcam); rat anti-mouse Ly6G (BDBioscience). After washing samples with PBS, secondary antibodies (anti-rabbit AF532; anti-rat AF594 [Invitrogen]) were added in blocking buffer and incubated for 2 hours in the dark at room temperature. Samples were washed with PBS and incubated with directly-coupled antibodies (eFluor570-Ki67 [Invitrogen]; anti-mouse AF700-MHC-II [ThermoFischer]; anti-mouse Superbright432-Pdpn [ThermoFischer]) in blocking buffer for 6 hours at 4 °C.

Finally, all samples were washed one last time with PBS and were mounted with 10 µl ProLong Antifade reagent (Invitrogen) containing 0.1% Sytox blue nucleic acid stain (Invitrogen) on glass slides and stored at room temperature in the dark overnight.

Images shown in Fig. 3K and 5A were acquired on an LSM 980 inverted confocal microscope using Plan-Apochromat 20x/0.8 or LD C-Apochromat 40x/1.1 W objectives. Fluorophores were excited simultaneously at 405/561 nm (Fig. 3K) or 405/488/561 nm (Fig. 5A) with detection wavelength at 300-735/499-594/573-627 with GaAsP-PMT in Zeiss FastAiryScanSheppardSum SR-4y:3.7 mode and bidirectional acquisition. Analysis was performed with Zeiss Blue software.

Images shown in Fig. 5H and fig. S8 were acquired on a Leica Stellaris 8 Inverted Confocal microsocope with a White Light Laser (WLL) using 20x APO CS2 or 40x 1.30 NA Oil objectives and 512x512, 400 Hz, unidirectional acquisition. The acquisition was finalized by 3 sequential settings, all with WLL at 85% and a pinhole at 1 AU (65,3). We used, for the first sequence, the combination of diode laser 405 (dsetector HyD S 415-443 nm) and WLL with a laser line of 556 nm (Detector HyD S 570-620nm); for the second sequence, the WWL with a laser line of 528 nm (Detector HyD S 541-564 nm) and 445 nm (Detector HyD S 450-515nm); for the third sequence, the WLL with a laser line of 499nm (Detector HyD S 504-539 nm) and 696nm (Detector HyD X 706-752 nm). The images were then analyzed with LAS X software version 4.7.0.28176.

Histology

Seven-µm-thick sections from frozen lung tissues obtained from mock- and IAV-infected mice at day 20 post-IAV were mounted onto glass slides and stained with Hematoxylin & Eosin (H&E) or periodic-acid Schiff (PAS). The slides were scanned with an Axioscan 7 scanner (Zeiss,

Germany). Whole slide images were analysed with an open-source automated software analysis program for digital pathology (QuPath version 0.4.3). Briefly, lesional areas were determined manually and automated tissue detection was performed in the lesional area to correct for alveolar blank spaces. Thereafter, built-in algorithms for pixel classification of QuPath and machine learning were used on PAS sections and a threshold was determined to quantify % of mucus$^+$ cells within the lesional area.

Ex vivo experiments

For *ex vivo* stimulation and co-culture experiments, single cell suspensions isolated from IAV-infected lungs of WT or *Ly6g*^{tdTom} mice at day 10 post-IAV were enriched in CD11b$^+$ cells by a magnetic-activated cell sorting (MACS) using CD11b MicroBeads (Myltenyi). Cells were then stained and FACS-sorted using the gating strategy shown in Fig. 1A. After sorting, cells were counted, spinned down, and either directly added to the co-culture with MLE-12 cells, or seeded in 96 wells at a concentration 5.10^4 cells/well in complete RPMI (ThermoFischer), containing 1mM sodium pyruvate, 1% vol/vol MEM non-essential amino acids, 50 U ml^{-1} Penicillin-Streptomycin and 10% vol/vol FBS. For stimulation experiments, recombinant mouse GM-CSF (20 ng ml^{-1}, Peprotech), mouse M-CSF (20 ng ml^{-1}, Peprotech), mouse IL-4 (20 ng ml^{-1}, Peprotech) or mouse IL-13 (20 ng ml^{-1}, Peprotech) were added. When required, Cre-ERT2 activation was achieved by adding 0.02 mg ml^{-1} of 4-hydroxytamoxifen (Sigma-Aldrich). After 18 hours of culture, cell supernatants were collected (conditioned medium, CM) and cells were harvested for flow cytometry phenotyping. For the visualisation of tdTomato induction in tamoxifen-treated iMos from *Ly6g*^{tdTom} mice by confocal microscopy, iMos were seeded and cultured in 8-chambers slides (Nunc Lab-Tek II Chamber Slide system, Sigma) precoated with poly-D-lysin hydrobromide (Sigma). Cells were incubated in complete RPMI containing 0.02 mg ml^{-1} 4-hydroxytamoxifen and 20ng ml^{-1} GM-CSF or vehicle. Supernatants were removed and chambers were rinsed with PBS. Slides were then fixed with paraformaldehyde 10% for 10 minutes, rinsed twice with PBS and mounted with ProLong Antifade reagent with DAPI (ThermoFisher). Images were acquired as above.

Proteome profiler (R&D) was performed on CM from Ly6G$^+$Macs cultured for 18h in complete RPMI with or without 20ng ml^{-1} IL-4 and 20ng ml^{-1} IL-13 treatment. The assay was performed following the manufacturer's instructions and was analysed using the Protein Array Analyzer plug-in for ImageJ.

Murine lung epithelial (MLE)-12 cells (ATCC, CVCL_3751) were cultured in DMEM/F12 (ThermoFisher) complemented with 1% Insulin-Transferrin-Selenium (ITS-G) (ThermoFisher), L-glutamine 2mM (ThermoFisher), FBS 2% and HEPES 10mM (ThermoFisher). Cells were incubated at 37 °C in a humidified atmosphere containing 5% CO2. Cells were passaged at 80–90% confluence using 0.05% Trypsin-EDTA (ThermoFisher). Experiments were performed with passage numbers ranging from 4 to 6. Scratch Wound Assay were performed using IncucyteS3 (Sartorius). MLE-12 cells were seeded in 96-well (Sartorius) at density of 4.10^4 cells/well and incubated 24 hours in DMEM/F12 medium. An open wound area was created in the cell monolayer using the IncuCyte ® Wound Maker tool, washed with PBS and subsequently co-cultured with 5.10^4 Neu, IM-like cells, iMos or Ly6G$^+$ Macs, or incubated with CM from unpulsed or IL-4/IL-13-pulsed Ly6G$^+$ Macs. Complete DMEM medium containing 20 ng ml^{-1} IL-4 and 20 ng ml^{-1} IL-13 was used as control. Cells were imaged after wounding every 3 hours at 10 x magnification using the Sartorius Incucyte S3 Inverted brighfield microscope with motorized XYZ in a chamber

for 37°C temperature, 5% CO2 and 90-95% humidity. Images were acquired by Basler Ace 1920-155um, acA1920-155umEBS camera with 10 x 0.3 NA, Dry, 16mm WD objective. For each time point, relative wound closure was calculated using the Scratch Wound analyses pipeline of the IncuCyte 2023A Rev1 software.

Adoptive transfer of Ly6G$^+$ Macs *in vivo*

Ly6G$^+$ Macs were isolated from the lungs of CD45.2 WT mice at day 10 poist-IAV. Lung single cell suspensions were first enriched in CD11b$^+$ cells by MACS using CD11b MicroBeads (Miltenyi Biotec) and were FACS-sorted using a Sony MA900. Four hundred thousands (4 x 10^5) Ly6G$^+$ Macs were resuspended in 50 µl sterile PBS and were instilled i.t. in lightly isoflurane-anesthetized *Maf/Mafb*^{MyeloKO} mice at days 8, 11, 13, 15 post-IAV. Control *Maf/Mafb*^{MyeloKO} mice and WT mice received 50 µl PBS as vehicle.

Quantification of alanine aminotransferase (ALT)

Blood was collected in a a 100 mM EDTA (Merck Millipore)-containing tube and centrifuged at 4000 rpm for 4 minutes. Plasma was collected and levels of ALT were determined usinf a mouse ALT ELISA Kit (Abcam) following manufacturer's instructions.

Human BALFs

The use of human BALF cells was approved in 2022 by the Ethics Reviewing Board of the University Hospital of Liege, Belgium (ref. 2022/159). The characteristics of the patients are summarized in Table S1. Human BALFs were fixed directly after collection for storage and scRNA-seq analyses.

Statistical analysis

Graphs were prepared with GraphPad Prism 9 (GraphPad software) or R Bioconductor (3.5.1) (*73*). Data distribution was assumed to be normal when parametric tests were performed. Data from independent experiments were pooled for analysis in each data panel, unless otherwise indicated. No data were excluded from the analyses. Statistical analyses were performed with Prism 9 (GraphPad software), and with R Bioconductor (3.5.1) (*73*) and Seurat (*76*) for scRNA-seq data, respectively. The statistical analyses performed for each experiment are indicated in the respective figure legends. We considered a P value lower than 0.05 to be significant (*, $P < 0.05$; **, $P < 0.01$; ***, $P < 0.001$; ****, $P < 0.0001$; ns, not significant).

Additional sections and details about Materials and Methods can be found in the Supplemental Materials.

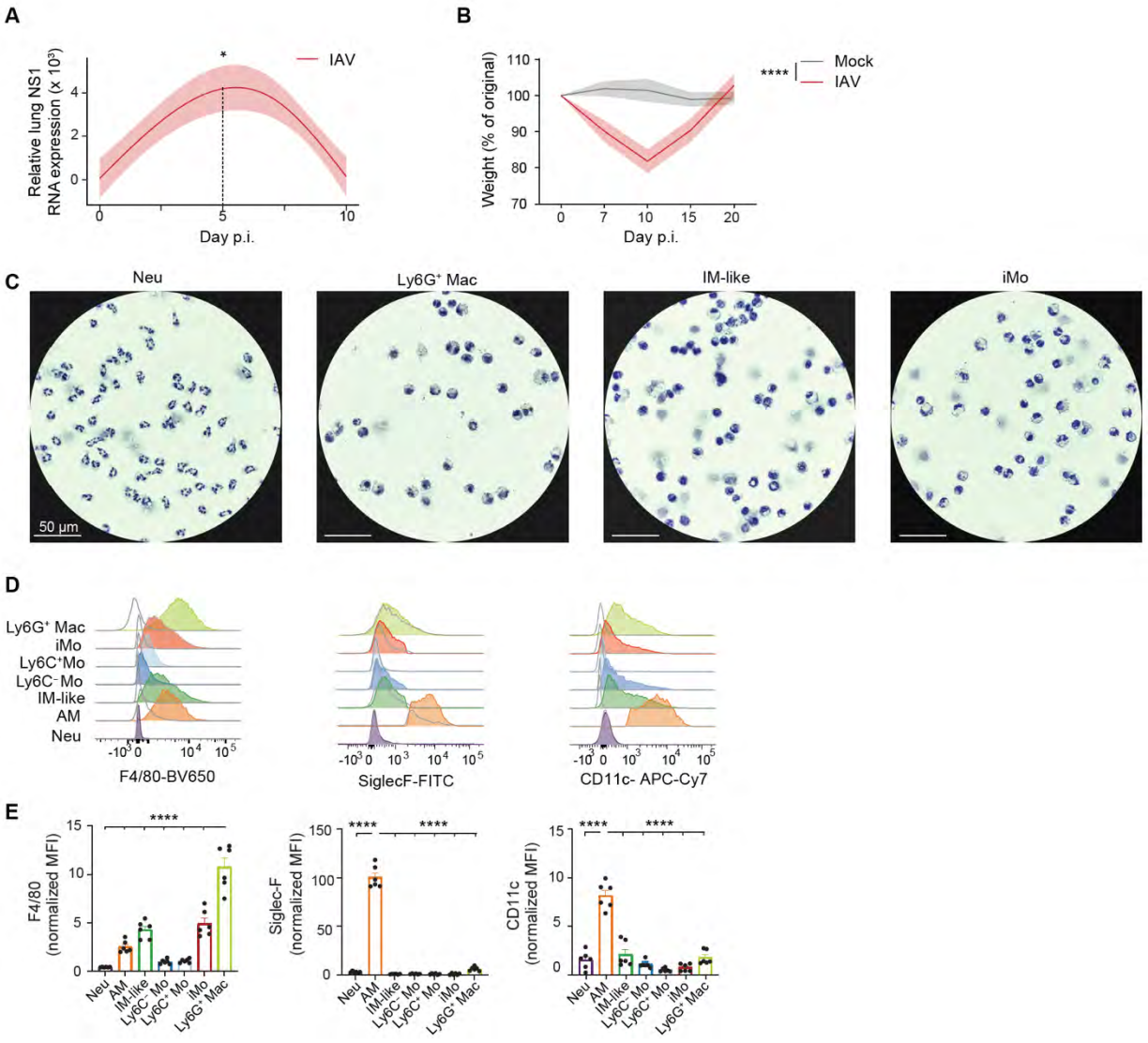

Fig. S1. Morphology and phenotype of lung myeloid cells at day 10 post-IAV. (**A**) Time course of relative lung NS1 RNA expression, assessed by RT-qPCR at days 0, 5 and 10 post-IAV in WT mice. (**B**) Time course of weight, expressed as the % of the original weight at day 0 and assessed at days 0, 7, 10, 15 and 20 post-IAV in WT mice. (**C**) Photographs of Neu, Ly6G$^+$ Macs, IM-like cells and iMo sorted by FACS from IAV-infected WT mice at day 10 p.i.. Pictures are representative of 1 of 3 independent sorting experiments, each giving similar results. (**D**) Representative histograms of F4/80, SiglecF and CD11c expression in the indicated myeloid cell populations, quantified by flow cytometry at day 10 post-IAV in WT mice. (**E**) Quantification of expression of the indicated markers, as in (D). (A,B) Data show mean (centerline) ± SEM (colored area) and are pooled from 2 independent experiments (*n*=6-7 mice per time point). (E) Data show mean + SEM and are pooled from 2 independent experiments (*n*= 6 mice). *P* values compare day 5 vs. day 0 in (A) and were calculated using (A,D) a one-way ANOVA with Dunnett's post hoc tests or (B) a two-way ANOVA. *, $P<0.05$; ****, $P<0.0001$. p.i., post-infection. (C) Scale bar: 50 µm.

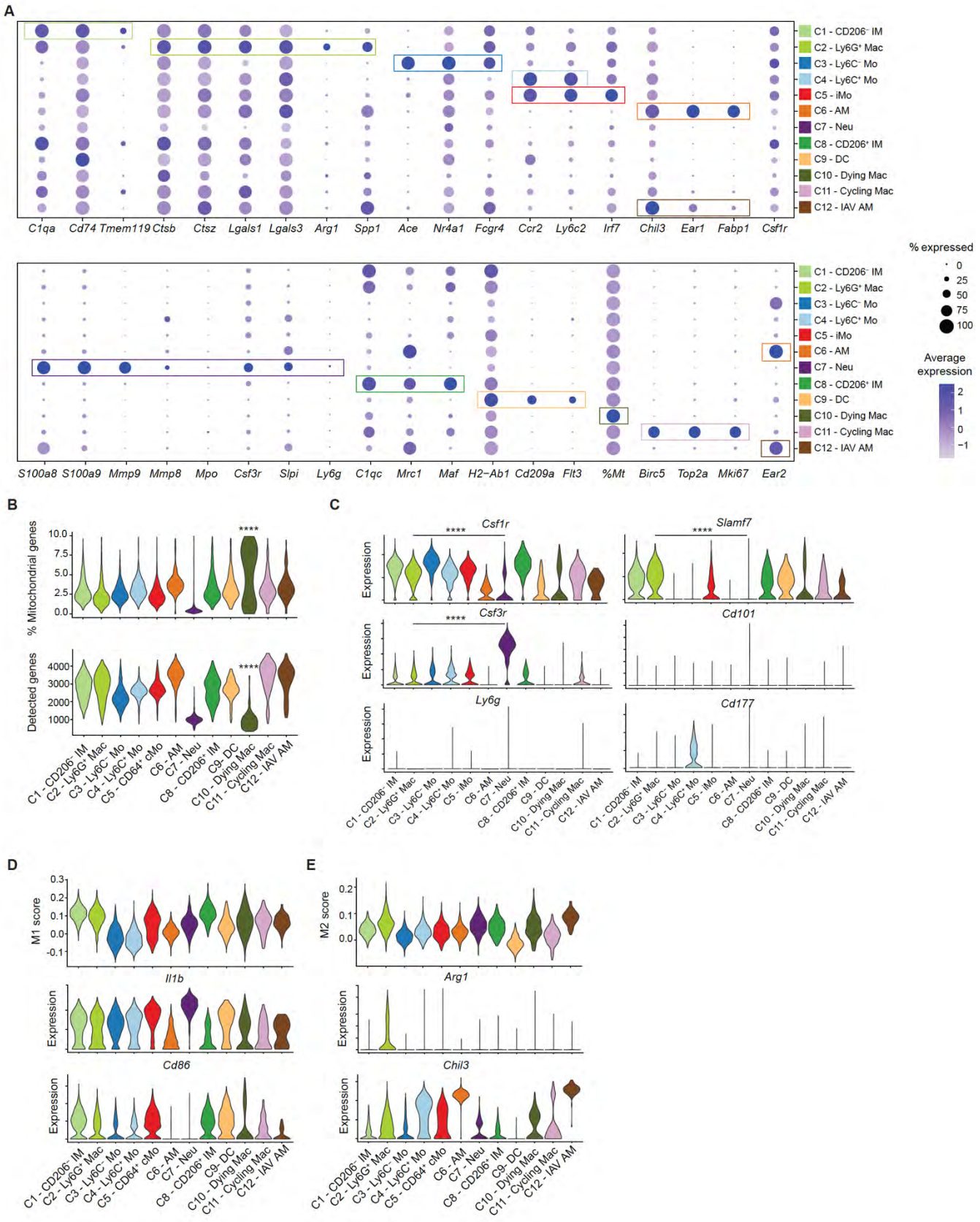
A
C1 - CD206⁻ IM
C2 - Ly6G⁺ Mac
C3 - Ly6C⁻ Mo
C4 - Ly6C⁺ Mo
C5 - iMo
C6 - AM
C7 - Neu
C8 - CD206⁺ IM
C9 - DC
C10 - Dying Mac
C11 - Cycling Mac
C12 - IAV AM
C1qa Cd74 Tmem119 Ctsb Ctsz Lgals1 Lgals3 Arg1 Spp1 Ace Nr4a1 Fcgr4 Ccr2 Ly6c2 Irf7 Chil3 Ear1 Fabp1 Csf1r
S100a8 S100a9 Mmp9 Mmp8 Mpo Csf3r Slpi Ly6g C1qc Mrc1 Maf H2−Ab1 Cd209a Flt3 %Mt Birc5 Top2a Mki67 Ear2
% expressed
0
25
50
75
100
Average expression
2
1
0
−1
B
% Mitochondrial genes
Detected genes
****
C
Csf1r
Slamf7
Csf3r
Cd101
Ly6g
Cd177
Expression
D
M1 score
Il1b
Cd86
E
M2 score
Arg1
Chil3

Fig. S2. Gene expression in and features of myeloid cell clusters identified by scRNA-seq at day 10 post-IAV. (**A**) Dot plots showing average expression of the indicated genes and % of cells expressing the genes within each cluster, related to Fig. 2A. (**B**) Percentage of mitochondrial genes (top) and number of detected genes (bottom) within each cluster, as depicted by violin plots (width: abundance of cells). (**C**) Expression of the indicated genes within each cluster, as depicted by violin plots (height: gene expression; width: abundance of cells). (**D**) M1 signature score (top) and expression of M1-related genes within each cluster, as depicted by violin plots (height: M1 score or gene expression; width: abundance of cells). (**E**) M2 signature score (top) and expression of M2-related genes within each cluster, as depicted by violin plots (height: M2 score or gene expression; width: abundance of cells). *P* values compare (B) C10 – dyings Macs *vs.* all other clusters or (C) C2 – $Ly6G^+$ Macs *vs.* C7 – Neutrophils and were calculated using a Wilcoxon rank sum test. ****, $P<0.0001$.

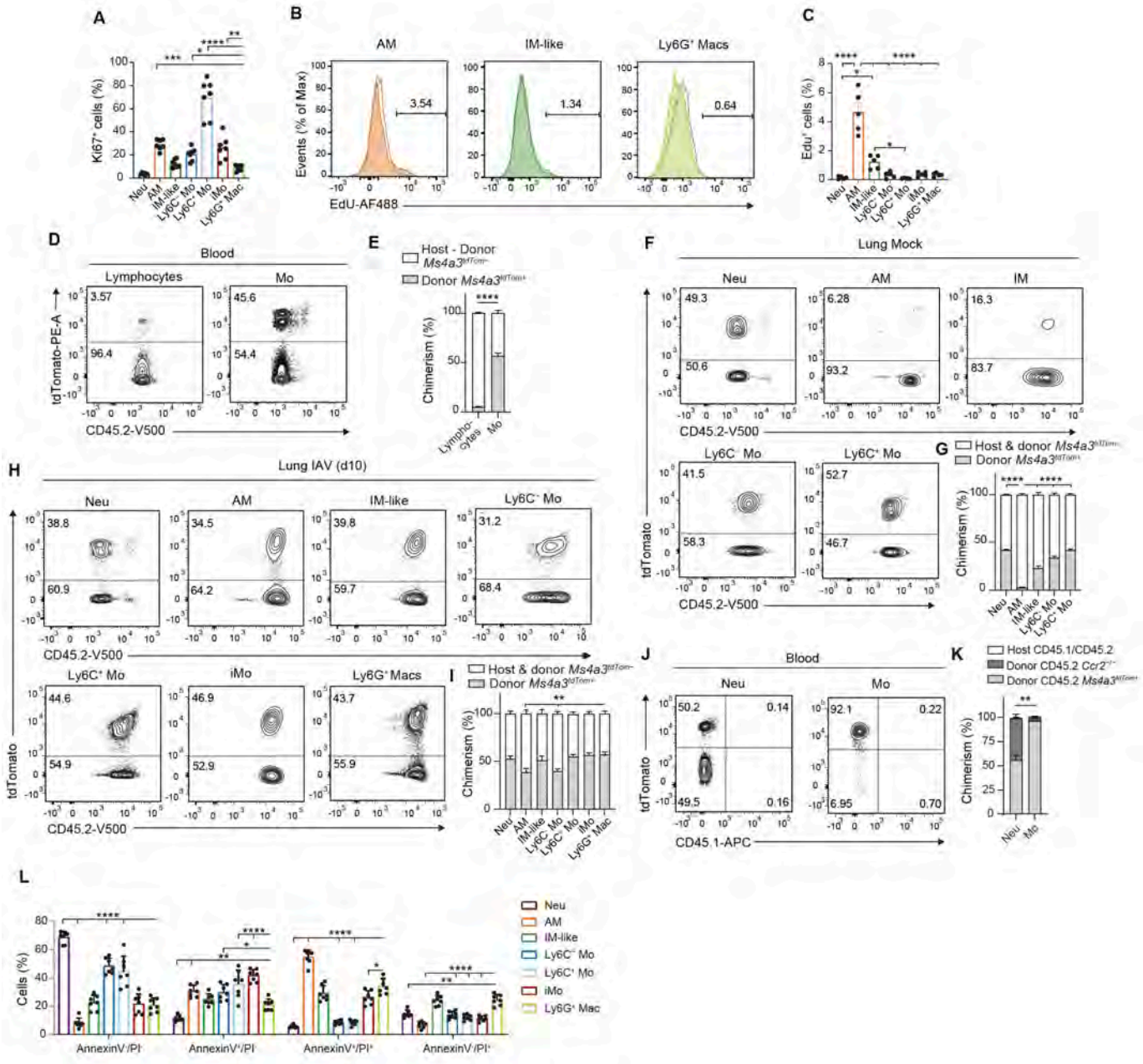
A
Ki67+ cells (%)
Neu
AM
IM-like
Ly6C- Mo
Ly6C+ Mo
iMo
Ly6G+ Mac
B
AM
IM-like
Ly6G+ Macs
Events (% of Max)
3.54
1.34
0.64
EdU-AF488
C
Edu+ cells (%)
D
Blood
Lymphocytes
Mo
tdTomato-PE-A
3.57
96.4
45.6
54.4
CD45.2-V500
E
Host - Donor Ms4a3tdTom-
Donor Ms4a3tdTom+
Chimerism (%)
Lympho-cytes
Mo
F
Lung Mock
Neu
AM
IM
49.3
50.6
6.28
93.2
16.3
83.7
CD45.2-V500
Ly6C- Mo
Ly6C+ Mo
41.5
58.3
52.7
46.7
tdTomato
G
Host & donor Ms4a3tdTom-
Donor Ms4a3tdTom+
Chimerism (%)
H
Lung IAV (d10)
Neu
AM
IM-like
Ly6C- Mo
38.8
60.9
34.5
64.2
39.8
59.7
31.2
68.4
CD45.2-V500
Ly6C+ Mo
iMo
Ly6G+ Macs
44.6
54.9
46.9
52.9
43.7
55.9
tdTomato
I
Host & donor Ms4a3tdTom-
Donor Ms4a3tdTom+
Chimerism (%)
J
Blood
Neu
Mo
50.2
0.14
49.5
0.16
92.1
0.22
6.95
0.70
tdTomato
CD45.1-APC
K
Host CD45.1/CD45.2
Donor CD45.2 Ccr2-/-
Donor CD45.2 Ms4a3tdTom+
Chimerism (%)
L
Cells (%)
AnnexinV-/PI-
AnnexinV+/PI-
AnnexinV+/PI+
AnnexinV-/PI+
Neu
AM
IM-like
Ly6C- Mo
Ly6C+ Mo
iMo
Ly6G+ Mac

Fig. S3. Ly6G$^+$ Macs do not proliferate, are short-lived and arise from recruited BM-derived monocytes post-IAV. (**A**) Bar graphs showing the % of Ki67$^+$ cells in the indicated lung myeloid cell populations, as quantified by flow cytometry in lungs of WT mice at day 10 post-IAV. (**B**) Representative histograms of EdU levels in AMs, IM-like cells and Ly6G$^+$ Macs from EdU-pulsed WT mice at day 10 post-IAV. Unpulsed mice were used as controls (grey line). (**C**) Bar graphs showing the % of EdU$^+$ cells in the indicated lung myeloid cell populations, as in (B). (**D**) Representative tdTomato and CD45.2 contour plots and (**E**) bar graph showing % of host and donor *Ms4a3*$^{tdTom-}$ chimerism and donor *Ms4a3*$^{tdTom+}$ chimerism of blood lymphocytes and monocytes (Mo) from lethally-irradiated thorax-protected WT mice reconstituted with *Ms4a3*$^{tdTom+}$ BM donor cells, evaluated by flow cytometry 4 weeks after reconstitution. (**F**) Representative tdTomato and CD45.2 contour plots and (**G**) bar graph showing % of host and donor *Ms4a3*$^{tdTom-}$ chimerism and donor *Ms4a3*$^{tdTom+}$ chimerism of the indicated lung myeloid cell populations, as in (D-E), evaluated by flow cytometry 4 weeks after reconstitution and 10 days after mock infection. (**H**) Representative tdTomato and CD45.2 contour plots and (**I**) bar graphs showing % of host + donor *Ms4a3*$^{tdTom-}$ chimerism and donor *Ms4a3*$^{tdTom+}$ chimerism of the indicated lung myeloid cell populations, as in (F-G), evaluated by flow cytometry 4 weeks after reconstitution and 10 days after IAV infection. (**J**) Representative tdTomato and CD45.1 contour plots and (**K**) bar graph showing % of host CD45.1/CD45.2, CD45.2 donor *Ccr2*$^{-/-}$ and *Ms4a3*$^{tdTom+}$ chimerism of blood neutrophils (Neu) and Mo from lethally-irradiated CD45.1/CD45.2 mice reconstituted with a 1:1 mix of CD45.2 *Ccr2*$^{-/-}$ and *Ms4a3*$^{tdTom+}$ BM cells, evaluated by flow cytometry 4 weeks after reconstitution. (**L**) Bar graph showing the frequency of Annexin V and PI negative and/or positive fractions within the indicated lung myeloid cell populations, quantified by flow cytometry at day 10 post-IAV in WT mice. (A,C,E,G,I,K,L) Data show mean + SEM and are pooled from 2 independent experiments (n=4-10 mice). *P* values compare donor *Ms4a3*$^{tdTom+}$ chimerism in (D,F,H,J) and were calculated using (A,C) a one-way ANOVA with Dunnett's post hoc tests, (E,K) a two-way ANOVA with Sidak's post hoc tests or (G,I,L) a two-way ANOVA with Tukey's post hoc tests. *, $P<0.05$; **, $P<0.01$; ****, $P<0.0001$.

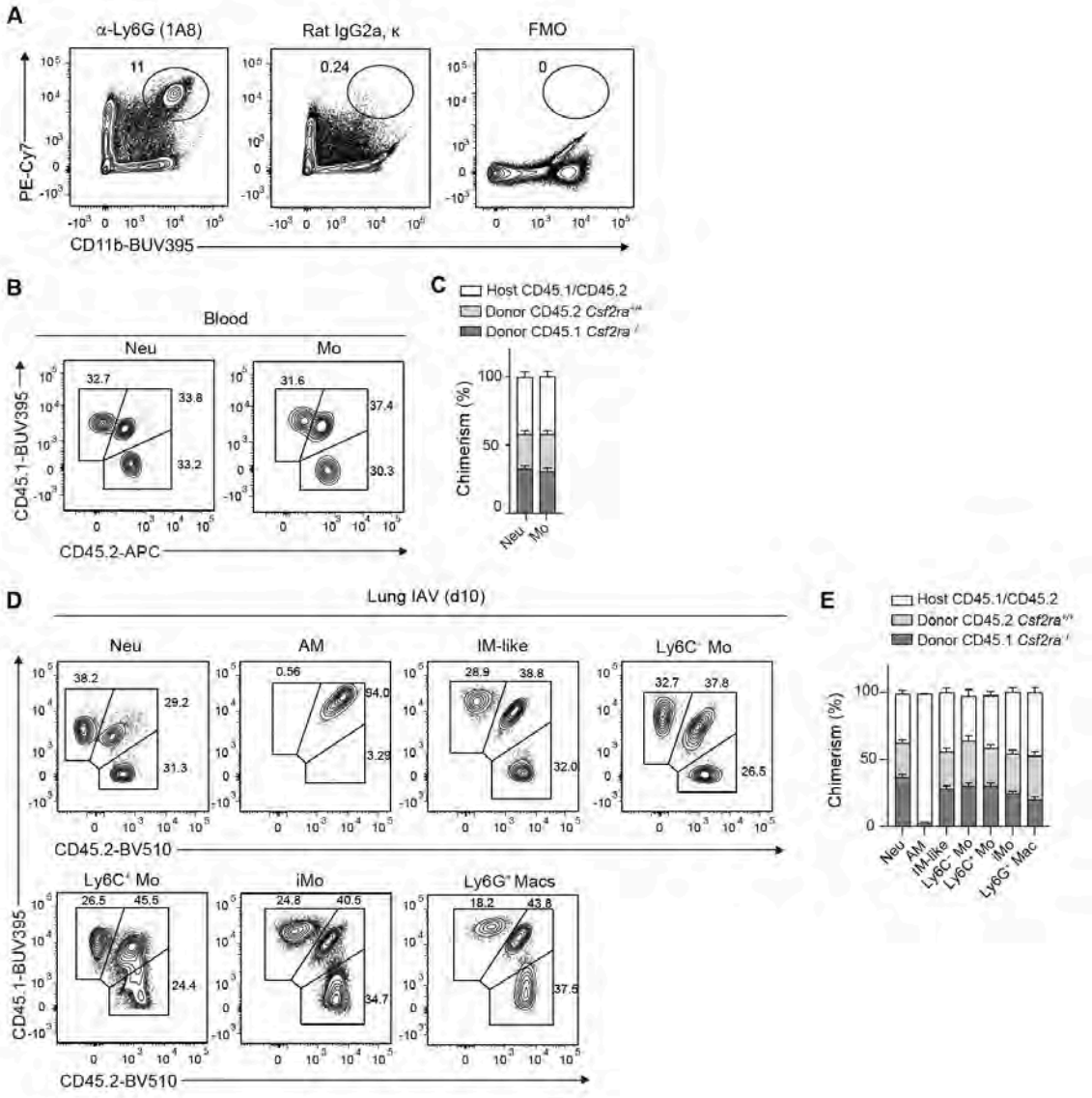

Fig. S4. Specificity of the anti-Ly6G staining and analysis of IAV-infected *Csf2ra*$^{-/-}$: *Csf2ra*$^{+/+}$ mixed BM chimeras. (**A**) Representative contour plots of PE-Cy7 and CD11b expression within lung live CD45^{+} cells in IAV-infected WT mice at day 10 post-IAV. Plots are representative of 1 of 6 mice analyzed, each giving similar results. (**B**) Representative CD45.1 and CD45.2 contour plots and (**C**) bar graph showing % of host CD45.1/CD45.2, CD45.2 donor *Csf2ra*$^{-/-}$ and CD45.1 *Csf2ra*$^{+/+}$ chimerism of blood neutrophils (Neu) and monocytes (Mo) from thorax-protected, lethally-irradiated CD45.1/CD45.2 mice reconstituted with a 1:1 mix of CD45.2 *Csf2ra*$^{-/-}$ and CD45.1 *Csf2ra*$^{+/+}$ BM cells, evaluated by flow cytometry 4 weeks after reconstitution. (**D**) Representative CD45.1 and CD45.2 contour plots and (**E**) bar graph showing % of host CD45.1/CD45.2, donor CD45.1 *Csf2ra*$^{-/-}$ and donor CD45.2 *Csf2ra*$^{+/+}$ chimerism of the indicated lung myeloid cell populations, as in (B-C), infected with IAV 4 weeks later and evaluated at day 10 post-IAV. (C,E) Data show mean + SEM and are pooled from 2 independent experiments (n=10 mice).

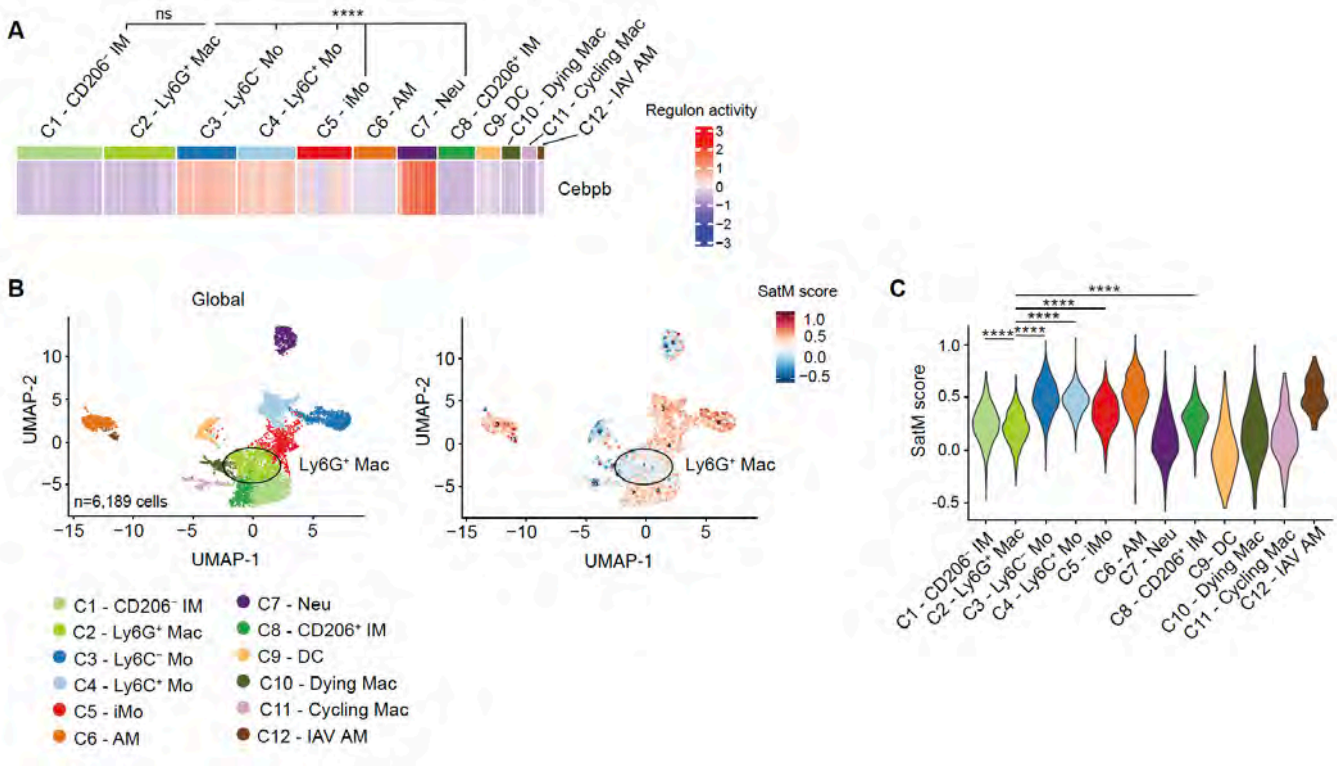

Fig. S5. Transcriptomic comparison of Ly6G$^+$ Macs and SatM monocytes. (**A**) Heatmap depicting predicted activities of Cebpb across lung myeloid cells post-IAV, evaluated by SCENIC analysis of the scRNA-seq data shown in Fig. 2A. (**B**) UMAP plots of scRNA-seq data depicting (left) the transcriptional identity of sorted lung live CD45$^+$F4/80$^+$ and/or CD11b$^+$ cells from mock- or IAV-infected WT mice 10 days post-infection (5 mice per time points), merged with a published dataset of steady-state lung monocytes and IMs (*69*), and (right) a SatM monocyte signature score (*35*). (C) SatM monocyte signature score within each scRNA-seq cluster, as depicted by violin plots (height: score; width: abundance of cells). (A,C) *P* values were calculated using a Wilcoxon rank sum test. ****, $P<0.0001$. ns, not significant.

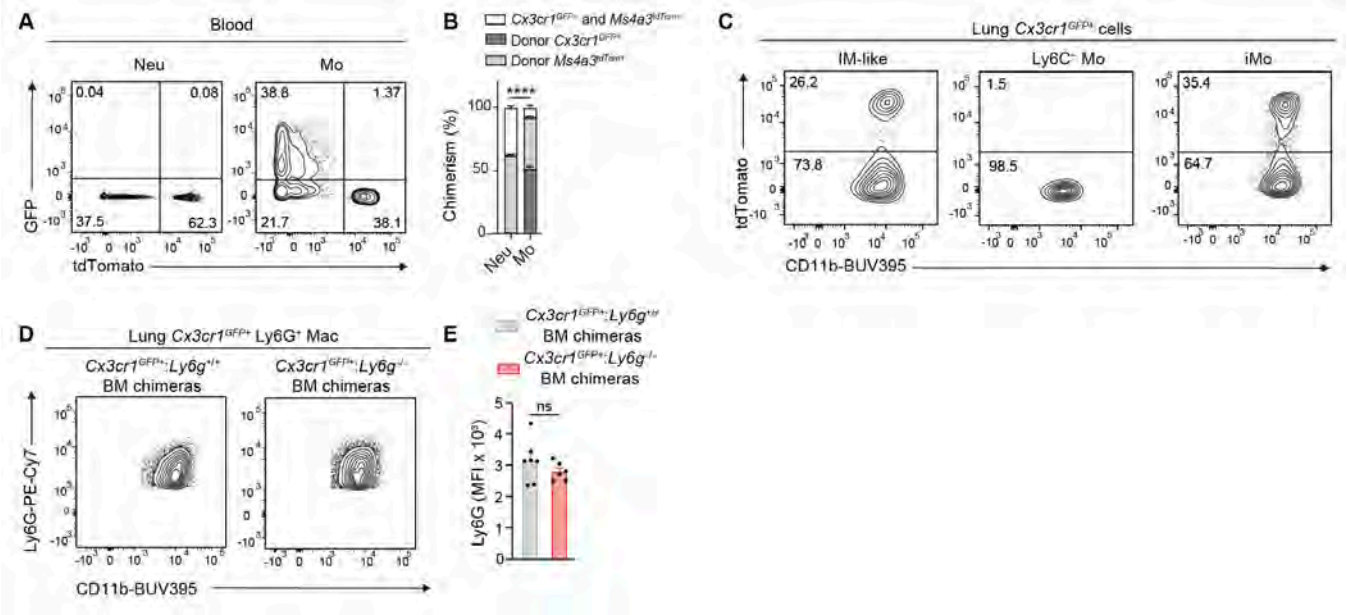

Fig. S6. Efferocytic abilities of lung myeloid cells post-IAV. (**A**) Representative GFP and tdTomato contour plots and (**B**) bar graph showing chimerism of *Cx3cr1*$^{GFP-}$*Ms4a3*$^{tdTom-}$, donor *Cx3cr1*$^{GFP+}$ and donor *Ms4a3*$^{tdTom+}$ cells in blood neutrophils (Neu) and monocytes (Mo) from lethally-irradiated CD45.2 WT mice reconstituted with a 1:1 mix of CD45.2 *Cx3cr1*$^{GFP+}$ and *Ms4a3*$^{tdTom+}$ BM cells, evaluated by flow cytometry 4 weeks after reconstitution. (**C**) Representative tdTomato and CD11b contour plots of the indicated lung *Cx3cr1*$^{GFP+}$ donor cell populations from lethally-irradiated CD45.2 WT mice reconstituted with a 1:1 mix of CD45.2 *Cx3cr1*$^{GFP+}$ and *Ms4a3*$^{tdTom+}$ BM cells, infected with IAV 4 weeks later and evaluated at day 10 post-IAV. (**D**) Representative Ly6G and CD11b contour plots of lung *Cx3cr1*$^{GFP+}$ Ly6G^{+} Macs from lethally-irradiated CD45.1/CD45.2 mice reconstituted with a 1:1 mix of CD45.2 *Cx3cr1*$^{GFP+}$ and *Ly6g*$^{+/+}$ (left) or *Ly6g*$^{-/-}$ (right) BM cells, infected with IAV 4 weeks later and evaluated at day 10 post-IAV. (**E**) Bar graph showing Ly6G expression levels in lung *Cx3cr1*$^{GFP+}$ Ly6G^{+} Macs, as in (D). (B,E) Data show mean + SEM and are pooled from 2 independent experiments (B: *n*=14 mice; E: *n*=6 mice). (B) *P* values compare donor *Cx3cr1*^{GFP} chimerism and were calculated using a two-way ANOVA with Sidak's post hoc tests. (E) *P* values were calculated using a two-tailed Student's *t* test. ns, not significant.

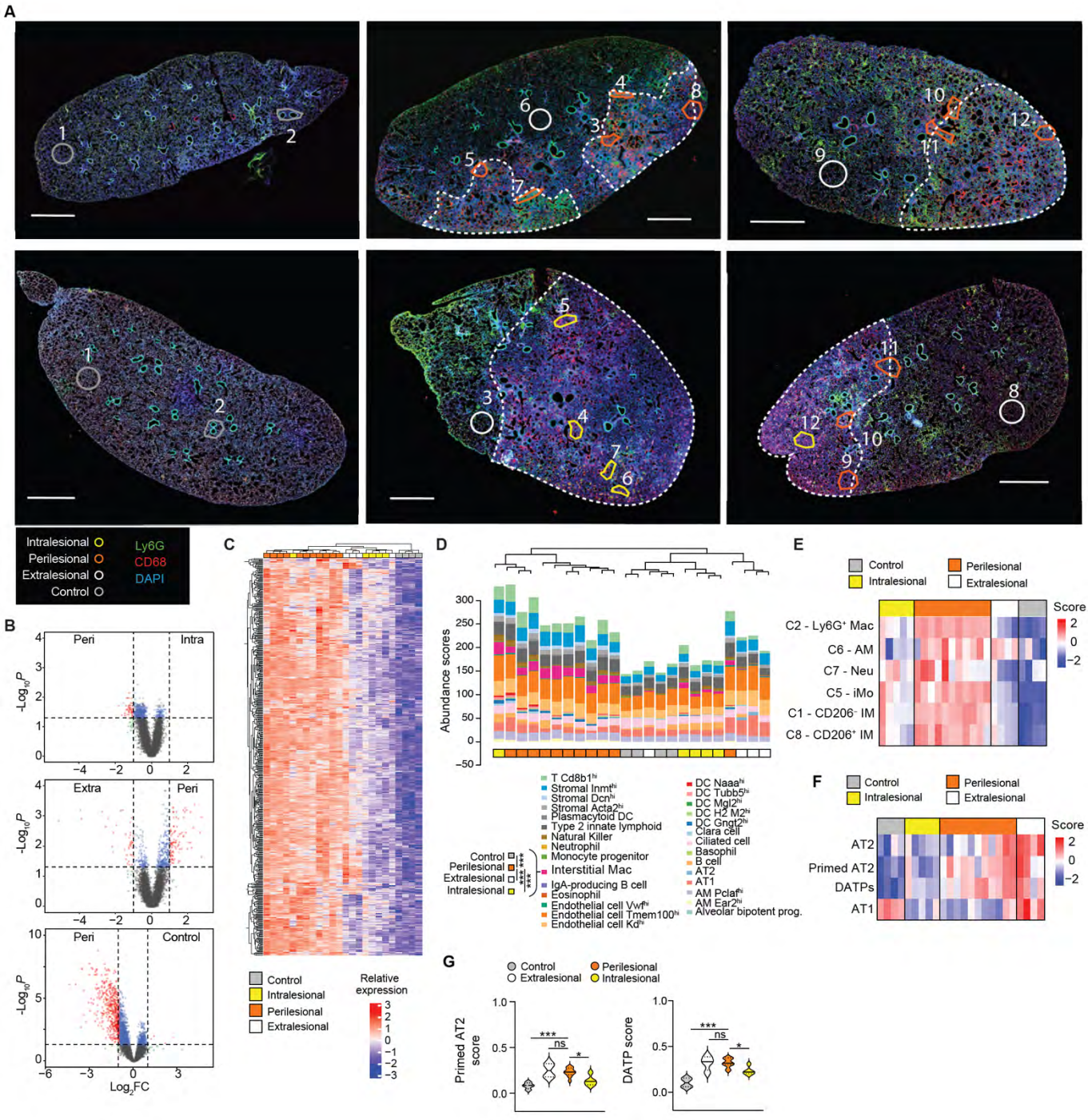
A
Intralesional
Perilesional
Extralesional
Control
Ly6G
CD68
DAPI
B
Peri
Intra
Extra
Peri
Peri
Control
-Log10P
Log2FC
C
Control
Intralesional
Perilesional
Extralesional
Relative expression
D
Abundance scores
T Cd8b1hi
Stromal Inmthi
Stromal Dcnhi
Stromal Acta2hi
Plasmacytoid DC
Type 2 innate lymphoid
Natural Killer
Neutrophil
Monocyte progenitor
Interstitial Mac
IgA-producing B cell
Eosinophil
Endothelial cell Vwfhi
Endothelial cell Tmem100hi
Endothelial cell Kdhi
DC Naaahi
DC Tubb5hi
DC Mgl2hi
DC H2 M2hi
DC Gngt2hi
Clara cell
Ciliated cell
Basophil
B cell
AT2
AT1
AM Pclafhi
AM Ear2hi
Alveolar bipotent prog.
E
Control
Intralesional
Perilesional
Extralesional
C2 - Ly6G+ Mac
C6 - AM
C7 - Neu
C5 - iMo
C1 - CD206- IM
C8 - CD206+ IM
Score
F
AT2
Primed AT2
DATPs
AT1
G
Primed AT2 score
DATP score
ns
*
***

Fig. S7. Identification of Ly6G$^+$ Macs-AT2 clusters by confocal microscopy in lung perilesional areas post-IAV. (**A**) Selection of regions of interest (ROIs) on lung sections from mock- or IAV-infected WT mice at day 10 post-IAV, stained with anti-Ly6G and anti-CD68 antibodies. (**B**) Volcano Plot depicting the differentially expressed genes (DEGs) between perilesional (Peri) and intralesional (Intra) areas (top), extralesional (Extra) and Peri areas (middle), and Peri and control areas (bottom). (**C**) Heatmap depicting the significantly upregulated genes in Peri areas as compared to Intra areas. (**D**) Cell deconvolution of the ROIs and abundance score of cell populations in individual ROIs using SpatialDecon algorithm. (**E**) Heatmap showing the signature score of the indicated myeloid cell populations within individual ROIs, inferred from the scRNA-seq data presented in Fig. 2A. (**F**) Heatmap showing the signature score of transitional epithelial cell states during AT2-mediated regeneration after bleomycin-induced lung injury, inferred from previously published scRNA-seq data ***(38)***. (**G**) Primed AT2 (left) and DATPs (right) signature scores within control, extralesional, perilesional and intralesional ROIs, as in (F), as depicted by violin plots (height: scores; width: abundance of cells). *P* values were calculated using (D) a two-way ANOVA with Tukey's post-hoc tests or (G) a one-way ANOVA with Tukey's post-hoc tests. *, $P<0.05$; ***, $P<0.001$. ns, not significant.

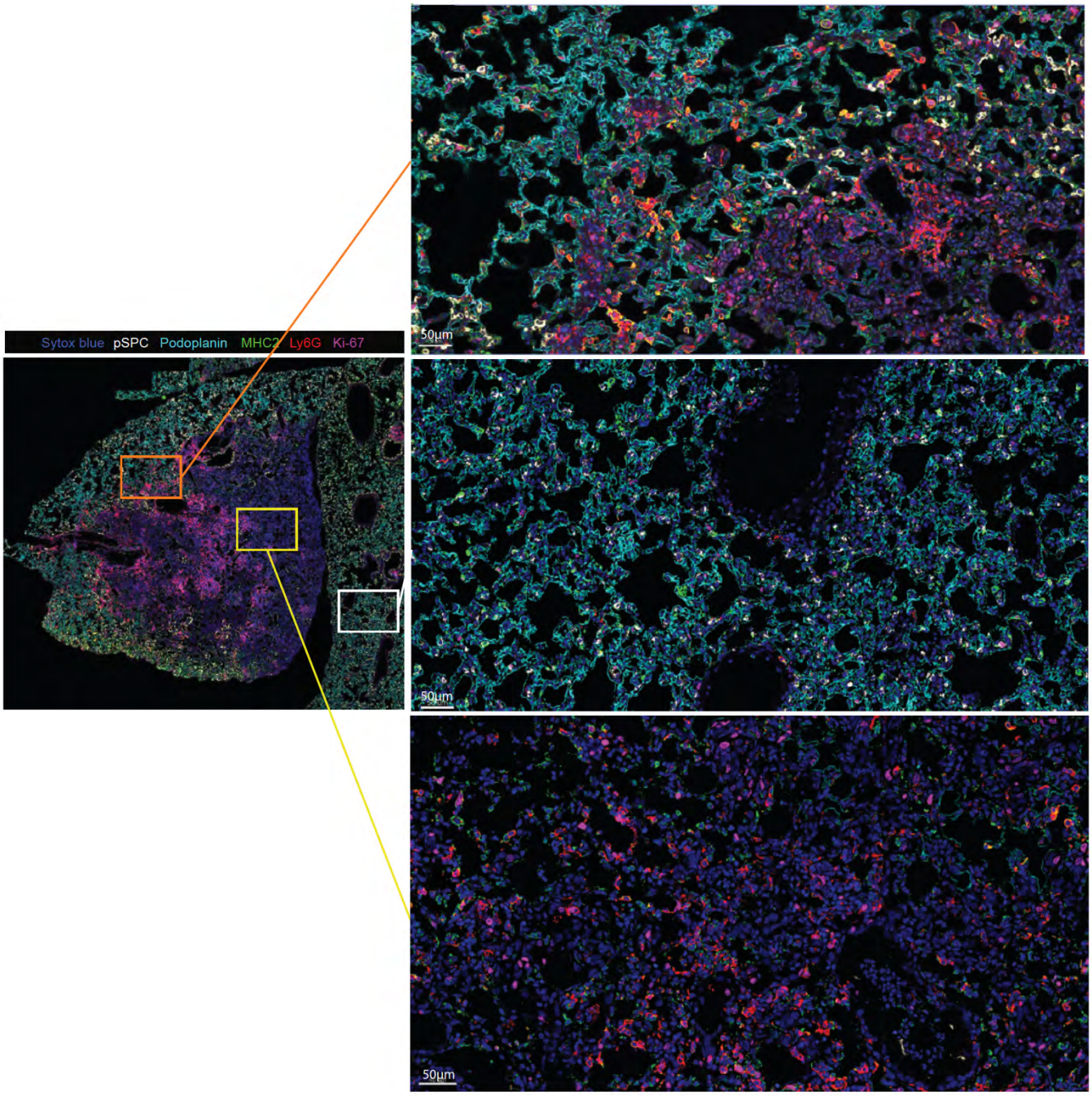
Sytox blue pSPC Podoplanin MHC2 Ly6G Ki-67
50µm
50µm
50µm

Fig. S8. Ly6G$^+$ Macs cluster with AT2 cells in perilesional areas. Representative high-resolution confocal laser scanning microscopy picture of a lung section from an IAV-infected WT mouse at day 10 post-IAV. Zooms of perilesional (orange) and intralesional (yellow) areas are shown. Pictures are representative of 1 of 6 mice analyzed, each of them giving similar results. Scale bar: 50 µm.

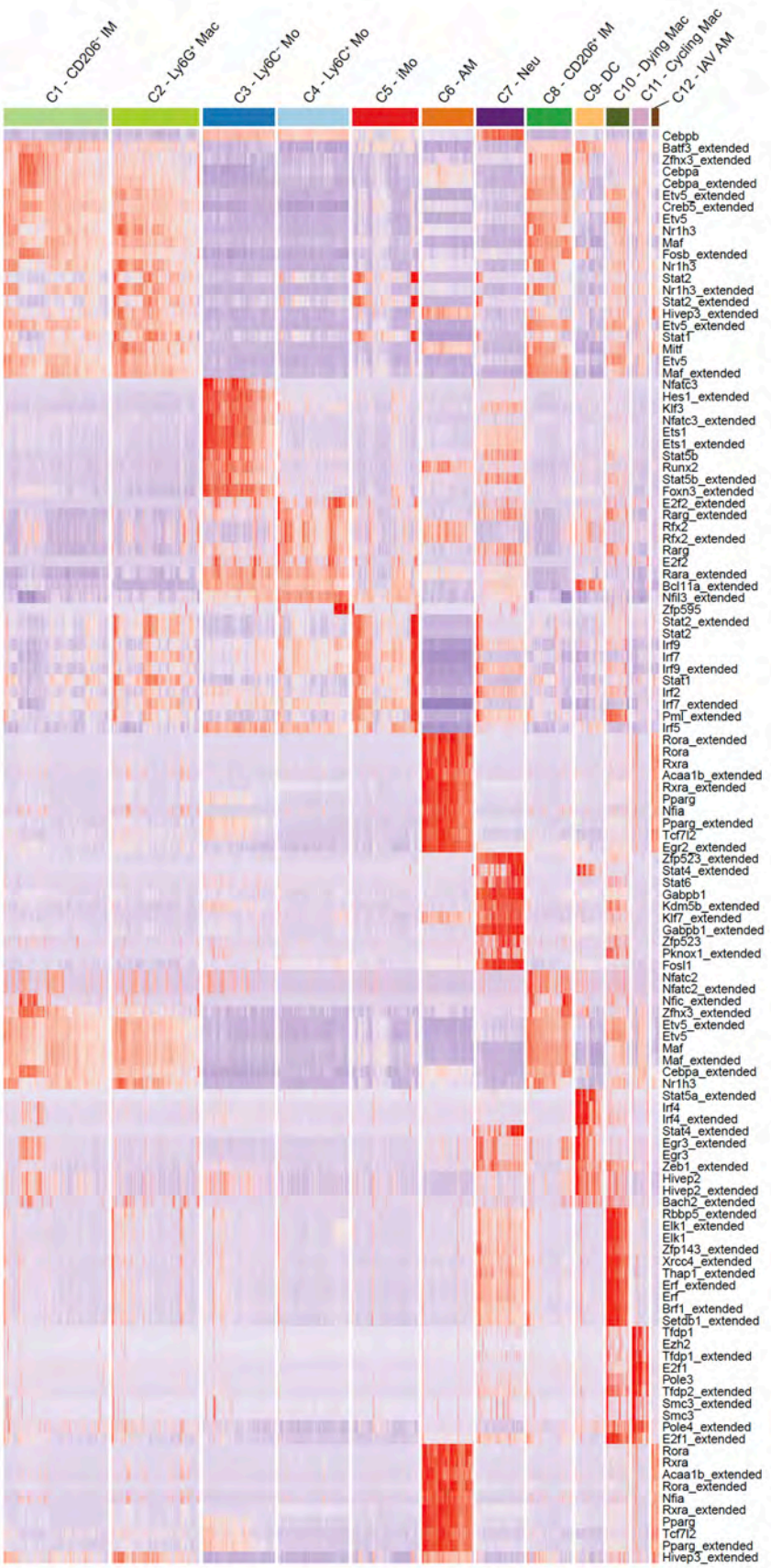
C1 - CD206+ IM
C2 - Ly6G+ Mac
C3 - Ly6C- Mo
C4 - Ly6C+ Mo
C5 - iMo
C6 - AM
C7 - Neu
C8 - CD206+ IM
C9- DC
C10 - Dying Mac
C11 - Cycling Mac
C12 - IAV AM
Cebpb
Batf3_extended
Zfhx3_extended
Cebpa
Cebpa_extended
Etv5_extended
Creb5_extended
Etv5
Nr1h3
Maf
Fosb_extended
Nr1h3
Stat2
Nr1h3_extended
Stat2_extended
Hivep3_extended
Etv5_extended
Stat1
Mitf
Etv5
Maf_extended
Nfatc3
Hes1_extended
Klf3
Nfatc3_extended
Ets1
Ets1_extended
Stat5b
Runx2
Stat5b_extended
Foxn3_extended
E2f2_extended
Rarg_extended
Rfx2
Rfx2_extended
Rarg
E2f2
Rara_extended
Bcl11a_extended
Nfil3_extended
Zfp595
Stat2_extended
Stat2
Irf9
Irf7
Irf9_extended
Stat1
Irf2
Irf7_extended
Pml_extended
Irf5
Rora_extended
Rora
Rxra
Acaa1b_extended
Rxra_extended
Pparg
Nfia
Pparg_extended
Tcf7l2
Egr2_extended
Zfp523_extended
Stat4_extended
Stat6
Gabpb1
Kdm5b_extended
Klf7_extended
Gabpb1_extended
Zfp523
Pknox1_extended
Fosl1
Nfatc2
Nfatc2_extended
Nfic_extended
Zfhx3_extended
Etv5_extended
Etv5
Maf
Maf_extended
Cebpa_extended
Nr1h3
Stat5a_extended
Irf4
Irf4_extended
Stat4_extended
Egr3_extended
Egr3
Zeb1_extended
Hivep2
Hivep2_extended
Bach2_extended
Rbbp5_extended
Elk1_extended
Elk1
Zfp143_extended
Xrcc4_extended
Thap1_extended
Erf_extended
Erf
Brf1_extended
Setdb1_extended
Tfdp1
Ezh2
Tfdp1_extended
E2f1
Pole3
Tfdp2_extended
Smc3_extended
Smc3
Pole4_extended
E2f1_extended
Rora
Rxra
Acaa1b_extended
Rora_extended
Nfia
Rxra_extended
Pparg
Tcf7l2
Pparg_extended
Hivep3_extended

Fig. S9. SCENIC analysis of lung myeloid cells at day 10 post-IAV. Heat map depicting predicted transcription factor (TF) activities across lung myeloid cells at day 10 post-IAV, as assessed by SCENIC analysis of the scRNA-seq data shown in Fig. 2A.

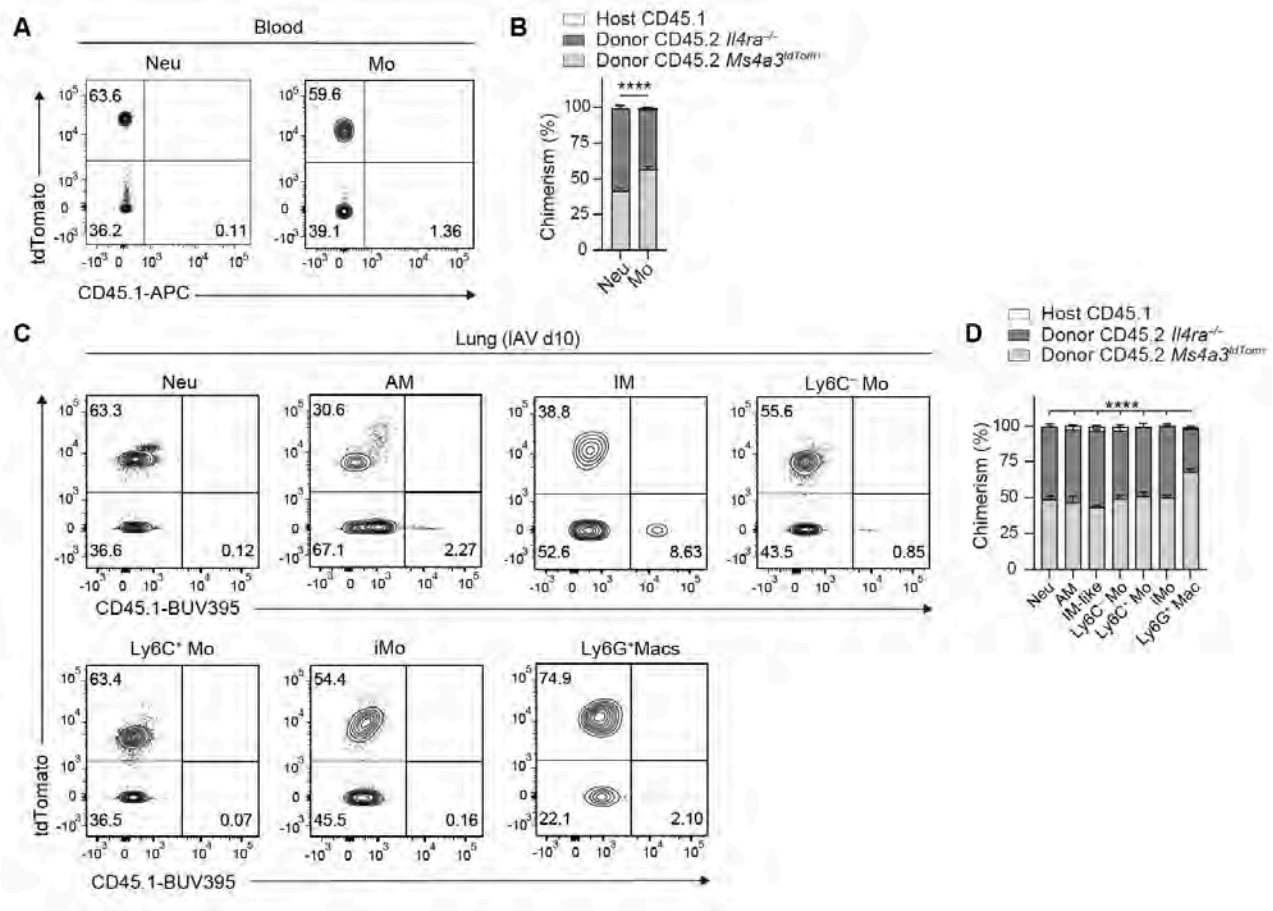

Fig. S10. Analysis of IAV-infected *Il4ra*$^{-/-}$:*Il4ra*$^{+/+}$ mixed BM chimeras. (**A**) Representative tdTomato and CD45.1 contour plots and (**B**) bar graph showing % of host CD45.1, donor CD45.2 *Il4ra*$^{-/-}$ and donor CD45.2 *Ms4a3*$^{tdTom+}$ chimerism of blood neutrophils (Neu) and monocytes (Mo) from lethally-irradiated CD45.1 mice reconstituted with a 1:1 mix of CD45.2 *Il4ra*$^{-/-}$ and *Ms4a3*$^{tdTom+}$ BM cells, evaluated 4 weeks after transplantation by flow cytometry. (**C**) Representative tdTomato and CD45.1 contour plots and (**D**) bar graph showing % of host CD45.1, donor CD45.2 *Il4ra*$^{-/-}$ and *Ms4a3*$^{tdTom+}$ chimerism of the indicated lung myeloid cell populations from lethally-irradiated CD45.1 mice reconstituted with a 1:1 mix of CD45.2 *Il4ra*$^{-/-}$ and *Ms4a3*$^{tdTom+}$ BM cells, infected with IAV 4 weeks later and evaluated at day 10 post-IAV. (B,D) Data show mean + SEM and are pooled from 2 independent experiments (B: n=4 mice; D: n=8 mice). (B,D) P values compare donor CD45.2 *Il4ra*$^{-/-}$ chimerism and were calculated using (B) a two-way ANOVA with Sidak's post hoc tests or (D) a two-way ANOVA with Tukey's post hoc tests. ***, P<0.001; ****, P<0.0001.

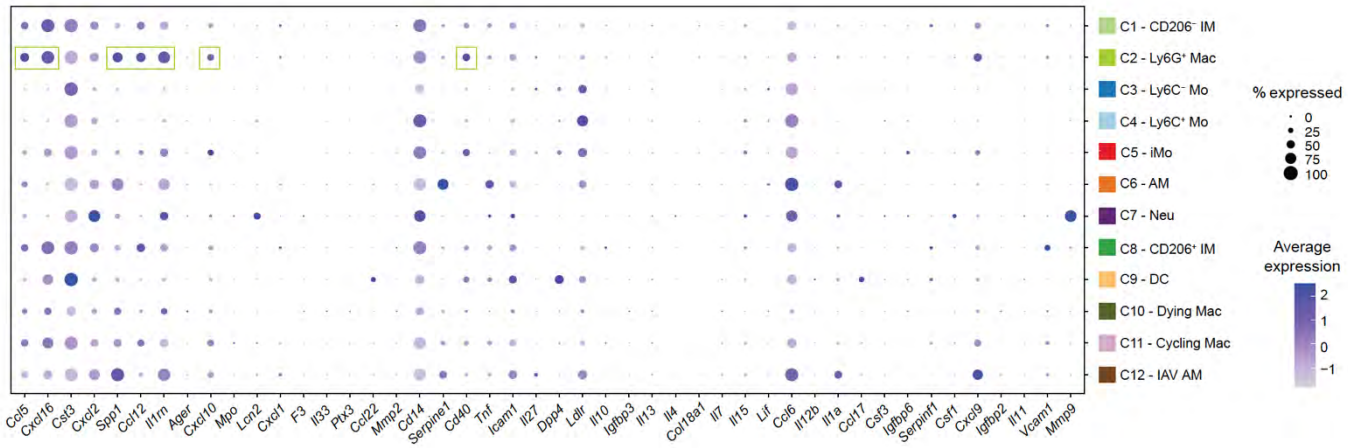

Fig. S11. Gene expression in myeloid cell clusters identified by scRNA-seq at day 10 post-IAV. Dot plots showing average expression of the indicated genes and % of cells expressing the genes within each cluster, related to Fig. 7K and 2A. Dot plots framed in green indicated gene that are significantly (P<0.0001) upregulated in C2 - Ly6G^{+} Macs as compared to other clusters. P values were calculated using a Wilcoxon rank sum test.

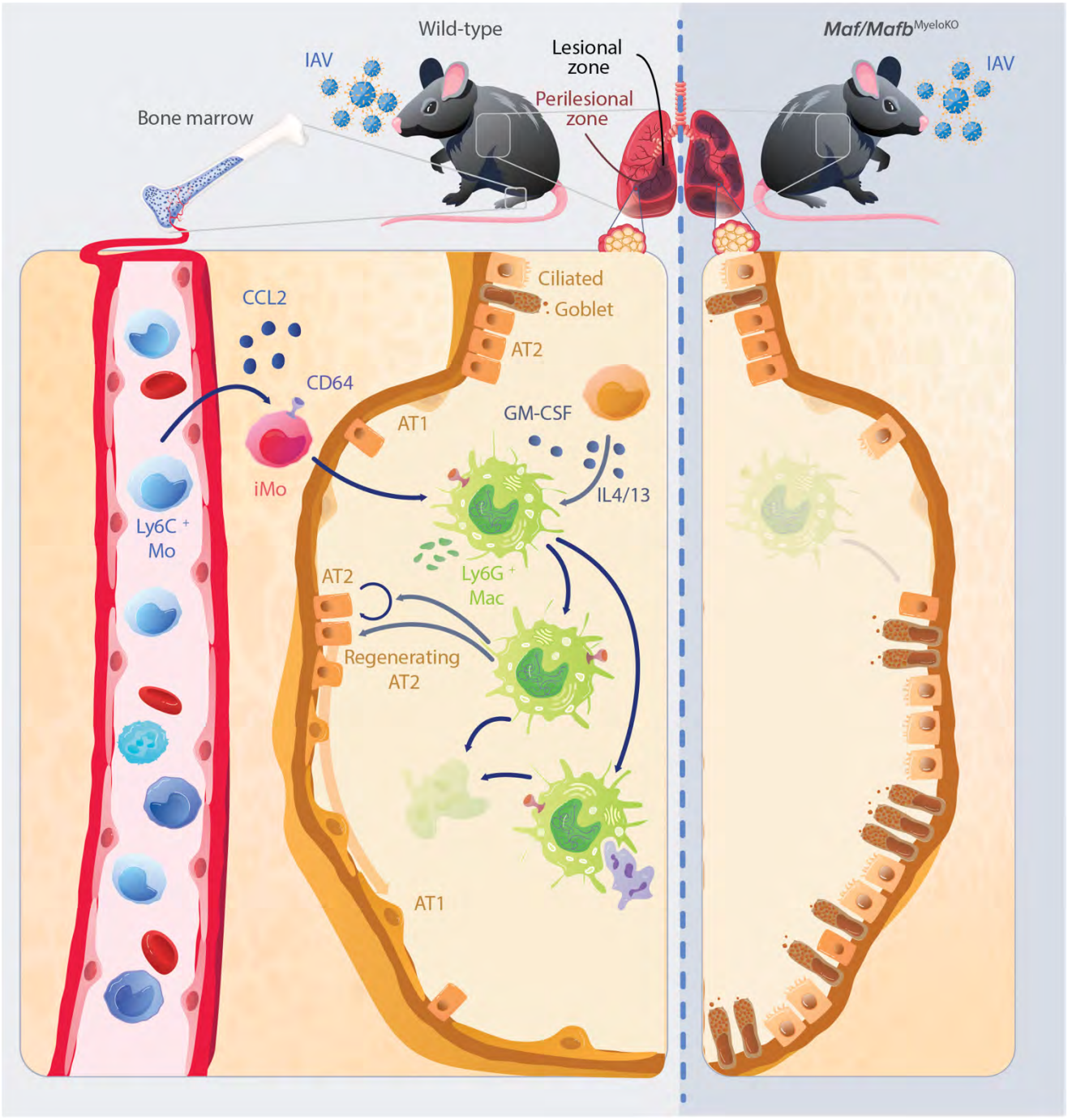
Wild-type
Maf/Mafb MyeloKO
IAV
IAV
Lesional zone
Perilesional zone
Bone marrow
CCL2
CD64
iMo
Ly6C + Mo
Ciliated
Goblet
AT2
AT1
GM-CSF
IL4/13
Ly6G + Mac
AT2
Regenerating AT2
AT1

Fig. S12. Proposed model of Ly6G$^+$ Mac-mediated alveolar epithelial regeneration after IAV-triggered injury. In mice, an atypical population of Ly6G$^+$ Macs is recruited from BM-derived Ccr2-dependent monocytes during the early recovery phase of IAV infection. Ly6G$^+$ Macs exhibit atypical ultrastructural features, are metabolically very active and short-lived, and are endowed with powerful phagocytic and efferocytic capabilities. They inhabit the alveolar spaces of lung perilesional areas, where they promote euplastic alveolar regeneration and AT2-to-AT1 differentiation via IL-4R-dependent mechanisms and soluble factors. In the absence of Ly6G$^+$ Macs, *Maf/MafB*^{MyeloKO} mice exhibit exacerbated morbidity, pathology and dysplastic bronchiolization of the alveoli.

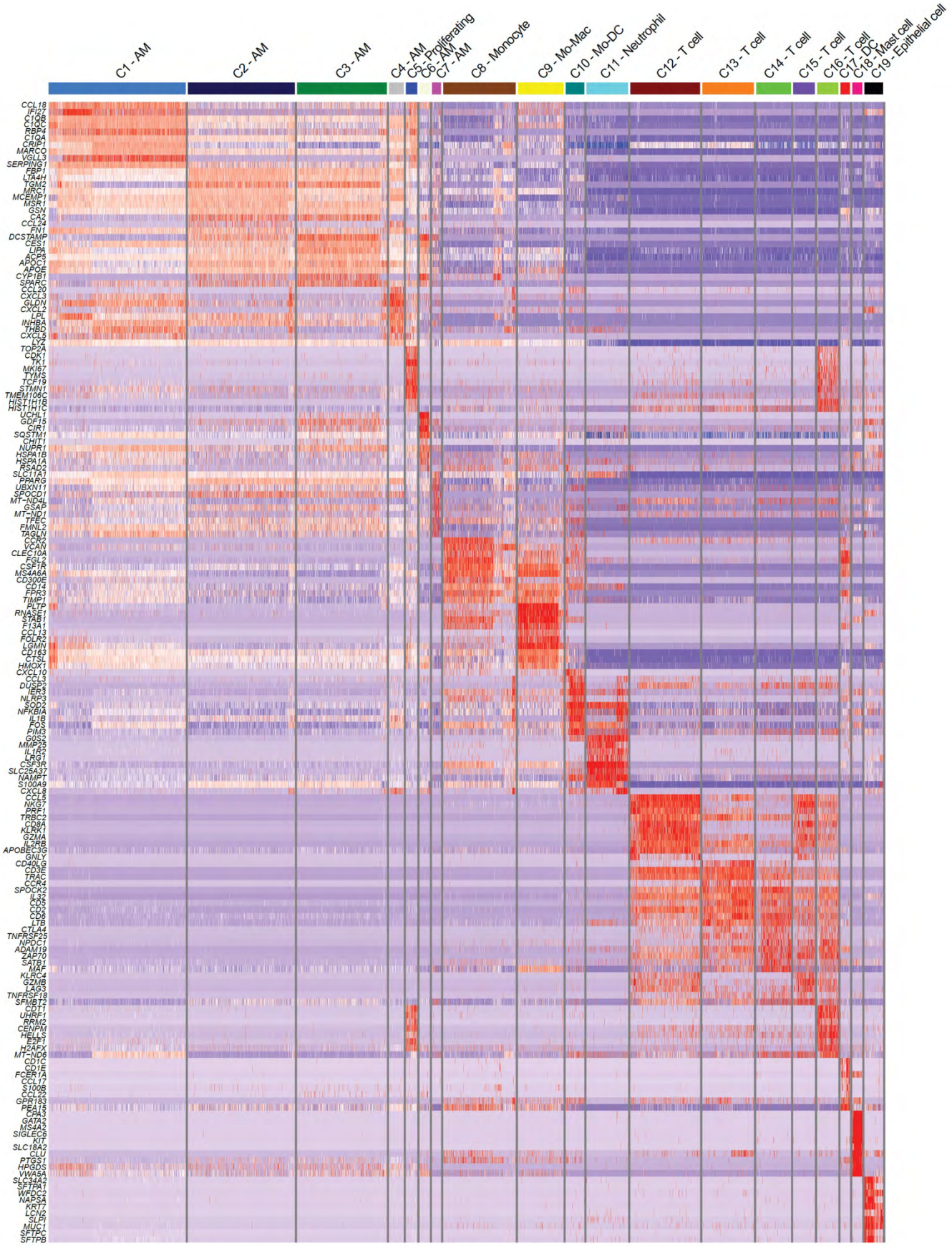
C1 - AM
C2 - AM
C3 - AM
C4 - AM
C5 - Proliferating
C6 - AM
C7 - AM
C8 - Monocyte
C9 - Mo-Mac
C10 - Mo-DC
C11 - Neutrophil
C12 - T cell
C13 - T cell
C14 - T cell
C15 - T cell
C16 - T cell
C17 - DC
C18 - Mast cell
C19 - Epithelial cell
CCL18
IFI27
C1QB
C1QC
RBP4
C1QA
CRIP1
MARCO
VSIG4
SERPINA1
FBP1
LTA4H
TGM2
MRC1
MCEMP1
MSR1
GSN
CA2
CCL24
FN1
DCSTAMP
CES1
LIPA
ACP5
APOC1
APOE
CYP1B1
SPARC
CCL20
CXCL3
GLDN
CXCL2
LPL
INHBA
THBS1
THBD
CXCL5
LYZ
TOP2A
CDK1
TK1
MKI67
TYMS
TCP19
STMN1
TMEM106C
HIST1H1B
HIST1H1C
UCHL1
GDF15
CIR1
SQSTM1
CHIT1
NUPR1
HSPA1B
HSPA1A
PSAP2
SLC17A1
PPARG
UBXN11
SPOCD1
MT-ND4L
GSAP
MT-ND1
TFEC
FMNL3
TAGLN
CCR2
VCAN
CLEC10A
FGL2
CSF1R
MS4A6A
CD300E
CD14
FPR3
TIMP1
PLTP
RNASE1
STAB1
F13A1
CCL13
FOLR2
LGMN
CD163
CTSL
HMOX1
CXCL10
CCL3
DUSP2
IER3
NLRP3
SOD2
NFKBIA
IL1B
FOS
PIM3
G0S2
MMP25
IL1R2
LRG1
CSF3R
SLC25A37
NAMPT
S100A9
CXCL8
CCL5
NKG7
PRF1
TRBC2
CD8A
KLRK1
GZMA
IL2RB
APOBEC3G
GNLY
CD40LG
CD3E
TRAC
CCR4
SPOCK2
IL32
CD5
CD2
CD6
LTB
CTLA4
TNFRSF25
NPDC1
ADAM19
ZAP70
SATB1
MAF
KLRC4
GZMB
IAH1
TNFRSF18
SFMBT2
CDT1
UHRF1
RRM2
CENPM
HELLS
E2F1
H2AFX
MT-ND6
CD1C
CD1E
FCER1A
CCL17
S100B
CCL22
GPR183
PEA15
CPA3
GATA2
MS4A2
SIGLEC6
KIT
SLC18A2
CLU
PTGS1
HPGDS
VWA5A
SLC34A2
SFTPA1
WFDC2
NAPSA
KRT7
LCN2
SLPI
MUC1
SFTPC
SFTPB

Fig. S13. Transcriptomic identities of human BALF single cells analyzed by scRNA-seq. Heatmap depicting the single cell expression of the 20 most upregulated genes within each cluster of human BALF cells analyzed by scRNA-seq, as shown in Fig. 8J.

Patient	Gender	Age	Disease status	Number of BALF cells analyzed
1	**M**	50	Bacterial pneumonia	858
2	**F**	63	Immunosuppressed, bacterial pneumonia	1,032
3	**M**	58	Interstitial pneumonia, metapneumovirus and cytomegalovirus infections	811
4	**M**	60	Pneumonia	1,445
5	**M**	71	Lung fibrosis and bacterial bronchopneumonia	311
6	**F**	62	Pneumonia	289
7	**M**	71	Immunosuppressed, bronchopneumonia	563

Table S1. Characteristics of patients from whom originate the BALF cells analyzed by scRNA-seq.

Reagents	Source	Cat. number
5-Ethynyl-2′-deoxyuridine	Santa Cruz Biotechnology	sc-284628
(Z)-4-Hydroxytamoxifen	Sigma-Aldrich	H7904
10X RBC Lysis Buffer (Multi-species)	Thermo Fisher Scientific	15270658
2-Mercaptoethanol	Thermo Fisher Scientific	21985023
Acetaminophen	Sigma-Aldrich	A7085
ALT ELISA Kit (Mouse)	Abcam	Ab2828-82
Agilent Seahorse XF Base Medium	Agilent	102353-100
Binding Buffer for Annexin V	Thermo Fisher Scientific	BMS500BB
Bleomycin sulfate - 10 mg	BIO-CONNECT	HY-17565
CD11b MicroBeads, human and mouse	Miltenyi Biotec	130-097-142
Cell-Tak™ Cell and Tissue Adhesive, 1 mg	Corning	354240
Click-iT™ Plus EdU Alexa Fluor™ 488 Flow Cytometry Assay Kit	Thermo Fisher Scientific	C10632
Collagenase IV	Thermo Fisher Scientific	17104019
Collagenase A	Roche	10103578001
Dispase® II protease	Sigma-Aldrich	D4693-1G
DMEM/F-12, no phenol red	Thermo Fisher Scientific	21041025
DNase I	Roche	11284932001
Donkey serum	Sigma-Aldrich	D9663
DPBS	Thermo Fisher Scientific	14190094
eBioscience™ Foxp3 / Transcription Factor Staining Buffer Set	Thermo Fisher Scientific	00-5523-00
Elastase from porcine pancreas	MedChemExpress	HY-P2974
Epoxy Embedding Medium kit	Sigma-Aldrich	45359
Fetal Bovine Serum	Thermo Fisher Scientific	A3160801
Formaldehyde, Extra Pure, Solution 37-41%, SLR, Fisher Chemical™	Thermo Fisher Scientific	F/1501/PB15
Hanks Balanced Salt Solution (HBSS)	Lonza	10-508F
Hemacolor	Sigma-Aldrich	111674
HEPES (1 M)	Thermo Fisher Scientific	15630080
Incucyte® Imagelock 96-well Plate	Sartorius	BA-04856
Insulin-Transferrin-Selenium (ITS -G) (100X)	Thermo Fisher Scientific	41400045
iTaq Universal SYBR Green Supermix	BioRad	1725120
L-Glutamine (200 mM)	Thermo Fisher Scientific	25030081
MEM Non-Essential Amino Acids Solution (100X)	Thermo Fisher Scientific	11140050
Méthanol	MerkMillipore	67-56-1
Milieu RPMI 1640	Thermo Fisher Scientific	21875091
Nimatek	Dechra	804132
Nunc® Lab-Tek® Chamber Slide™ system	Sigma-Aldrich	C7182
Penicillin-Streptomycin (10,000 U/mL)	Thermo Fisher Scientific	15140122
pHrodo™ Green E. coli BioParticles™ Conjugate for Phagocytosis	Thermo Fisher Scientific	P35366

Poly-D-lysine hydrobromide	Sigma-Aldrich	P6407
ProLong™ Diamond Antifade Mountant	Thermo Fisher Scientific	P36961
ProLong™ Gold Antifade Mountant with DNA Stain DAPI	Thermo Fisher Scientific	P36931
Propidium iodide	Thermo Fisher Scientific	P1304MP
Proteome Profiler Mouse XL Cytokine Array	R&D	ARY028
Recombinant Murine GM-CSF	Preprotech	315-03
Recombinant Murine IL-13	Preprotech	210-13
Recombinant Murine IL-4	Preprotech	214-14
Recombinant Murine M-CSF	Preprotech	315-02
RevertAid First Strand cDNA Synthesis Kit	Thermo Fisher Scientific	K1621
RNase A	Merck Millipore	70856
Rompun Sol Inj 2%	Bayer	76901
Sucrose	VWR	57-50-1
SYTOX™ Blue Nucleic Acid Stain	Thermo Fisher Scientific	S11348
Tissue-Tek® O.C.T. Compound	VWR	4583
Titriplex® III	Merck Millipore,	1084181000
TRITON® X-100 Detergent	MerkMillipore	648466
Trypsin-EDTA (0.05%), phenol red	Thermo Fisher Scientific	25300062
Tween 20	Acros Organics	AC233360010
UltraPure™ BSA (50 mg/mL)	Thermo Fisher Scientific	AM2616
Zytomed Systems HIER Citrate Buffer pH 6,0 (10 X)	Zytomed	ZUC028-500

Table S2. List of reagents used in this study.

Antibody	Source	Cat. number	RRID	Dilution (1.10^6 cells in 100 µL)
Annexin V APC Conjugate	Thermo Fisher	A35110		
Arginase 1 (A1exF5), APC	Thermo Fisher	17-3697-82	AB_2734835	1/100
Arginase 1 (A1exF5), PerCP-eFluor™ 710	Thermo Fisher	46-3697-82	AB_2734843	1/100
CD101 (Moushi101), PE	Thermo Fisher	12-1011-80	AB_1210729	1/100
CD115 (c-fms) (AFS98), APC	Thermo Fisher	17-1152-82	AB_1210789	1/100
CD11b (M1/70), BUV395	BD Bioscience	563553	AB_2738276	1/200
CD11b (M1/70), APC	Thermo Fisher	17-0112-83	AB_469344	1/100
CD11c (HL3), APC-Cy™7	BD Bioscience	561241	AB_10611727	1/200
CD124/IL4Ra (mILAR-M1), PE	BD Bioscience	561695	AB_10894018	1/100
CD170/Siglec F) (E50-2440), PE	BD Bioscience	552126	AB_394341	1/200
CD170/Siglec F (S17007L)FITC	Biolegend	155503	AB_2750232	1/200
CD177 Alexa Fluor™ 647	BD Bioscience	566599	AB_2869790	1/100
CD184/CXCR4 (2B11), APC	Thermo Fisher	17-9991-82	AB_10670878	1/60
CD31/PECAM-1 (390), APC	Thermo Fisher	17-0311-82	AB_657735	1/100
CD319 (4G2), APC	Biolegend	152003	AB_2632674	1/100
CD326/Epcam (G8.8), BV510	BD Bioscience	747748	AB_2738075	1/100
CD45.1(A20), APC	BD Bioscience	558701	AB_1645214	1/100
CD45.2 (104)V500	BD Bioscience	562129	AB_10897142	1/100
CD45.2 (104), BUV395	BD Bioscience	564616	AB_2738867	1/100
CD45.2 (104), FITC	BD Bioscience	561874	AB_10894189	1/100
CD64 (FcγRI) (X54-5/7.1), Brilliant Violet 421	Biolegend	139309	AB_2562694	1/100
c-MAF (sym0F1), PE	Thermo Fisher	12-9855-42	AB_2572747	1/100
CXCR4 (UMB2), Purified	AbCam	ab124824	AB_2564589	1/100
F4/80 (BM8), Brilliant Violet 650™	Biolegend	123149	AB_11220285	1/100
Ki-67 (SolA15), eFluor™ 570	Thermo Fisher	41-5698-82	AB_11040981	1/600
Ki-67 (SolA15), PerCP-eFluor™ 710	Thermo Fisher	46-5698-82	AB_11040981	0.3
Ly-6C (AL-21), PE-CF594	BD Bioscience	562728	AB_2737749	1/200
Ly-6G (1A8), PE-Cy™7	BD Bioscience	560601	AB_1727562	1/200
Ly-6G (1A8), Purified	BD Bioscience	551459	AB_394206	1/50
MafB (BRL046F), Purified	Bethyl Laboratories Inc.	A700-046		1/100

MHC Class II (I-A/I-E) (M5/114.15.2), Alexa Fluor™ 700	Thermo Fisher	56-5321-82	AB_494009	1/200
MHC II (IA/IE) (M5/114.15.2), PerCP/Cy5.5	Sony	1138130		1/600
Osteopontin (OPN), PE	R&D	IC808P	AB_10643832	1/100
Podoplanin (eBio8.1.1(8.1.1)), Super Bright™ 436	Thermo Fisher	62-5381-82	AB_2744800	1/200
Prosurfactant Protein C (EPR19839), Purified	AbCam	ab211326	AB_2927746	1/200
Secondary antibodies				
Goat anti-Rabbit IgG (H+L) Cross-Adsorbed Secondary Antibody, Alexa Fluor™ 532	Invitrogen	A11009	AB_2534076	1/1000
Goat anti-Rabbit IgG (H+L) Highly Cross-Adsorbed Secondary Antibody, Alexa Fluor™ 488	Invitrogen	A21209	AB_2535795	1/1000
GFP Polyclonal Antibody, Alexa Fluor™ 488	Invitrogen	A21311	AB_221477	1/200

Table S3. List of antibodies used in this study.